Dipartimento di Elettronica e Telecomunicazioni - Collegio di Ingegneria Informatica, del Cinema e Meccatronica

---

Master of science program in
MECHATRONIC ENGINEERING

Development of a SMA-actuated soft gripper with integrated pressure-based tactile sensing

Supervisors:
Prof. Luigi Mazza
Prof. Claudio Rossi (UPM - Spain)
Co-supervisors:
Giovanni Colucci
William Coral

Candidate:
Edoardo Selvaggi

Academic Year 2025-2026

Abstract

Current trends in Robotics, both in Service applications and in the Industrial sector through the continuous growth of Collaborative Robotics, show an increasing proximity between robots and humans, creating the need for safe, reliable and versatile robotic systems. This thesis addresses this need by developing a simple, multipurpose soft gripper that is motorless, gearless and lightweight. The gripper features silicone fingers actuated by nickel-titanium (nitinol) tendons, Shape Memory Alloy (SMA) wires that contract when heated above a known activation temperature. Each finger incorporates both agonist and antagonist SMA tendons for enhanced control. Additionally, an air channel embedded within the silicone matrix connects a compliant, hollow fingertip to a precision pressure sensor at the finger base, enabling contact detection between the finger and grasped objects. The fingers were characterized through three experimental procedures: a step response test to evaluate deformation dynamics in response to current steps, a free-load test analysing finger deformation under various current values, and an isometric test measuring fingertip force using a load cell at different current values and imposed deformations. The developed prototype was then mounted on a commercial robotic arm, replacing its original rigid gripper, to perform pick-and-place tasks with objects of varying shapes. Results showed the gripper can lift and manipulate objects ranging between 0.5 to 1.3 times its characteristic dimension, with a mass of up to 85 g in force-fit grasping and up to 150 g in case of form-fit grasping. Despite generating limited contact force, with a maximum measured finger-tip force of approximately 0.22 N, the gripper successfully manipulated tested objects by exploiting friction and partial finger wrapping. While SMA tendon actuation and pressure-based feedback systems are established in literature, this work's contribution lies in integrating these technologies, implementing agonist-antagonist SMA configurations for each finger, and developing a novel pressure-based sensing system with this specific implementation. The research focused primarily on the gripper's functional design and manufacturing, finger characterization, and pick-and-place testing; while control development remains limited to open-loop on/off commands with pressure signals acquired but not yet integrated into closed-loop feedback.

Contents

List of Figures

List of Tables

Chapter 1

Introduction

Robotic manipulation in unstructured environments remains one of the open challenges in modern robotics. The ability to grasp and handle objects of unknown shape, variable stiffness, and fragile surface, safely and without complex prior knowledge, requires a fundamental rethinking of gripper design. This thesis contributes to this effort by developing a soft gripper that integrates compliant SMA tendon-driven actuation with embedded pneumatic tactile sensing in a single prototype.

1.1 Soft Robotics and Soft Grippers

Current trends in robotics show an increasing proximity between robots and humans. In the industrial sector, collaborative robots, commonly referred to as cobots, are designed to operate alongside human workers in shared workspaces, replacing the traditional safety barriers of fully automated cells. In Service Robotics, robots are expected to operate in domestic and public environments, interacting with people and handling objects designed for human use. Both contexts demand robotic systems that are safe, reliable, and adaptable, properties that are difficult to achieve with classical rigid manipulators [1]. These requirements have driven the development of soft robotics, a paradigm in which systems are built from compliant, deformable materials that exploit mechanical compliance as a functional property rather than a limitation. Soft robotic systems can adapt passively to the geometry of the environment and the objects they interact with, reducing the need for complex sensing and control and making physical interaction with humans inherently safer [1]. Grasping and manipulation represent one of the most active application areas of soft robotics. Soft grippers, in contrast to their rigid counterparts, can conform to the shape of a target object through deformation, distributing contact forces over a larger area and reducing the risk of damage. This makes them particularly attractive for handling delicate, irregular, or variable objects, such as fresh produce, biological samples, or consumer goods, where rigid grippers would require precise geometric models or complex force control [1, 2]. Shintake et al. [1] provide a comprehensive taxonomy of soft robotic grippers, classifying them according to their gripping mechanism into three main categories: gripping by actuation, gripping by controlled stiffness, and gripping by controlled adhesion. Within the actuation category, representative technologies include fluidic elastomer actuators, tendon-driven structures with passive compliant elements, electroactive polymer actuators, and shape memory material actuators. Fluidic actuators, driven by pneumatic or hydraulic pressure, are the most widely adopted, owing to their large deformation capability and straightforward fabrication, but require external compressors or pumps that increase system volume and noise. Tendon-driven designs offer precise force transmission through flexible cables but depend on external motors. Electroactive polymers enable large deformations at low forces but require high driving voltages. Shape memory alloy actuators occupy a distinctive position in this landscape: they are compact, silent, require only an electrical current source, and exhibit a high force-to-weight ratio, making them well suited for lightweight and autonomous gripper designs, albeit with limited actuation bandwidth due to thermal cooling constraints. The present work adopts an SMA tendon-driven approach, combining the compactness and autonomy of SMA actuation with the shape adaptability of a silicone soft finger body.

The following sections introduce shape memory alloys and review the relevant literature on SMA-actuated soft grippers, then examine pressure-based tactile sensing systems, before identifying the research gap addressed by this thesis.

1.2 SMA-Actuated Soft Grippers

1.2.1 Shape Memory Alloys

Shape Memory Alloys (SMAs) are a class of metallic materials capable of recovering a pre-defined shape after deformation when subjected to an appropriate thermal stimulus. This behaviour arises from a reversible solid-state phase transformation between two crystallographic phases. Martensite is stable at low temperature and characterized by a monoclinic crystal structure, while austenite is stable at high temperature and characterized by an ordered cubic structure [3, 4]. A schematic of this transformation at the crystalline level, together with the characteristic strain-temperature hysteresis curve, is shown in Figure 1.1. When an SMA wire in the martensitic phase is mechanically deformed and subsequently heated above the austenite start temperature A_s, the material begins to transform back to austenite, recovering its memorized shape and generating a contraction force. The transformation is complete at the austenite finish temperature A_f. Upon cooling below the martensite start temperature M_s, the reverse transformation begins and is complete at the martensite finish temperature M_f. The hysteretic nature of the transformation, whereby the heating and cooling paths do not coincide, is a fundamental property of SMAs with important implications for their use as actuators: the output strain at a given temperature depends not only on the current temperature but also on the thermal history of the wire [4].

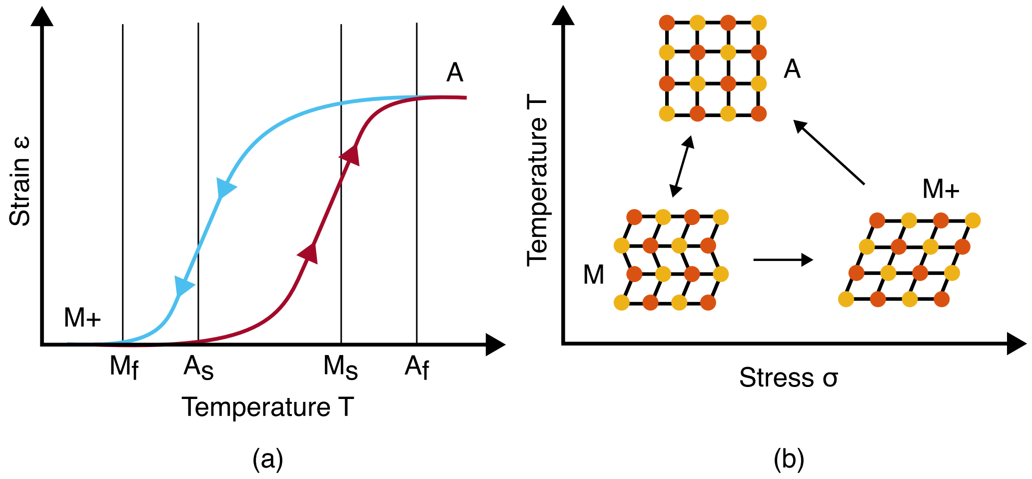

Figure 1.1: **(a)** Strain-Temperature plot showing a cycle between detwinned martensite phase M+ and austenite phase A, through heating and cooling under isobaric conditions (constant applied stress). **(b)** Temperature-Stress plot showing the three crystalline states of an SMA: twinned martensite M, detwinned martensite M+ and austenite A.

Among the various SMA compositions, nickel-titanium alloys (NiTi, commercially known as Nitinol) are the most widely used in robotics applications, due to their favorable combination of large recoverable strain, typically up to 4–5%, high force-to-weight ratio, bio-compatibility, and commercial availability. SMAs are commonly found in several formats. Wires contract along their axis upon heating and are the simplest and most widely used actuator form, strips can produce bending when heated, coils or springs generate larger displacements at lower forces, and knitted or woven textile composites enable complex distributed actuation behaviours [5]. It is worth noting that at low temperature the martensite phase can exist in two states: twinned martensite, in which the material has no net deformation, and detwinned martensite, in which the crystal variants are reoriented by an applied mechanical stress [6]. To exploit the shape memory effect in a cyclically actuated system, a bias force must be applied to the wire during cooling, typically provided by the elastic restoring force of the surrounding silicone matrix or by an antagonist element, so that the wire is stretched back into the detwinned martensitic state and can contract again upon the next heating cycle. Heating is most commonly achieved through direct Joule heating, passing an electrical current through the wire itself, although indirect heating via adjacent resistive elements is also possible. By means of appropriate heat treatment, SMAs can be programmed to recover a bent or curved shape rather than simply contracting, enabling a wider range of actuation geometries [3]. In the present work, NiTi wire in the contracting format is adopted, representing the simplest and most controllable configuration. An additional property of NiTi SMAs relevant to control is the variation of electrical resistance with phase state. As the material transforms from martensite to austenite, its resistivity changes in a characteristic and repeatable fashion. Song et al. [7] demonstrate that the electrical resistance of a NiTi wire depends on the martensite phase fraction, temperature, and mechanical stress, and that this relationship can be modelled and used as a feedback signal for closed-loop position control without the need for external displacement sensors, a property known as self-sensing. The main limitations of SMA actuators are their relatively slow actuation bandwidth, dictated by the thermal cooling time of the wire, and the nonlinear, hysteretic relationship between input current and output strain, which complicates open-loop control. For a 0.2 mm diameter Flexinol LT wire, the type adopted in this work, the manufacturer specifies a recommended actuation current of 660 mA and a cooling time of approximately 3.2 seconds in still air [31]. These characteristics make SMAs well suited to applications where compactness, silence, and autonomy are valued over actuation speed, such as soft gripper design.

1.2.2 SMA-Actuated Soft Grippers in the Literature

Several works in the literature have explored the use of SMA wires and strips as actuators for soft robotic fingers and grippers. A common approach consists in embedding SMA wires directly within a polymeric matrix, where contraction upon heating produces a bending deformation of the finger body. Lee et al. [8] proposed the use of free-sliding SMA wires as long tendons routed through the polymeric matrix via sheaths, decoupling the tendon length from the matrix length. This design allows significantly larger bending angles and tip forces to be achieved, up to 400 deg and 0.89 N respectively, while maintaining a compact form factor through the use of bearing-based tendon routing modules. Building on this direction, Rodrigue et al. [9] demonstrated that introducing an initial curvature in the actuator cross-section, realized through a double casting process, can further increase the maximum bending angle and grasping force without modifying the actuator dimensions. Kim et al. [10] developed a tendon-driven artificial finger based on a smart soft composite (SSC) structure, where SMA wires slide through a matrix reinforced with glass fiber layers, achieving a biomimetic bending motion and demonstrating multi-object grasping with a five-finger hand. Tuyboyov et al. [11] extended this concept by interweaving SMA wires with glass fiber textiles in a PDMS matrix, enabling multi-mode and bidirectional bending behaviours through variation of the wire interweaving pattern. Wang and Ahn [12] addressed the limited grasping force of SMA-based soft grippers by integrating shape memory polymer (SMP) structures within the finger hinges, achieving variable stiffness and increasing the maximum grasping force by approximately ten times compared to the low-stiffness configuration. Abdullah et al. [13] explored a different approach, using thicker SMA wires of 1 mm diameter pre-trained through heat treatment to bend upon activation rather than contract as tendons. Different wire configurations embedded in silicone fingers were compared in terms of tip force and bending angle, demonstrating the influence of wire geometry and training on actuator performance. She et al. [14] presented a fully integrated five-finger soft robotic hand embedding SMA strips as agonist actuators and an antagonist SMA strip for shape recovery, together with a flexure sensor for closed-loop control, all within a single silicone body, demonstrating the feasibility of integrating actuation, sensing, and recovery within a single soft finger. Hellebrekers et al. [15] demonstrated a complementary approach, integrating a stretchable microelectronic sensor skin onto an SMA-actuated soft gripper, embedding pressure, proximity, temperature, and orientation sensors connected by liquid metal traces for multi-modal sensing. Beyond grippers, SMAs embedded in soft polymeric matrices have been explored as muscle-like actuators in bio-inspired robotic systems. Coral et al. [4] provide a comprehensive review of SMA-based actuation in bio-inspired robots, covering systems operating in water, air, and ground environments. Among the prototypes discussed, the iTuna robot fish [16] is particularly relevant: SMA wires in an antagonistic configuration act on a continuous polycarbonate backbone, producing controlled bending of each body segment. The same research group also developed soft dorsal and anal fins for 3D maneuvering, where pairs of SMA wires are embedded in thin silicone fin structures and produce bending through contraction upon Joule heating [17]. The Kheirikhah et al. review [3] further documents the breadth of SMA applications in robotics, confirming SMAs as a versatile and established actuation technology for soft and compliant systems. The finger design proposed in the present work draws directly from two of these contributions: the tendon sheath and U-shaped routing concept of Lee et al. [8], which allows the SMA wire to slide freely within the silicone matrix and transmit its contraction as a bending force at the fingertip, and the antagonistic SMA wire architecture embedded in a silicone structure demonstrated by Coral and Rossi [17], which enables bidirectional actuation and active recovery of the neutral position.

1.3 Pressure-Based Tactile Sensing in Soft Grippers

Tactile sensing in robotic manipulation has received increasing attention as a means to enable contact detection, force estimation, and slip detection without relying solely on external vision systems. Among the approaches proposed in the literature, pneumatic tactile sensing, based on the deformation of a compliant air-filled cavity connected to a pressure sensor, has emerged as a particularly attractive solution for soft robotic applications due to its mechanical simplicity, inherent compliance, and ease of fabrication. Gong et al. [18] demonstrated a pneumatic tactile sensor based on a latex air-filled bladder applied to a robotic fingertip, capable of detecting contact force, vibration, object softness, and surface roughness through pressure changes. The sensor exhibited good linearity, low hysteresis, and wide sensing range, and the authors highlighted the possibility of customizing its mechanical properties by varying the bladder wall thickness. Shang et al. [22] integrated internal air-filled channels directly into 3D-printed fin-ray compliant fingers, the FORTE system, achieving force estimation in the 0–8 N range with ±0.2 N accuracy and slip detection within 100 ms at a sampling rate of 2 kHz. The authors noted that temperature variations in the sealed channel introduce pressure noise, a limitation also observed in the present work and attributed to the ideal gas law. A related approach uses actively pressurized rather than passively air-filled cavities. Pozzi et al. [20] embedded independently inflatable soft pneumatic pads within the rigid phalanges of a tendon-driven gripper, using the pads simultaneously as contact force sensors and as actuators for in-hand manipulation and grasp adjustment. Colucci [21] proposed a hydro-pneumatic soft pad system, termed PneuTact, in which compliant fluid-filled membranes are mounted on the distal links of a rigid gripper and connected to auxiliary pneumatic volumes, allowing active stiffness modulation of the contact interface in addition to force sensing. Kuppuswamy et al. [23] proposed a different approach with the Soft-bubble gripper, where highly compliant inflated membranes are combined with an internal depth camera for visuo-tactile sensing, enabling in-hand pose estimation and tactile classification. The present work adopts a passive air-filled approach: compliant bladders are embedded within the silicone finger body and connected to miniaturized pressure sensors at the finger base. Unlike the inflatable systems of Pozzi et al. and Colucci, the bladders are not pressurized and require no external air supply, contact is detected purely through the pressure rise generated by bladder compression. This configuration shares the core sensing principle with Gong et al. while being fully integrated within a soft actuated finger rather than applied as an add-on to a rigid structure.

1.4 Research Gap and Thesis Contribution

A review of the literature reveals that, while SMA tendon-driven actuation and pneumatic tactile sensing have each been explored in soft robotic systems, their integration within a single soft finger prototype has not been reported. This thesis addresses this gap by developing a soft gripper that combines both subsystems in a unified design. SMA wires are used as tendons routed through the silicone finger body, exploiting their high force-to-weight ratio, silent operation, and absence of external pressure supply. The agonist-antagonist tendon architecture enables bidirectional actuation, allowing active control of both finger closing and neutral position recovery, a capability not achievable with single-tendon designs. Pneumatic tactile sensing is implemented through compliant air-filled bladders embedded in the fingertip and connected to miniaturized pressure sensors at the finger base, providing contact detection and basic slip identification. The two subsystems integrate naturally within the same silicone body: the cross-sectional area occupied by the SMA tendons within the matrix is minimal, leaving sufficient material for the bladder walls, while the compliance of the bladder and sensing channel does not interfere with the bending deformation of the finger. The result is a compact soft actuator that integrates actuation and tactile sensing within a single silicone matrix, supported by the rigid finger base and tensioning system described in the following chapters, without the need for external compressors or additional sensing hardware.

The remainder of this thesis is organized as follows. Chapter 2 presents the functional design of the gripper, describing the mechanical architecture, the finger geometry, the actuation principle, and the electronics system. Chapter 3 covers the prototyping process, detailing the mold design, the silicone casting procedure, the SMA tendon assembly, and the firmware implementation. Chapter 4 presents the experimental characterization of the finger and the gripper, including dynamic step response tests, free-load deformation tests, isometric force tests, pick and place validation on a robotic arm, and evaluation of the tactile sensing system. Chapter 5 summarizes the main findings, identifies the limitations of the current prototype, and proposes directions for future development.

Chapter 2

Functional design

The proposed soft gripper system was designed following a modular approach. This chapter describes its architecture from the top level down. The overall gripper assembly and structural frame are presented first, followed by the electronics subsystem and the soft finger subsystem. Each is described in detail, supported by functional schematics and executive drawings including all relevant dimensional specifications.

2.1 Gripper

Figure 2.1 depicts the 3D model of the developed gripper assembly. The device frame has a cylindrical shape, resulting from the assembly of a base plate, a top plate and an outer tubular shell. The base plate serves as the mounting platform for the compliant fingers, which are secured in place by means of screws. The top plate serves a dual mounting function, providing an interface for the electronics stack housed within the body, and for a custom end-effector flange mounted externally, enabling the gripper to be attached on a robotic manipulator. The two plates are connected by a PMMA cylindrical outer shell, which provides structural rigidity and environmental protection for the internal wiring and electronics, while its transparency allows visual inspection of the internal components for debugging and demonstration purposes. The compliant fingers are mounted to the base plate and extend downward from the rigid body, forming the grasping elements of the gripper.

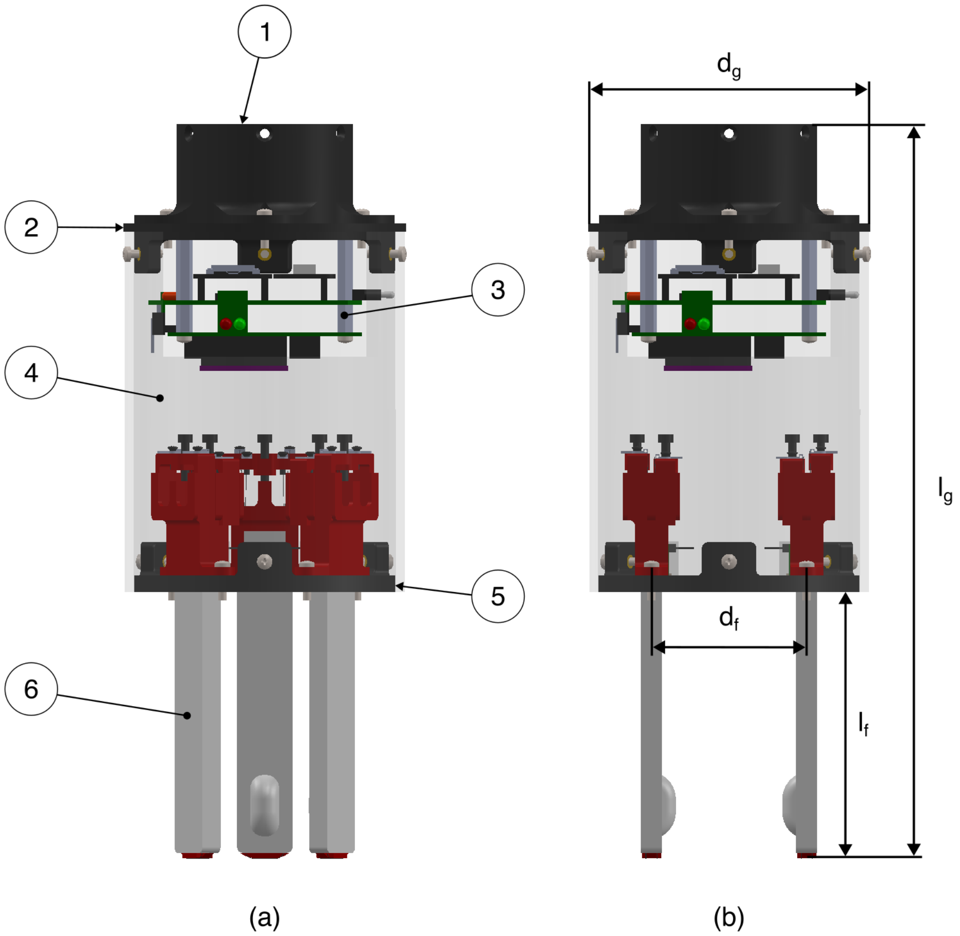

Figure 2.1: **(a)** Developed gripper functional design, three fingers configuration. **1**: End-effector mounting flange. **2**: Upper plate. **3**: Electronics stack. **4**: Outer structural shell. **5**: Base plate. **6**: Soft fingers. **(b)** Developed gripper, two fingers configuration.

In the following table the main dimensions of the gripper assembly are summarized, see Figure 2.1 (b).

Table 2.1: Main dimensions of the gripper assembly

Dimension	**Description**
d_g	Outer diameter of the gripper body
d_f	Finger mounting circumference diameter
l_g	Total length of the gripper
l_f	Total length of the finger outside the gripper body

Two configurations of the gripper were taken into consideration: a three-finger configuration and a two-finger configuration. In the three-finger configuration, the fingers are equally spaced along a circumference at 120 deg intervals, and the gripper is intended to approach and grasp objects from above in an enveloping grasp mode. In the two-finger configuration, two fingers are mounted opposing each other in a parallel gripper architecture, designed primarily for grasping elongated objects through a lateral approach. To accommodate both configurations, two dedicated base plates were designed, one for each configuration, see Figure 2.2. Switching between the two configurations simply requires swapping the base plate.

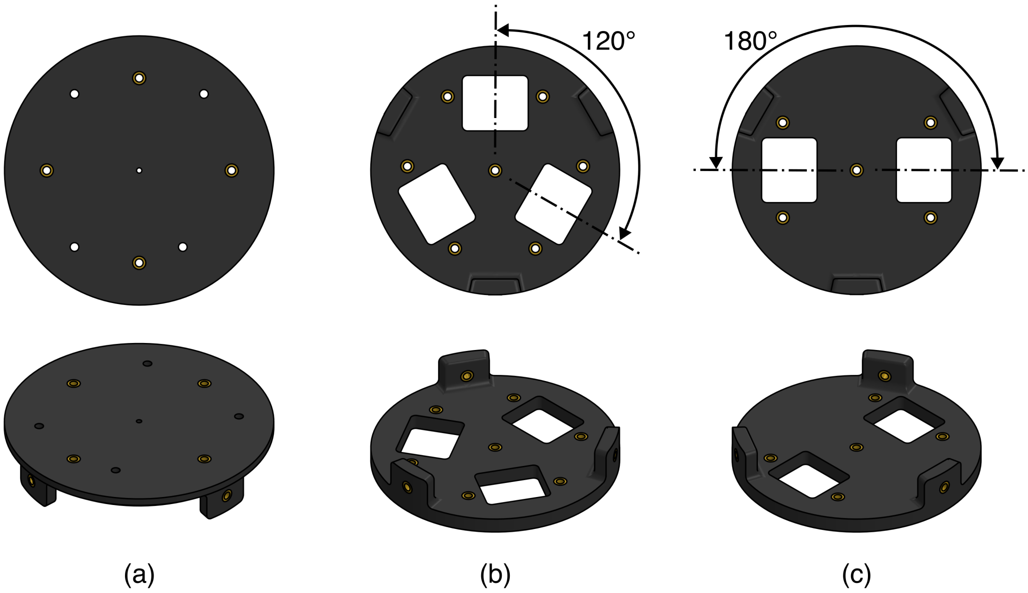

Figure 2.2: **(a)** Top plate. Threaded insert holes are used to mount the robotic manipulator flange and connect the plate to the outer structural shell, through holes to secure the electronics stack. **(b)** Base plate, three fingers configuration. Cutouts and threaded insert holes are used to secure fingers in place and connect the plate to the outer structural shell. **(c)** Base plate, two fingers configuration.

2.2 Electronics

The electronics of the gripper had been developed to control the actuation of the fingers, acquire data sensors and manage the I/O signal exchange with a remote control unit.

As previously described in the first Chapter 1, the SMA wire tendons contract upon heating above an activation temperature $\mathrm{A_s}$. The heating is achieved by exploiting the *Joule effect*, whereby an electrical current is passed directly through the SMA wires. An important design choice concerns whether to control all fingers as a single unified actuator or as independent actuators. The latter implementation would allow for more sophisticated grasping strategies, enabling adaptive finger positioning during object approach and grasp. However, this comes at the cost of a significantly increased electronics complexity and, more critically, a considerably more demanding control strategy.

One of the inherent advantages of soft actuators is that much of the work involved in adapting to different object geometries, such as wrapping around irregular shapes and compensating for positional misalignment, is passively handled by the inherent compliance of the soft structure itself. For this reason, and given that independent finger control falls outside the primary scope of this work, the fingers are treated as a single unified actuator, containing system complexity at this stage of development.

This implies three defined operational states of the gripper:

- In the closed configuration, the agonist tendons of all mounted fingers are simultaneously actuated.
- In the open configuration, the antagonist tendons of all fingers are simultaneously actuated.
- In the neutral configuration, all tendons are not actuated and the fingers rest in their natural relaxed position.

Under this assumptions, the SMA tendons can be modeled as resistive elements and wired accordingly into two separate series circuits: an agonist series and an antagonist series. This wiring configuration ensures that an equal current flows through each tendon within the same series, guaranteeing coordinated actuation dynamics across all fingers.

Building on this wiring scheme, the developed electronics architecture, summarized in the schematic in Figure 2.3, operates as follows. Actuation commands are entered by the user via a serial interface on a PC, used as a remote control unit. Through a USB cable, these commands and power are transmitted to a microcontroller housed within the gripper body. The microcontroller interprets the received commands and switches two digital MOSFET switches accordingly, powering either the agonist tendon series, closing the gripper, or the antagonist tendon series, opening the gripper. Electrical current is supplied by an external power supply operating in Constant Current (C.C.) mode, which simultaneously functions as a current regulator, compensating for the absence of a dedicated current regulation circuit in the custom electronics.

Two status LEDs are connected to the microcontroller, one for each tendon series, providing a visual indication of the current actuation state of the gripper.

The electronics architecture also integrates several sensors. Two current sensors are used to continuously monitor the current flowing through each tendon series. For this purpose, they are wired in series with the respective MOSFET switches within the main electronics stack. Additionally, pressure sensors are used to acquire pressure data from which tactile contact information is derived. One pressure sensor per finger is embedded within the silicone matrix and directly connected to the respective fingertip bladder. Depending on the gripper configuration, two or three pressure sensors are wired to the circuit.

Both current and pressure sensors communicate with the microcontroller via the I^2C bus[1]. To uniquely identify each device on the bus, a distinct I^2C address is assigned to each sensor. While some commercial sensors offer configurable addresses, allowing multiple instances of the same sensor to coexist on a single I^2C bus, others feature fixed addresses, making it impossible to connect more than one such sensor on the same bus without additional hardware. In the present implementation, the pressure sensors employed feature fixed I^2C addresses, which required the inclusion of an I^2C multiplexer in the electronics architecture to enable the microcontroller to address each pressure sensor independently.

---

[1] I^2C (Inter-Integrated Circuit) is a synchronous, multi-device serial communication protocol that enables multiple sensors and peripherals to share a common two-wire interface, a serial data line (SDA) and a serial clock line (SCL), in addition to power and ground connections. Its simplicity and low wiring requirements make it widely adopted in embedded and robotic systems.

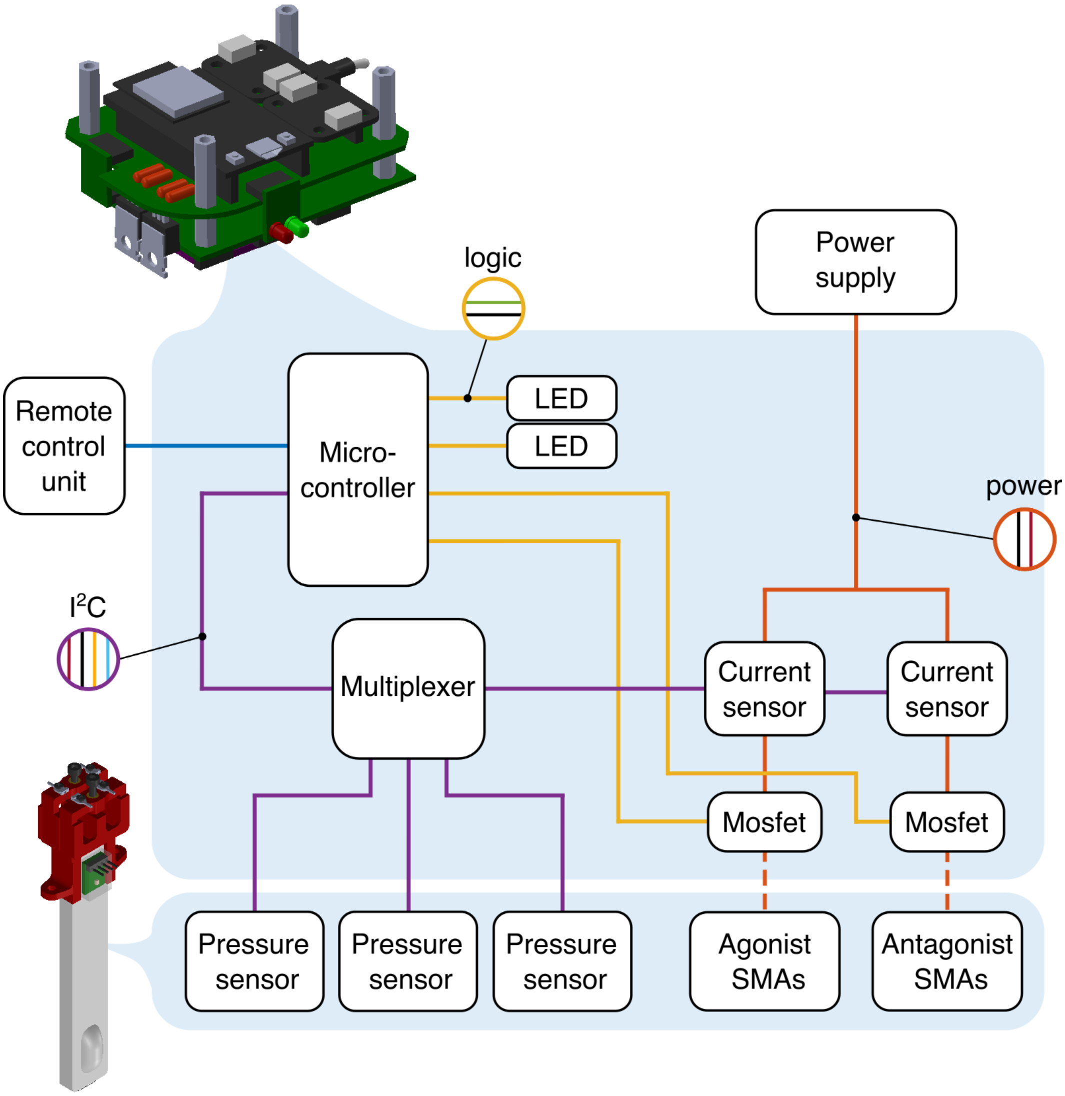

Figure 2.3: Electronics architecture. USB in blue. I^2C bus in purple (V_{dd}, GND, SDA, SCL). Power line in orange (0-30 V). Logic line in yellow (0-3.3 V).

Figure 2.4 shows the developed electronics stack assembly with its main components labeled. The stack consists of two layers separated by commercial spacers, which also serve as mounting points to the top plate of the gripper body. The top layer houses the microcontroller, the current sensors, and the power circuit, along with a main power switch allowing the stack to be de-energized when needed. The bottom layer accommodates the I^2C circuit, including the multiplexer. Electrical connection between the two layers is realized through a dedicated bridging board. The status LED board is placed at the front of the stack for easy visibility. The pressure sensors are mounted on dedicated boards, which are subsequently embedded within the silicone matrix of the finger bodies. The electronics stack was designed with modularity as a guiding principle, ensuring that all main components can be easily disassembled and replaced independently without requiring resoldering of the entire assembly. The details of the physical realization of the stack, including wiring, connectors, and soldering, are covered in the prototyping chapter. The detailed circuit schematic of the electronics architecture is reported in Appendix B.

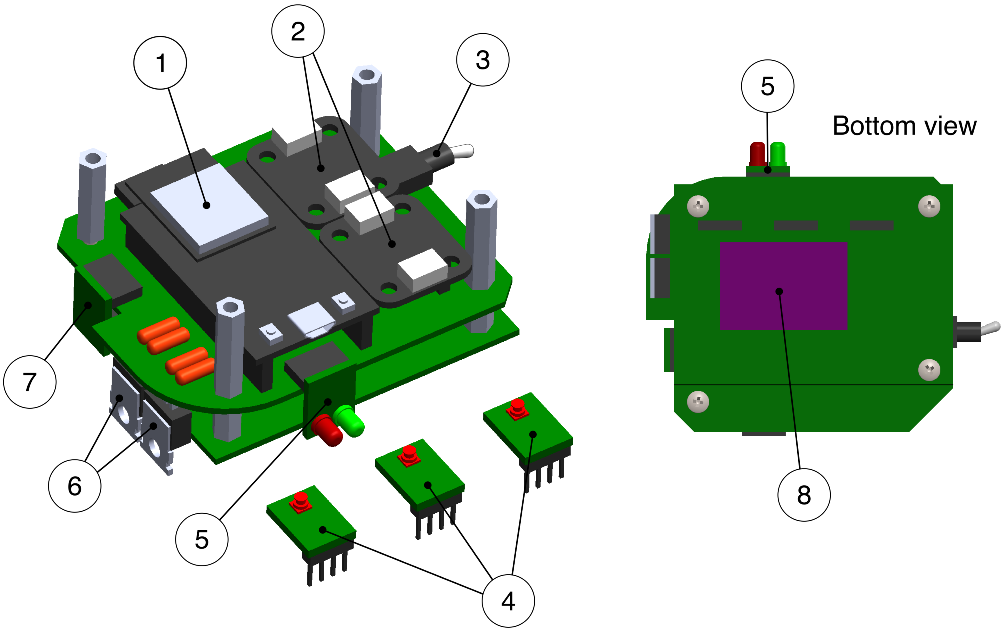

Figure 2.4: Electronics stack functional design. **1**: Microcontroller. **2**: Current sensors. **3**: Switch. **4**: Pressure sensor boards. **5**: LED board. **6**: MOSFET. **7**: Bridging board. **8**: Multiplexer.

2.3 Finger

The developed finger consists of two main parts: a rigid base and a main body made of soft material. The compliant body is a parallelepiped-shaped silicone structure, characterized by a rectangular cross-section with the short side defining the finger thickness and the long side defining its width. It houses two SMA wire tendons and an integrated tactile sensing system. The tendons are responsible for the actuation of the finger. The agonist tendon lies on a plane parallel to the neutral midplane of the finger, offset towards the front face by a distance $\mathrm{d_{SMA}}$. This offset represents the moment arm of the tendon-driven mechanism and is a critical design parameter, as it directly determines the bending moment generated upon tendon contraction. The antagonist tendon lies on a plane symmetric to that of the agonist with respect to the neutral midplane. When the agonist tendon contracts, the finger bends toward the plane containing it, and vice versa for the antagonist tendon. A simplified analytical model of the tendon-driven mechanism is reported in Appendix A. The inclusion of the antagonist tendon serves two purposes. First, it enables active recovery of the neutral position, rather than relying solely on the passive elastic restoring force of the silicone matrix. This is particularly advantageous given the thermal dynamics of SMA wires, whose cooling, and thus shape recovery, can be slow when the wires are embedded within a silicone matrix rather than exposed to free air. Second, the antagonist tendon enables actuation of the finger in the opposite direction. This allows the gripper to spread its fingers outward before closing around an object, enabling the grasping of objects larger than the finger mounting circumference diameter reported in Table 2.1, or alternatively to grasp hollow objects from the inside. Both tendons follow a U-shaped trajectory along the finger length, entering from the base, running toward the tip, being redirected, and returning to the base, effectively traversing the finger length twice. The tendons are routed through silicone tendon sheaths embedded within the silicone matrix. These sheaths serve three functions: they protect the silicone matrix from direct contact with the SMA wires during contraction, they guide the tendons along their path, reducing friction, and they allow independent tendon replacement in case of damage, without the need to recast the entire finger, see Chapter 3 for more details. It should be noted that the tendon sheaths extend only within the silicone matrix. At the fingertip, where the tendons are redirected, they are briefly exposed to the exterior before reentering the matrix. Here, a rigid tendon routing insert is present, held in position by the two tendons themselves. This element acts as a passive pulley, guiding the tendons at the point of redirection corresponding to the bottom of the U-shaped trajectory. Its rigidity prevents tendon contraction in this region, concentrating the bending deformation along the finger length and protecting the fingertip silicone matrix from being damaged by the tendons.

The space within the silicone matrix not occupied by the tendon sheaths is exploited to integrate a tactile sensing system. A rounded fingertip bladder protrudes from the frontal face of the finger, forming a hollow chamber. Its geometry, a rounded parallelepiped, hollowed internally, was specifically designed to maximize compliance: the curved walls deform in bending rather than compression upon contact, maximizing deformation for the limited actuation forces available. The bladder features a compliant silicone membrane that separates the internal volume from the exterior. The bladder is connected via an internal channel, embedded within the silicone matrix, to the base of the finger, where a miniature pressure sensor is located, also fully embedded within the silicone matrix, with only its electrical pins accessible from the exterior. These pins are connected to the electronics stack by means of a dedicated cable assembly, terminated with a connector for easy integration into the electronics architecture. Under normal conditions, the bladder and internal channel are filled with air at atmospheric pressure. Upon contact, the bladder membrane deforms, reducing the internal cavity volume and generating a measurable pressure increase. This pressure variation is detected by the sensor, from which tactile contact information can be derived. The compliant body is assembled onto the rigid base by inserting its proximal end into a dedicated cavity. This form-fit coupling, combined with the pretensioned tendons, acts as a fixed structural constraint between the compliant body and the base. The rigid base serves three functions. First, it provides the structural connection between the finger and the gripper base plate, featuring two clearance holes for the fixing screws, visible in Figure 2.1. Second, it houses the tendon fixation and pretensioning mechanism, shown in Figure 2.6 (c). On both sides of the base, two parallel slots act as prismatic guides for two C-shaped brackets, which can slide independently along them. Each bracket features three threaded holes: the two lateral ones serve as tendon fixing points, while the central one houses the tensioning screw. This screw bears against the base surface, acting as a lead screw, so that tightening or loosening it advances or retracts the bracket, directly adjusting the tendon pretension. It is worth noting that the pretensioning system plays a crucial role in the finger correct functioning: without it, part of the SMA contraction would be consumed in taking up slack before any bending deformation occurs [2]. Third, the base provides the electrical interface between the tendons and the electronics stack. The SMA wires are terminated with commercial crimp ferrules featuring a through hole, see Figure 2.6 (b). The fixing screws pass through these holes and are secured to the C-shaped brackets. A ring connector, soldered to an electrical wire, is stacked together with the crimp ferrule and clamped in a sandwich configuration by the same screw, simultaneously achieving mechanical fixation of the tendon and electrical connection to the control circuit, Figure 2.6 (a).

---

[2] Slack is also introduced during assembly, since the tendons are cut to size and terminated with ferrules manually, making it impossible to control their final length with sufficient precision. The tensioning screw provides the means to compensate for this.

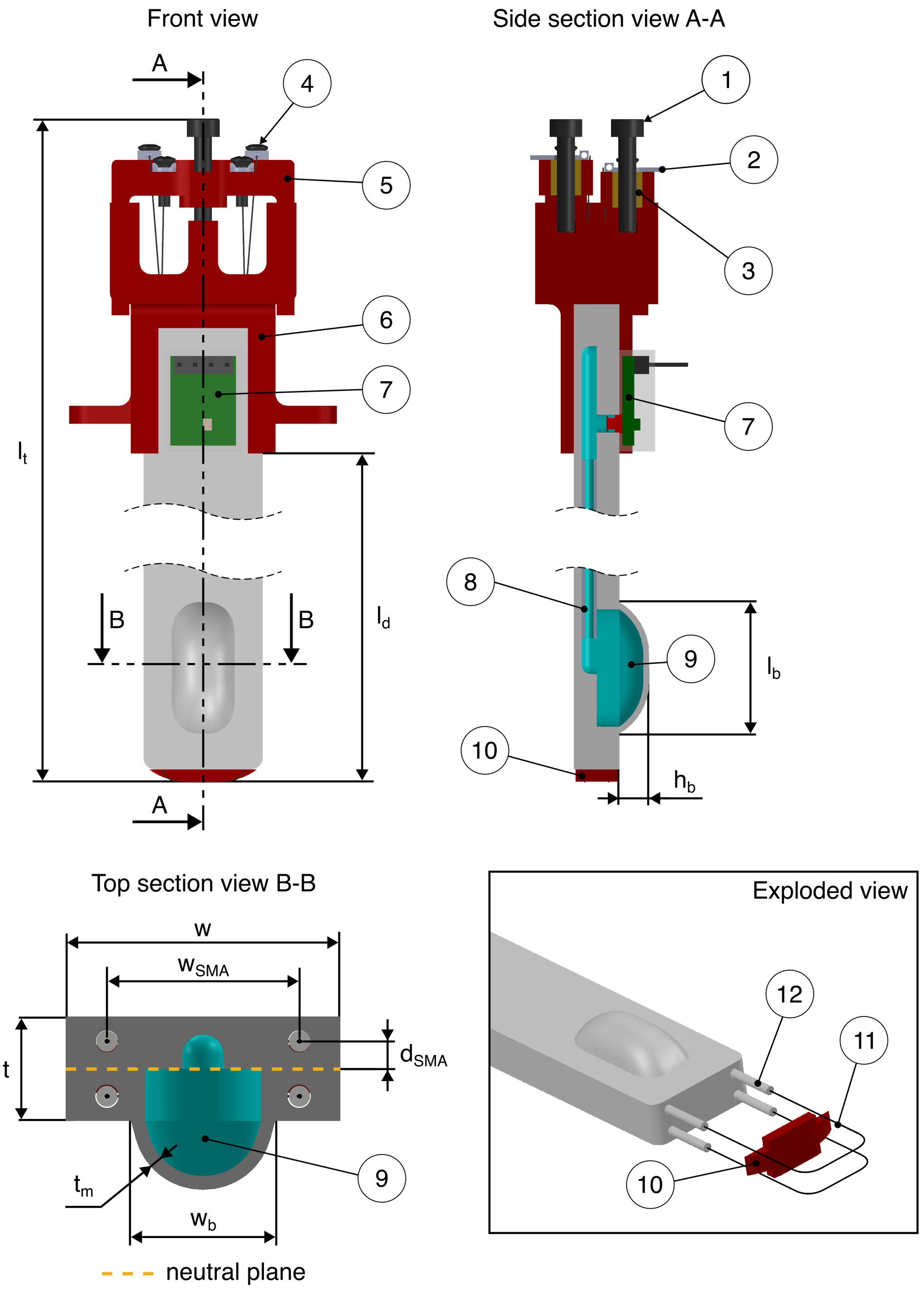

Figure 2.5: Finger functional design. **1**: Tensioning screw. **2**: SMA wire crimp. **3**: Threaded insert. **4**: Fixation screw. **5**: C-shaped bracket. **6**: Finger rigid base. **7**: Pressure sensor board. **8**: Air channel. **9**: Fingertip compliant bladder. **10**: Tip Routing Insert. **11**: SMA wire tendon. **12**: Bowden cable/Tendon sheath.

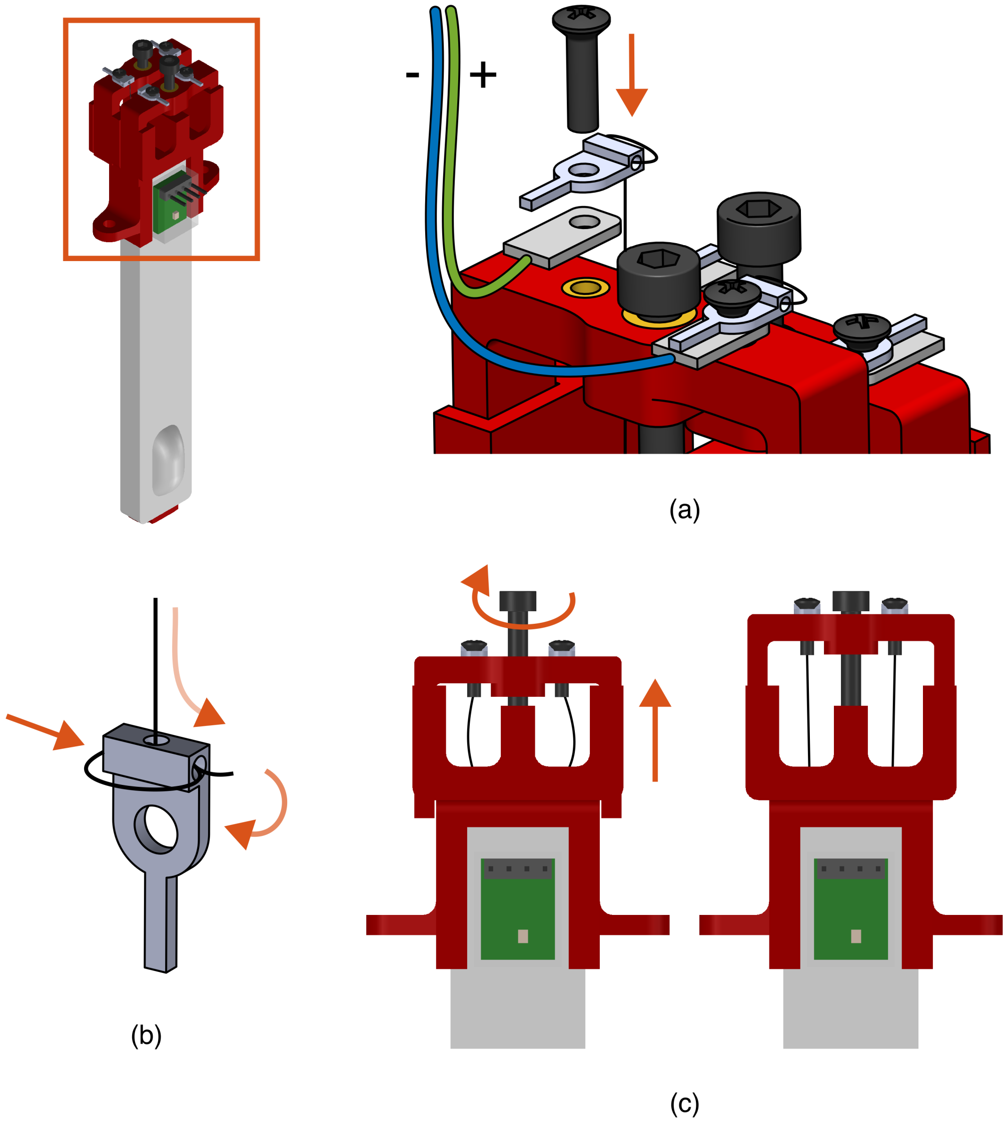

Figure 2.6: **(a)** Electronic connection and mechanical fixation of the tendon wires are achieved clamping the wire crimp and a ring connector with a single screw secured to the C-shaped bracket. **(b)** SMA wire tendon crimping method. The SMA wire is threaded through a commercial crimp and then secured in place using crimping pliers (not shown). **(c)** Tensioning system. Adjusting the tensioning screw the C-shaped bracket slides up and down regulating the pretension of the tendons.

In the following Table 2.2 the main dimensions of the finger assembly are summarized, see also Figure 2.5.

Table 2.2: Main dimensions of the finger assembly

Dimension	**Description**
l_t	Total length of the finger
l_d	Deformable length of the finger
w	Width of the finger
t	Thickness of the finger
w_{SMA}	Width of the U-shaped trajectory of the tendons
d_{SMA}	Offset of tendon planes to neutral plane
w_b	Width of the bladder
h_b	Height of the bladder
t_m	Thickness of the bladder membrane

2.4 Alternative multi-bladder finger

An alternative finger design was developed, featuring an enhanced tactile sensing system while keeping the same actuation architecture (SMA wire tendons, tendon sheaths, tendon routing insert, and rigid base) as the previously described version. A CAD drawing of this alternative design is reported in Figure 2.7.

The key difference lies in the number and distribution of fingertip bladders. Rather than a single bladder located at the fingertip, this design integrates three independent bladders distributed along the finger length: a distal bladder, positioned at the fingertip in the same location as in the original design; a medial bladder, located approximately at the midpoint of the finger length; and a proximal bladder, positioned closer to the base of the finger.

Each bladder is connected to an independent internal channel embedded within the silicone matrix, ensuring that the three sensing cavities are fluidically isolated from one another. A custom sensor board, housing three pressure sensors, is embedded within the silicone matrix at the base of the finger, one sensor per channel, replacing the single sensor board of the original design.

This configuration enables contact detection at three distinct points along the finger length, providing significantly richer tactile information compared to the single-bladder design.

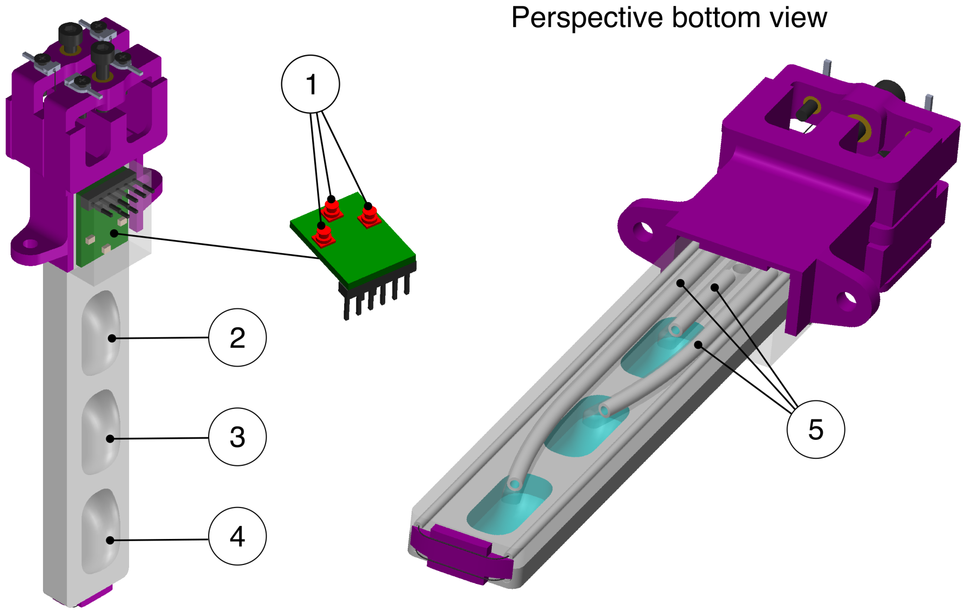

Figure 2.7: Multi-bladder finger functional design. **1**: Three pressure sensors on a single custom board. **2**: Proximal bladder. **3**: Middle bladder. **4**: Distal bladder. **5**: Three independent air channels connecting each pressure sensor to one bladder.

Chapter 3

Prototyping

This chapter covers the prototyping process of the developed soft gripper system. The electronics production is described first, detailing the assembly of the custom multi-layer stack. Subsequently, the finger prototyping pipeline is presented, covering the mold design, casting process, and integration of the sensing and actuation components within the silicone matrix. Finally, the manufacturing of the 3D printed mechanical components and the final assembly of the complete gripper system are discussed.

3.1 Electronics

The realization of the physical prototype of the electronic board follows the functional schematics presented in the previous chapter 2.2.

The first step consisted in the selection of the commercial components required to realize the architecture, summarized in Table 3.1.

Table 3.1: Selected commercial components

Component	Commercial Reference	Key Specification
Microcontroller	ESP32 WROOM [25]	38 GPIO, Wi-Fi, Bluetooth
Current sensor	INA219 [26]	3.2A max, 12-bit ADC
Pressure sensor	MS5837-30BA [27]	0-30 bar, 24-bit ADC, 3.3×3.3 mm
I^2C Multiplexer	TCA9548A [28]	8 I^2C channels

An ESP32 WROOM was chosen as the microcontroller for its suited processing power, the availability of numerous GPIO pins, and its compact dimensions. Notably, the ESP32 features built-in Bluetooth and Wi-Fi modules, which were tested and confirmed to enable remote gripper control and wireless sensor data streaming via TCP/IP protocol. This capability was not included in the final design of this work in order to limit complexity, but it represents a possible direction for future development. For current sensing, two INA219 sensors by Adafruit were selected, offering sufficient precision and a measurement range well suited to the currents involved in finger actuation. The TCA9548A was chosen as the I^2C multiplexer, a compact and cost-effective standard component offering up to eight independent I^2C channels. Finally, the MS5837-30BA pressure sensor was selected for its reduced dimensions, necessary to fit within the finger base, and for its high resolution. The selection of passive components such as resistors and capacitors, as well as the MOSFET, is detailed in the circuit schematic reported in Appendix B.

The realization of the electronics stack required standard soldering equipment and materials. A temperature-controlled soldering station was used throughout the assembly process, paired with a ventilation fan to ensure safe working conditions. Thin gauge soldering wire and soldering flux were used to achieve clean and reliable solder joints. Standard tools such as wire cutters, wire strippers, and pliers completed the workbench setup.

Both layers of the stack were realized using standard 2.54 mm pitch perforated boards as substrate. These prototyping boards are particularly convenient for several reasons: they are easy to solder for both direct wire connections and connector mounting, they can be readily cut to size using a saw and drilled as needed, and their inherent rigidity allows them to function not only as an electrical substrate but also as a structural component of the stack. Pin header connectors were used throughout to pursue a modular architecture, allowing the breakout boards of the commercial components and the custom auxiliary boards to be individually disassembled and replaced without resoldering. Throughout the assembly, a consistent convention was followed: female pin header connectors were used on the higher potential side of each connection and male connectors on the lower potential side, ensuring unambiguous and safe mating of all boards. All other components and wiring were soldered directly to the boards.

The top layer was assembled first. On its upper face, the main power switch and all pin header connectors were placed and soldered in their prescribed locations to accommodate the breakout boards. On its lower face, the internal side of the stack, the power circuit and the I^{2}C circuit sections related to the current sensors were wired and soldered directly to the board. The bottom layer was then produced accordingly, with its I^{2}C circuit soldered on its upper face facing the interior of the stack, and the multiplexer connector and sensor cable connectors mounted on its lower face.

Several additional small boards were realized as perforated board cutouts. A bridging board was produced to establish the electrical connection between the two layers, carrying the four lines of the I^{2}C bus: V$_{dd}$, GND, SCL, and SDA. The status LED board was realized by wiring each LED in series with a current limiting resistor.

The pressure sensor boards were produced following the same approach. The MS5837-30BA sensor was purchased in its bare die configuration, without the recommended decoupling capacitor. A small perforated board cutout was therefore prepared. On one side, the pressure sensor was carefully soldered following the thermal recommendations of the datasheet to avoid heat damage. On the other side, the decoupling capacitor, wire traces, and pin header connector were soldered. This configuration ensures that the sensor side of the board is free of any additional components, which was necessary to allow the board to be mounted inside the finger body with the sensor facing directly into the internal cavity. Both the single-sensor and three-sensor board variants were realized in this way.

Once both layers and all auxiliary boards were completed, the electronics stack was assembled by plugging all boards into their respective connectors and securing the structure using commercial threaded hex standoffs. These are small metal columns with a hexagonal cross-section, internally threaded at both ends, allowing them to be connected to form rigid multi-layer structures. Seven standoffs were used to fix the two layers at a prescribed distance, while simultaneously serving as mounting points for the complete stack onto the top plate of the gripper body.

The overall dimensions of the stack were kept compact to fit within the internal volume of the gripper body shell. It is worth noting that a significant size reduction could be achieved through the design of a custom PCB, which however falls outside the scope of the present work.

The assembled electronics stack is shown in Figure 3.1, with main components labeled.

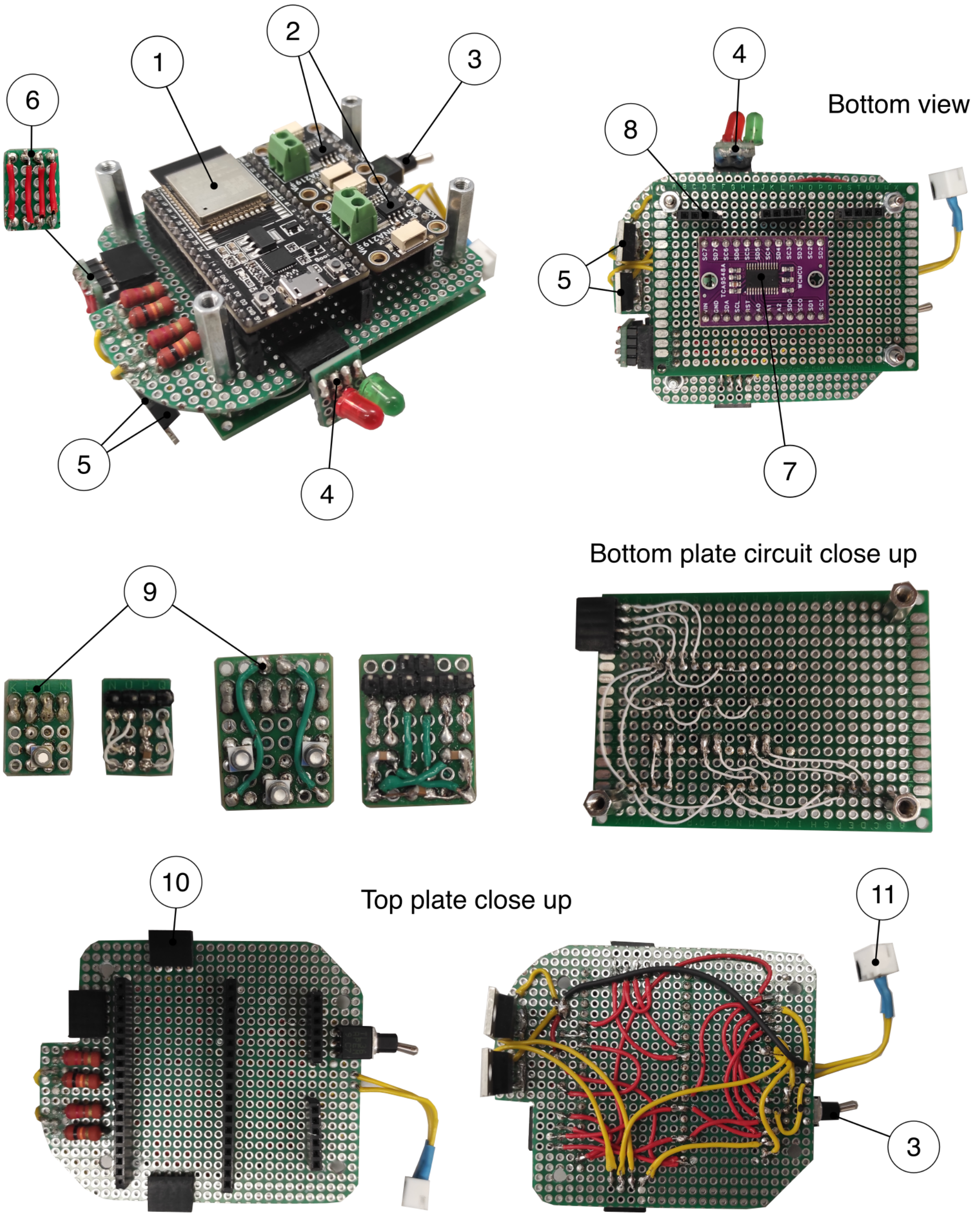

Figure 3.1: Manufactured electronics. **1**: Microcontroller. **2**: Current sensors. **3**: Switch. **4**: LED board. **5**: Mosfet. **6**: Bridging board. **7**: Multiplexer. **8**: Pressure sensors connectors. **9**: Pressure sensor boards, 1- and 3-sensors variants. **10**: SMA tendons power connector. **11**: Power supply connector.

3.2 Finger

The finger, whose design was defined in the previous chapter, was manufactured by combining two different processes: the compliant body was produced by silicone casting, while the rigid components were 3D printed.

The rigid base, the two C-shaped brackets, and the tendon routing insert were 3D printed using FDM technology.[1] PLA was selected as the printing material for its ease of printability, low toxicity, and sufficient structural characteristics for the application. The printer used was a Bambu Lab X1 Carbon, due to its high accessibility, fine layer resolution (0.08 mm), and fast printing speeds of up to 500 mm/s [32], well suited for rapid prototyping.

As a preliminary step, the CAD models were modified by reducing the diameter of all holes slightly below the nominal value. This was done to compensate for dimensional inaccuracies that the FDM process can introduce, ensuring that the final hole dimensions after post-processing would match the design specifications. The STL files were then imported into the slicing software, where printing parameters such as layer thickness, infill density, and support structures were adjusted according to the geometry of each part. The resulting G-code was then sent to the printer and the parts were produced.

Once printed, basic post-processing was carried out to remove support structures and smooth out coarse surfaces. All holes were then brought to their nominal diameter using a drill and appropriate drill bits. Finally, brass threaded inserts were heat-set into the C-shaped brackets, two M2 inserts for the tendon fixing screws and one M3 insert for the tensioning screw, per bracket.

The soft body of the finger was manufactured through silicone casting. The first critical step was to select the casting strategy and design dedicated molds accordingly. Two main options were considered: a single cast in a closed mold, or multiple casts in separate open molds. While the presence of embedded elements such as the tendon sheaths did not represent a significant constraint for either option, the geometry of the internal sensing cavity was problematic for the single cast approach. A single cast would have required an internal core matching the cavity geometry, which could not have been extracted after curing due to the undercut geometry of the bladder volume at the end of the channel, a limitation that persists even considering the elasticity of the silicone. For this reason, multiple casting in open molds was selected. [2]

The finger body was therefore divided into two halves along its thickness, with the parting plane coinciding with the neutral midplane of the tendon-driven actuation system. Two dedicated open molds were designed accordingly.

---

[1] FDM, which stands for Fused Deposition Modeling, is an additive manufacturing process in which a thermoplastic filament is melted by a heated nozzle and deposited layer by layer onto a build platform, guided by a CNC motion system. Each deposited layer bonds to the previous one upon cooling, progressively building the desired geometry from the bottom up.

[2] Open molds also offer additional practical advantages over closed molds: the large exposed surface facilitates pouring and distribution of the silicone, allows visual inspection during casting to prevent air bubble entrapment and unfilled cavities, and promotes more uniform curing through greater contact between the silicone and the atmosphere.

The first mold consists of a rectangular vat with a rib protruding from its bottom face, running along its length. This feature produces a corresponding groove in the cast half, forming the internal sensing channel. The free surface of this cast constitutes the back face of the finger, while the bottom face corresponds to the parting line of the finger.

The second mold also consists of a rectangular vat, but features a recess at its bottom towards one end, producing the geometry of the protruding fingertip bladder in the cast half. To hollow out the bladder and control the membrane wall thickness, a custom punch was designed. The punch geometry matches the internal volume of the bladder and is pressed by external weights into the mold immediately after pouring the silicone. Precise alignment between the punch and the mold recess is achieved through a form-fit between alignment features present on both parts. The second mold also includes a small cylindrical pillar extruded from its bottom face, which produces the short channel connecting the pressure sensor to the main sensing channel. In this mold, the free surface of the cast constitutes the parting line of the finger, while the bottom face defines the external front face.

To embed the tendon sheaths within the silicone matrix, commercial silicone tubing was used and placed in the molds prior to casting. Four through holes were designed in the short walls of each mold, two per side, serving as guides for the tubing. The sheaths were cut to a length slightly exceeding that of the finger, fed through the holes, and held straight and taut during casting and curing by means of light pretension applied with pegs. The first mold hosted the sheaths for the antagonist tendons and the second those for the agonist tendons.

In Figure 3.2 the CAD drawing of the single-bladder variant finger molds is reported, main features are labeled.

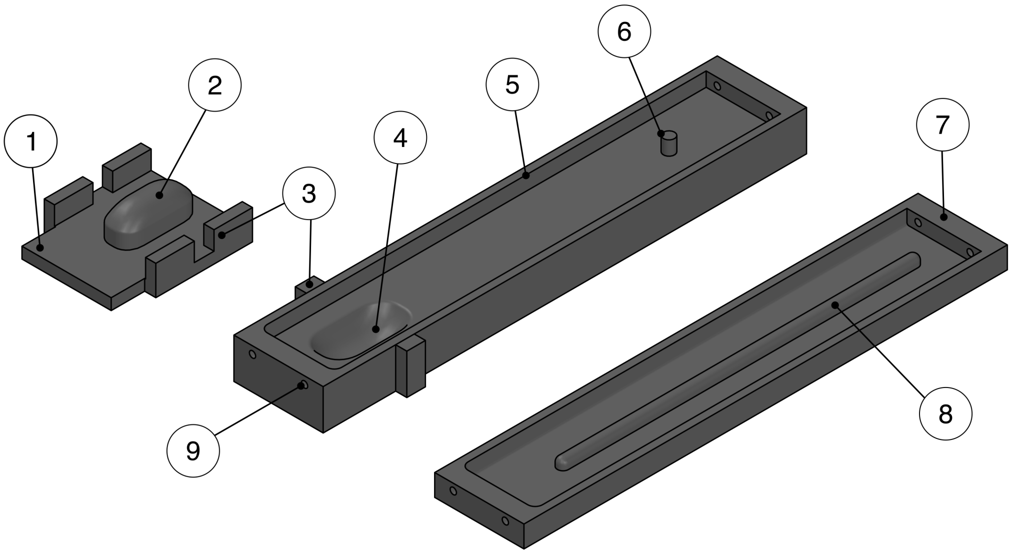

Figure 3.2: Single-bladder variant finger molds. **1**: Punch plate. **2**: Punch volume. **3**: Alignment features. **4**: Bladder recess. **5**: Front half mold. **6**: Cylindrical pillar for pressure sensor. **7**: Back half mold. **8**: Rib for sensing channel. **9**: Guide through holes for tendon sheaths.

The same casting strategy was adopted for the multi-bladder finger variant, with modifications to the mold geometry to accommodate the three-bladder sensing system. In the first mold, three ribs were designed in place of the single rib, realizing the branched internal channel system connecting each pressure sensor to its respective bladder. In the second mold, three recesses were included, one per bladder position. Accordingly, the single punch was replaced by a punching plate featuring three punches distributed along its length. Since the punching plate covers the entire free surface of the second mold, spillage holes were included in the plate to allow excess silicone to escape during pressing.

In Figure 3.3 the CAD drawing of the multi-bladder variant finger molds is reported, main features are labeled.

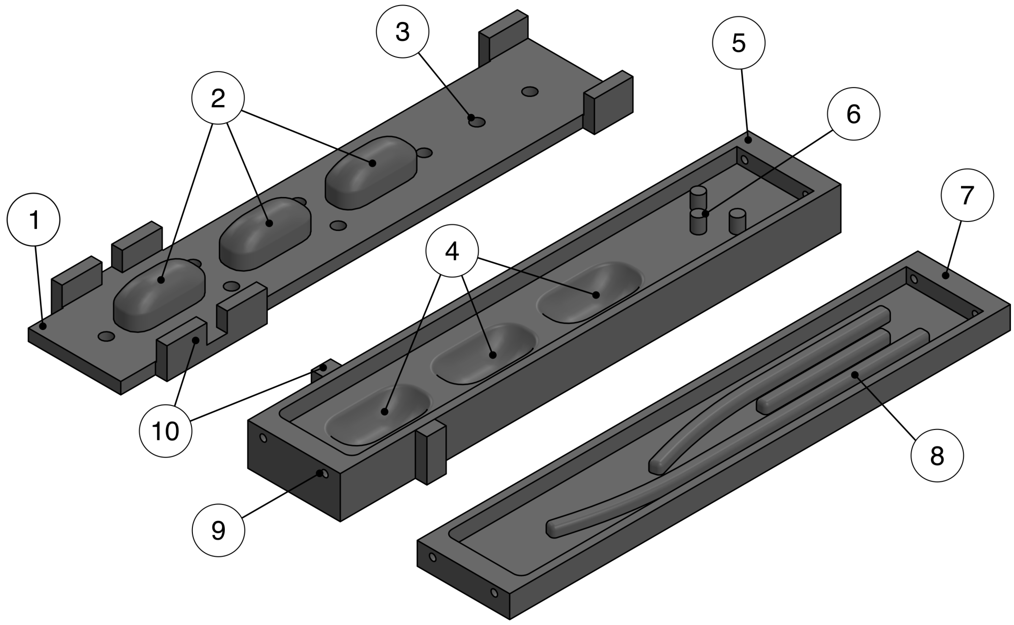

Figure 3.3: Multi-bladder variant finger molds. **1**: Punch plate. **2**: Punch volumes. **3**: spillage holes. **4**: Bladders recesses. **5**: Front half mold. **6**: Cylindrical pillars for pressure sensors. **7**: Back half mold. **8**: Ribs for sensing channels. **9**: Guide through holes for tendon sheaths. **10**: Alignment features.

Once the mold design was finalized, the molds were 3D printed following the same procedure described above for the rigid finger components [3].

The silicone selected for the casting process was the PlatSil® Gel-25 by Polytek, whose main characteristics are reported in Table 3.2.

Table 3.2: Main characteristics of PlatSil® Gel-25 by Polytek, from manufacturer datasheet [30].

Property	**Value**
Mix ratio	1:1
Mixed Viscosity (cP)	3500
Pot life	5 min
Demold time	60 min
Shore hardness	A25

---

[3] Some molds were also produced using an SLA resin printer. While resin molds offer higher surface quality, print times are longer and chemical incompatibility between uncured resin and platinum-catalysed silicone can inhibit curing. To prevent direct contact between the resin walls and the silicone, the mold inner surfaces were coated with acrylic spray paint prior to casting.

Even featuring a notably short pot life its low mixed viscosity makes it particularly manageable during the preparation steps and the casting process. Its short demold time is ideal for fast prototyping. Finally, the cured silicone hardness was well suited to the desired compliance of the finger, ensuring sufficient flexibility for both actuation and tactile sensing.

The complete manufacturing process of the finger body is described in the following and summarized in Figure 3.4. As a first step, the molds were prepared by placing the tendon sheaths in position as described above. The silicone was then prepared by weighing parts A and B using a precision laboratory scale to achieve the correct 1:1 mix ratio, after which the two parts were thoroughly mixed. The mixture was placed in a vacuum chamber for 2 minutes to degas, removing the air bubbles incorporated during mixing. The degassed silicone was subsequently poured into the molds [4]. For the front half mold, the punch was pressed onto the poured silicone immediately after casting and held in place by means of external weights for the entire curing time.

After the curing time elapsed, the two halves were demolded. The next step consisted in joining them to form the complete finger body. A fresh batch of silicone was prepared and used as a bonding agent between the mating surfaces of the two halves. A known risk of this process is the infiltration of fresh silicone into the sensing channel, which would clog it and compromise the tactile sensing system. To prevent this, a section of commercial silicone tubing, ID 1.5 mm / OD 2.5 mm, was inserted into the channel prior to bonding. This tubing is not removed after curing, as it bonds permanently to the surrounding silicone matrix. Its flexibility is comparable to that of the finger body material, ensuring that its presence does not negatively affect the actuation performance, consistently with the design rationale of the tendon sheaths.

To apply controlled and uniform pressure during the bonding phase without deforming the protruding fingertip bladder, a dedicated 3D printed pressing mask was designed and used. This mask covers the two halves and distributes the load of the external weights evenly across the finger body, protecting the bladder geometry from unwanted deformation or unintended bonding in an incorrect configuration. The assembly was left to cure under the mask and weights for the prescribed curing time.

After curing, the excess tendon sheath material protruding from the finger body was trimmed flush. The pressure sensor board was then installed by inserting the sensor into the small channel produced by the cylindrical pillar feature of the mold, ensuring the sensor is positioned directly within the internal cavity of the finger. To embed the sensor board within the silicone matrix and fluidically seal the internal cavity from the atmosphere, a fresh batch of silicone was prepared and poured over the sensor board using a dedicated 3D printed formwork, which was removed once the silicone had cured. At this point, the compliant finger body was complete and ready for final assembly.

Flexinol® LT actuator wires, by Dynalloy, were selected as SMA tendons. In par-

---

[4] A release agent spray can be applied to the mold surfaces prior to casting to facilitate demolding of the cured silicone part.

ticular the Low Temperature (LT) SMA actuator wire with 0.2 mm diameter model was chosen for its high pull force but still contained recommended current. Its main characteristics are reported in Table 3.3.

Table 3.3: Main characteristics of the Flexinol® 0.2 mm diameter LT SMA actuator wire, used as tendons, from manufacturer datasheet [31].

Property	**Value**
Diameter	0.20 mm
Resistance	29 Ω/m
Pull force	570 g
Cooling deformation force	228 g
Recommended current (1 s contraction)	660 mA
Cooling time	3.2 s
Activation temperature	70 °C
Maximum strain	4–5%

The recommended current for 1-second contraction reported in the datasheet for the selected wire is 660 mA. According to the manufacturer, this value represents the current level at which the wire fully contracts within 1 second without overheating, and it was adopted as the actuation current throughout the experimental tests, including the pick and place validation. This choice allowed the finger actuation to be controlled in a simple open-loop fashion, without the need for a dedicated current regulation strategy, while ensuring the tendons were not subjected to thermal damage from excessive current. It should be noted that the manufacturer's note specifies that wires of diameter up to 0.15 mm can be left on continuously at this current level without overheating. The wire used in this work has a diameter of 0.20 mm, which slightly exceeds this threshold. Nevertheless, the 660 mA limit was adopted as the reference actuation current, and no signs of thermal degradation were observed during testing. Given the resistivity of 29 Ω/m and a single tendon length of approximately 300 mm, each tendon features a resistance of approximately 10 Ω. Consequently, the agonist and antagonist tendon series in the two-finger and three-finger configurations feature a total resistance of approximately 20 Ω and 30 Ω respectively.

Given the diameter of the selected SMA wire, silicone tubing for the tendon sheaths was chosen with a slightly larger internal diameter of 0.5 mm, allowing the wire to slide freely while maintaining guidance along the U-shaped trajectory.

With the finger body complete and the tendons selected, the final assembly could be carried out. The proximal end of the finger body is inserted into the dedicated recess of the 3D printed rigid base. The SMA wires are then cut to size, routed through the tendon sheaths, and the tendon routing insert is installed. The wire terminations are crimped and fixed together with the electrical connectors to the C-shaped brackets using the fixing screws, as described in the functional design chapter. Finally, the tendon pretension is set by adjusting the tensioning screws, and the finger assembly is complete.

The same procedure was followed to produce the three-bladder finger variant, with minor modifications to account for the different mold geometry. A dedicated pressing mask was designed for this variant to accommodate the three protruding bladders. All other steps remained unchanged.

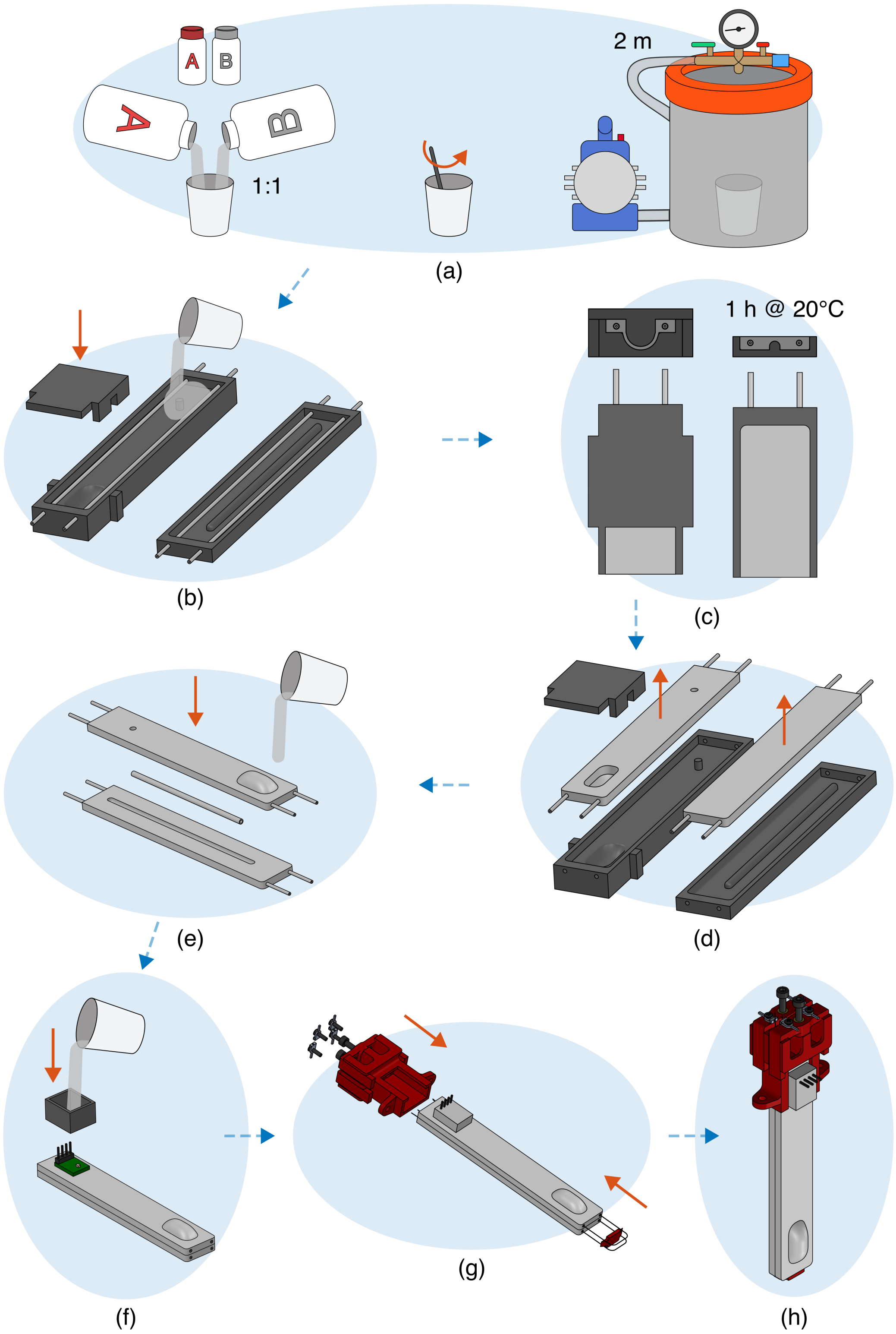

Figure 3.4: Finger manufacturing process. **(a)** Silicone preparation: Parts A and B are mixed and degassed. **(b)** Silicone is poured in the molds. **(c)** Silicone is left completely curing inside the molds. **(d)** The two halves are extracted from the molds. **(e)** The two halves are joined together, internal tubing is added. **(f)** Sheaths excesses are trimmed flush and sensor board is embedded in the finger body. **(g)** Final assembly is performed integrating the rigid parts and SMA tendons. **(h)** Finished produced finger.

Table 3.4: Dimensions of the produced finger, see Table 2.2 and Figure 2.5 for reference.

Dimension	**Value**
l_t	155 mm
l_d	100 mm
w	20 mm
t	8 mm
w_{SMA}	13 mm (18 mm in multi-bladder variant)
d_{SMA}	2.2 mm
w_b	10.5 mm
h_b	22 mm
t_m	1 mm

The bladder dimensions reported in Table 3.4 were selected based on functional and geometric constraints. The length of the bladder was fixed first, proportioned to the finger body length such that the bladder does not hinder the bending deformation of the finger during actuation. The height of the bladder, which determines the internal volume and the degree of protrusion from the finger face, was instead constrained by two bounds. The upper bound was dictated by a geometric consideration: an excessively protruding bladder would interfere with the wrapping of the finger around grasped objects, reducing grasping effectiveness. The lower bound instead was derived from the requirement that the bladder must produce a sufficiently large pressure variation upon contact to be detectable by the pressure sensor. To estimate this, the compression of the internal cavity upon bladder deformation was modeled as an adiabatic process, given the short duration of the deformation event, and thus described by:

$$p \cdot [v(h_b)]^\gamma = \text{constant}$$

where p is the pressure, v is the volume of the internal cavity, which is a function of the height of the bladder h_b and γ is the adiabatic index for air. This relation was then used in an iterative process to check if, choosing a value for h_b was producing a sufficient Δp between final deformed state and initial undeformed state. The selected bladder height satisfies both constraints and represents a compromise between sensing sensitivity and grasping performance.

The membrane thickness and the rounded bladder geometry were likewise determined through an iterative process.

The offset of the tendon planes from the neutral plane, $\mathrm{d_{SMA}}$, was maximized subject to the constraint imposed by the finger body thickness, ensuring sufficient silicone material between the tendon sheaths and the outer surfaces to prevent delamination during actuation.

Finally, it is worth noting that the width of the U-shaped tendon trajectory $\mathrm{w_{SMA}}$, as reported in the table, was increased in the multi-bladder finger variant to accommodate the three independent sensing channels within the silicone matrix.

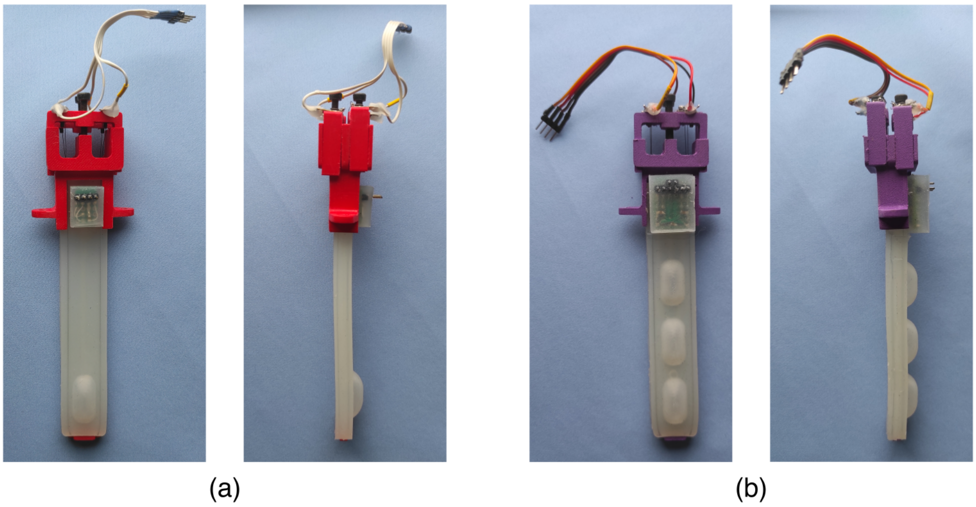
(a) (b)

Figure 3.5: Developed finger. **(a)** Single-bladder variant. **(b)** Three-bladders variant.

3.3 Gripper

This section describes the manufacturing of the gripper structural components and the assembly of the complete system.

The top plate and the two base plates, one for the two-finger configuration and one for the three-finger configuration, were 3D printed following the same procedure described above for the rigid finger components and the molds. Brass threaded inserts were heat-set into the dedicated holes as prescribed.

As described in Chapter 4, the gripper was mounted on the Kinova Gen2 7-DOF commercial manipulator. A custom mounting flange was designed and 3D printed in the same manner to interface the gripper with the robot wrist. The flange features a cylindrical profile with six radial holes for the corresponding set screws.

The outer shell of the gripper body was realized from a section of commercial PMMA tubing, cut to size using a saw. Six holes were drilled through the shell wall, three for the top plate and three for the base plate. Additionally, a rectangular recess was cut out on the upper portion of the shell to provide external access to the front face of the electronics stack, allowing the micro USB cable to be connected to the microcontroller without disassembling the gripper.

Figure 3.6 shows the final assembly procedure of the gripper, which consists of the following steps. First, the electronics stack was secured to the top plate by means of M3 screws. The fingers were then screwed onto the base plate. The two subassemblies were then interconnected through the necessary wiring. This includes the power circuit wiring connecting the electronics to the tendon series, and the I^2C wiring connecting the stack to the pressure sensor boards embedded in the fingers.

Finally, the PMMA outer shell was slid over the assembly and secured to both plates with screws, completing the gripper. To facilitate the correct positioning and sliding of the base plate inside the shell during this step, an auxiliary threaded hole was included at the center of the base plate. A long screw was temporarily secured in this hole and used as a handle to guide the plate into the correct position inside the shell. Once the shell was secured, the auxiliary screw was removed.

Figure 3.7 shows the final assembled gripper in both the two-finger and three-finger configurations.

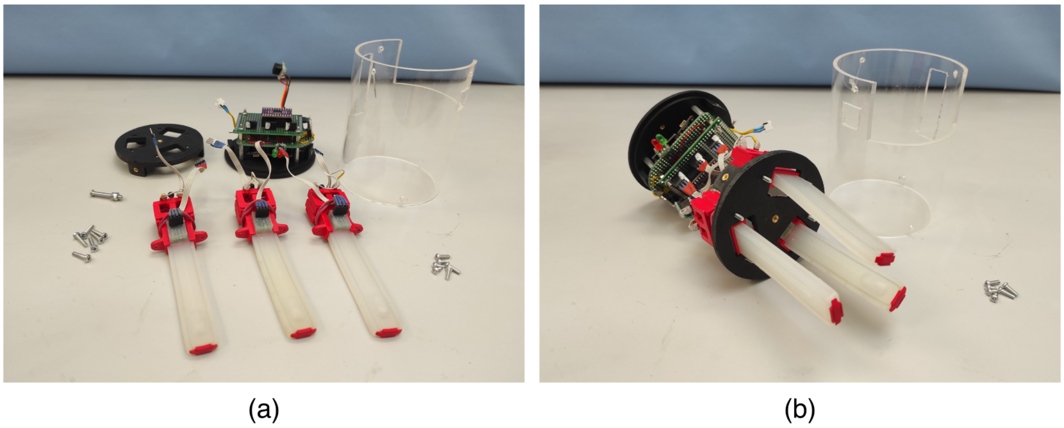
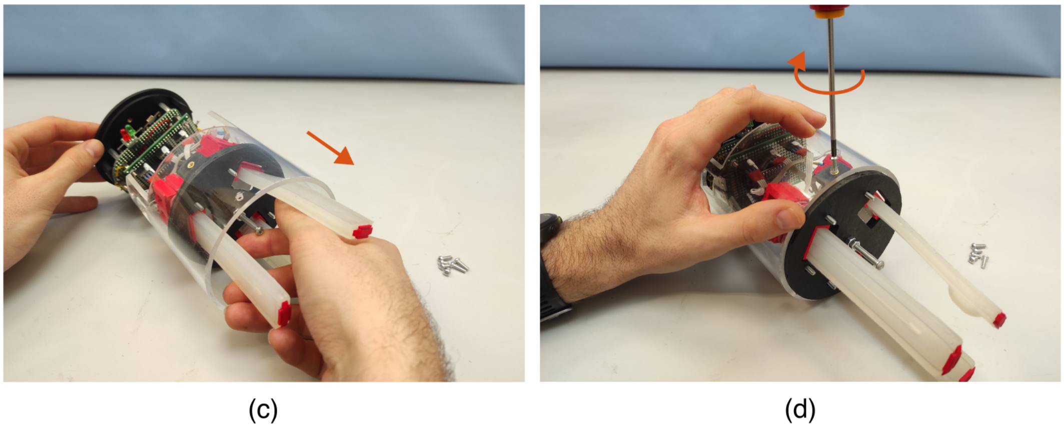

(a) (b) (c) (d)

Figure 3.6: Final assembly sequence of the gripper. **(a)** All produced parts, ready to be assembled together. **(b)** Wiring. **(c)** The outer shell is installed with the help of the auxiliary screw. **(d)** All the parts are secured in place with screws.

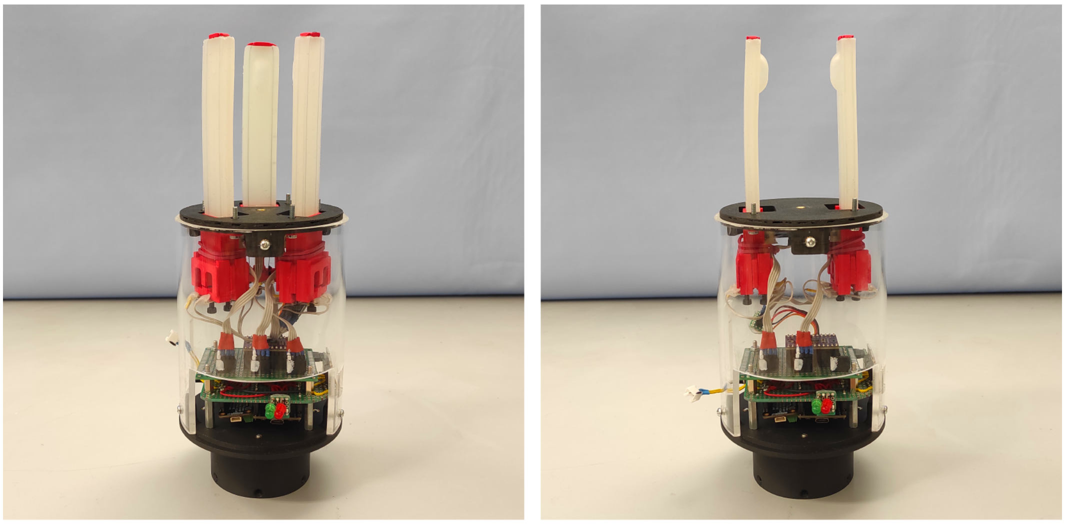

(a) (b)

Figure 3.7: Developed gripper. **(a)** Three-fingers configuration. **(b)** Two-fingers configuration.

Table 3.5: Dimensions of the assembled gripper, see Table 2.1 and Figure 2.1 for reference.

Dimension	**Value**
d_g	100 mm
d_f	60 mm
l_g	265 mm
l_f	96 mm

The reported total length l_g includes the end-effector flange, which was designed specifically for the robotic manipulator used during the testing phase and could be redesigned to adapt to other implementations. Furthermore, this dimension could be significantly reduced by replacing the electronics stack with a custom PCB and trimming the outer shell accordingly, eliminating the empty space currently present within the gripper body.

3.4 Firmware implementation

In order to control the actuation of the gripper and acquire data from the embedded sensors, an appropriate firmware was developed and flashed onto the ESP32 microcontroller.

The firmware was written in C language using the ESP-IDF framework (version 5.4), Espressif's official IoT Development Framework for ESP32 microcontrollers. The code was compiled and flashed onto the microcontroller through the ESP-IDF 5.4 CMD terminal, which was also used to monitor serial communication and exchange commands and sensor data with the remote control unit (PC).

In the following, the general architecture of the implemented code is described and the working principle of the main functions is briefly explained. The conceptual flowchart of the firmware, providing a graphical representation of the task architecture and main logic flows, is reported in Figure 3.8.

The firmware is organized around four concurrent tasks, managed by the FreeRTOS real-time operating system natively supported by the ESP32. Each task runs independently and is responsible for a specific function of the system. Upon startup, the `app_main()` initialization routine configures all peripherals: the GPIO outputs for the MOSFET switches and status LEDs, the UART interface for serial communication with the remote control unit, and the I^{2}C bus connecting the microcontroller to the current sensors and the pressure sensor multiplexer. The pressure sensors are initialized individually through the multiplexer, with their factory calibration coefficients read and verified from internal memory.

The `uart_local_mode_task` handles serial communication with the user. Commands are received via the UART interface from a remote control unit (PC) and dispatched accordingly. Available commands, entered directly from the keyboard, include starting and stopping actuation cycles, toggling sensor data streaming, and defining custom actuation sequences. Custom sequences are specified by the user as vectors of agonist state, antagonist state, and duration, allowing flexible open-loop control of the gripper.

The `gpio_control_task` manages the actuation timing. Based on the loaded cycle sequence, it drives the GPIO outputs connected to the MOSFET switches and status LEDs, advancing through the defined states at the prescribed durations. The task supports both finite and indefinite hold states, as well as repeated cycling.

The `sensor_monitor_task` handles sensor data acquisition and can be toggled on and off by the user. When active, it reads averaged current measurements from the two INA219 current sensors and acquires pressure and temperature data from the three MS5837 pressure sensors through the I^2C multiplexer, applying the manufacturer compensation formula to convert raw ADC values into physical units. Sensor data is streamed to the remote control unit via the serial interface at a rate of 10 Hz.

Finally, the `monitor_gpio_task` periodically prints the current GPIO state and operating mode to the serial console, providing a simple real-time status monitor for debugging purposes.

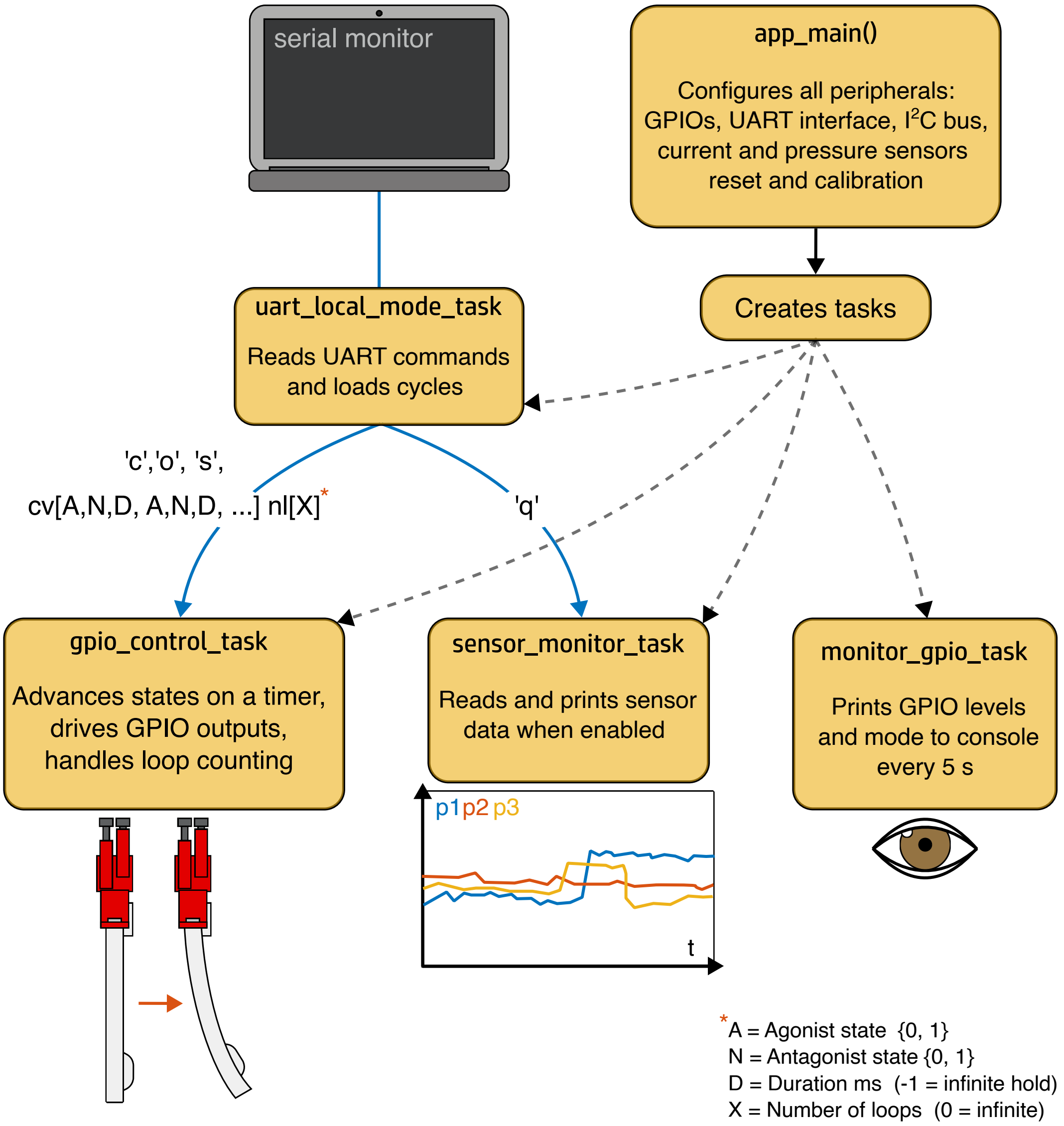

Figure 3.8: Conceptual flowchart of the implemented firmware.

Chapter 4

Characterization and testing

Different tests were performed to characterize the single finger actuator and the complete gripper. To evaluate the actuation performance of the finger, three tests were carried out:

- A step response test to evaluate the finger actuation dynamics
- A free-load deformation test to characterize finger bending for different actuation levels
- An isometric test to measure fingertip force for different levels of actuation and deformation

Finally, an end-to-end validation was performed by mounting the assembled gripper on a robotic manipulator and executing grasping tasks. During this phase, the tactile sensing system was evaluated as well.

4.1 Experimental Setup

In order to perform the three characterization tests listed above, a practical test bench was assembled. The experimental setup is shown in Figure 4.1, with its main elements labeled.

A T-slot aluminum extruded panel was used as a structural base. A dedicated support was 3D printed to secure the finger in a fixed position, allowing it to be screwed to the support through the holes present in its rigid base. The support was then fastened to the aluminum panel using bolts and T-slot inserts. This configuration allowed the finger to be easily repositioned on the panel by loosening the screws. The aluminum panel was maintained in a vertical position throughout the tests, so that the finger actuated along a vertical plane. This orientation was chosen to replicate the operating conditions of the gripper during real grasping tasks: in the three-finger configuration, the gripper approaches objects from above, meaning the fingers operate vertically during actual use.

To track the bending deformation of the finger, six colored markers were pinned to its exposed lateral face and a camera was placed on a tripod in front of the test bench, oriented perpendicularly to the actuation plane.

An external adjustable DC power supply, a Nice-Power SPS305D [33], featuring an integrated Constant Current mode, was used together with the developed electronics [1] to actuate the finger and monitor the current flowing through the tendon series via the integrated INA219 sensors. The electronics stack was connected to a PC for data exchange and command input via USB serial communication, as described in the prototyping chapter. During the isometric test, a strain gauge load cell was used to measure the force exerted at the fingertip for different levels of deformation. The load cell and its dedicated acquisition system are described in detail in Section 4.4. It was mounted on the aluminum panel by means of 3D printed rails, allowing precise positioning with respect to the fingertip.

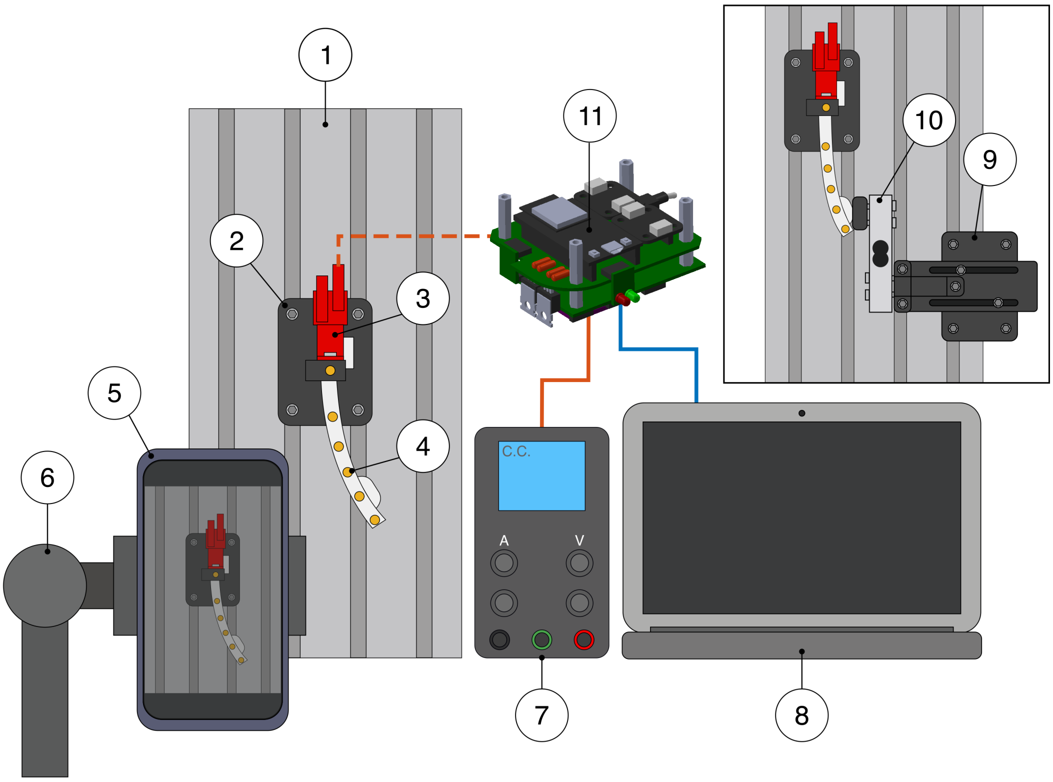

Figure 4.1: Experimental set up. **1**: Aluminum base panel. **2**: 3D-printed support. **3**: Developed finger. **4**: Marker. **5**: Camera. **6**: Tripod. **7**: DC Power Supply. **8**: Remote control unit (PC). **9**: 3D-printed rails. **10**: Load cell. **11**: Developed electronics.

---

[1] It should be noted that the characterization tests were conducted using a preliminary electronics setup, functionally equivalent to the final stack described in the prototyping chapter, which was completed prior to the pick and place validation phase.

4.2 Dynamic Tests

The objective of this test was to evaluate the step response of the finger actuator. A current step is applied to the finger and its deformation, in terms of fingertip deflection, is measured over time. This allows the actuation dynamics to be characterized and key parameters such as the settling time to be extracted, which are subsequently exploited in the static deformation tests. During each trial, a video was recorded using the camera mounted on the tripod and current data were simultaneously acquired by the INA219 current sensors. A custom firmware was developed for data acquisition: upon initialization, the current sensors were calibrated and configured in the 32V-1A range. Actuation could then be triggered via a serial monitor command, upon which current values and corresponding timestamps were streamed to a PC used as Remote Control Unit. Once the finger reached its deformed state, it was switched off and left to cool down completely before repeating the trial. The experiment was repeated three times, varying the amplitude of the current step. In this test, only the agonist tendon was actuated. The operational flowchart of the test is reported in Figure 4.2.

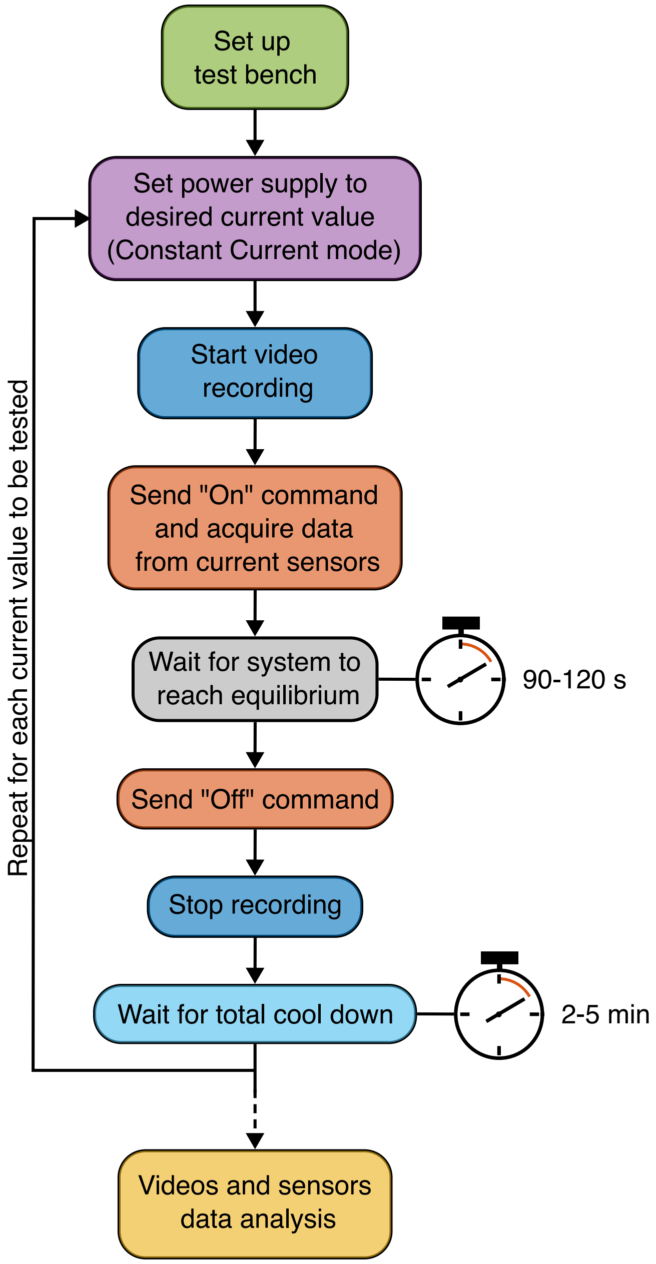

Figure 4.2: Operational flowchart of the dynamic test.

4.2.1 Data Analysis

Once video and current data were collected, the first step of the analysis consisted in extracting the fingertip position over time using the open source Tracker software.

The video was imported into the software and an initial frame was selected to define t_0, the reference instant from which tracking begins. The correct starting frame was identified by observing the status LEDs visible in the frame: the first frame in which the LED switches on corresponds to the moment of actuation, which can be unambiguously matched to the rise of the current signal in the acquired data, allowing precise synchronization between the two.

The scene was then calibrated using a calibration stick: a known reference object present in the frame was used to establish a pixel-to-meter conversion ratio, allowing the fingertip deflection to be expressed in physical units. A reference frame was subsequently defined by placing its origin on a marker attached to the 3D printed support, close to the finger base and symmetric with respect to the finger thickness. The x axis was set horizontal and the y axis vertical, parallel to the finger length.

The fingertip tracking pin was then identified manually in the first frame and tracking parameters related to the vision algorithm were set. Once configured, the auto-tracker function was activated, and the software reconstructed the position of the pin in each subsequent frame. The temporal axis was derived from the video frame rate, computed automatically by the software.

The resulting fingertip displacement data, together with the current data, were imported into MATLAB for synchronization, processing, and visualization. The fingertip displacement was synchronized with the current data using the LED-based reference instant identified during the Tracker analysis. Figure 4.3 summarizes the main steps of the Tracker software setup.

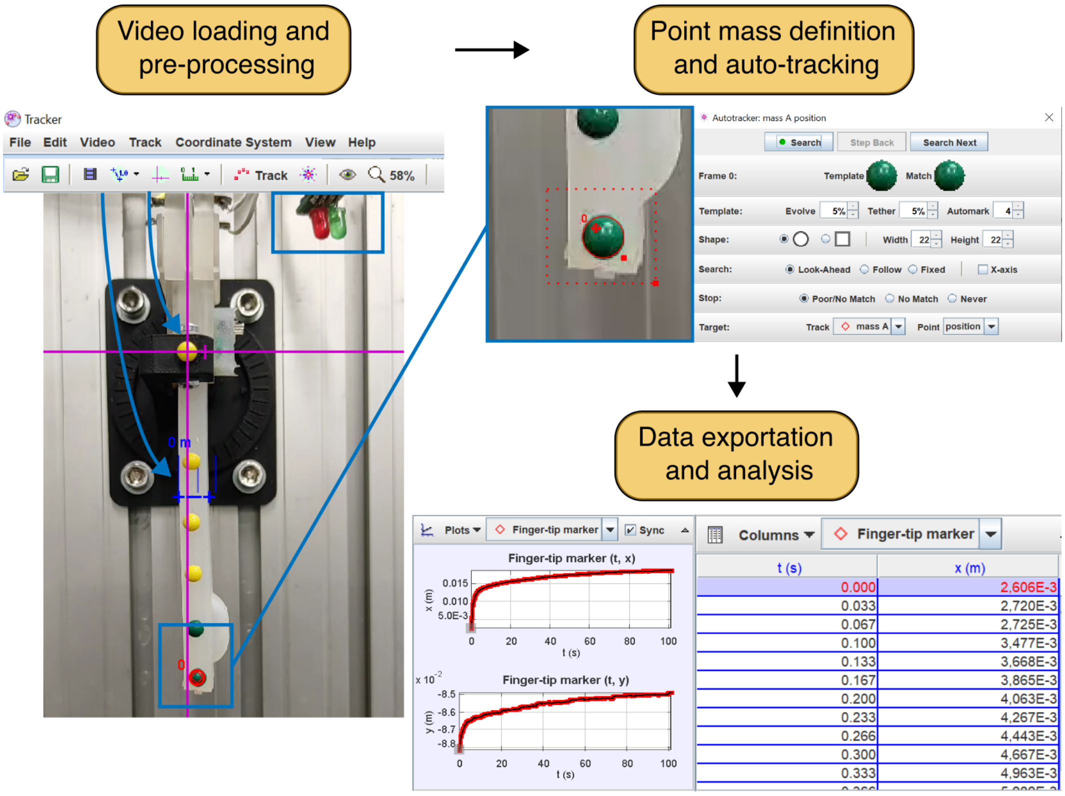

Autotracker: mass A position

Frame 0: Template Match

Template: Evolve 5% Tether 5% Automark 4

Shape: ● ○ ○ ☐ Width 22 Height 22

Search: ● Look-Ahead ○ Follow ○ Fixed ☐ X-axis

Stop: ● Poor/No Match ○ No Match ○ Never

Target: Track mass A Point position

t (s)	x (m)
0.000	2,606E-3
0.033	2,720E-3
0.067	2,725E-3
0.100	3,477E-3
0.133	3,668E-3
0.167	3,865E-3
0.200	4,063E-3
0.233	4,267E-3
0.266	4,443E-3
0.300	4,667E-3
0.333	4,963E-3

Figure 4.3: Main steps of the Tracker software setup.

4.2.2 Results

Figure 4.4 shows the step response of the finger actuator. The plot is divided into two sections: the lower section reports the current over time, while the upper section shows the corresponding fingertip deflection d over time.

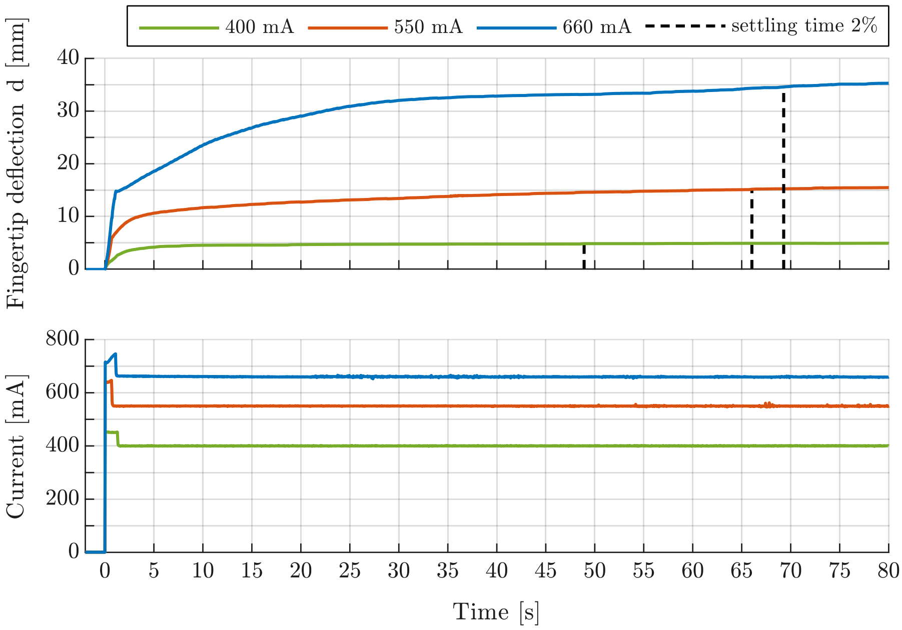

Figure 4.4: Step response of the finger actuator.

The test was repeated for three current step amplitudes: 400 mA, 550 mA, and 660 mA. The steady-state fingertip deflection values for the three steps are approximately 5 mm, 15 mm, and 36 mm respectively. The settling times, evaluated using a 2% error band around the steady-state value, range from 49 to 69 seconds, indicated by black dashed lines in the plot. The system was allowed to reach equilibrium by visual observation, resulting in a total wait time of approximately 90-120 seconds. The plot reports the first 80 seconds of the response. The deformation does not evolve linearly over time. In the initial phase, the finger bends rapidly, the slope of the deflection curve is steep, and then progressively slows down, exhibiting a behaviour similar to a logarithmic response. Approximately 90% of the total deformation occurs within the first 35 seconds in the case of the 660 mA step, and proportionally less for lower current values. This behaviour can be attributed to the mechanical properties of the silicone matrix, which acts as a spring opposing the tendon contraction. Initially, the elastic restoring force is small and the tendon contraction produces rapid bending. As deformation increases, the elastic force grows until equilibrium is reached between the tendon pulling force and the elastic restoring force of the silicone matrix. A further source of non-linearity is the SMA tendon pulling force itself, which is not constant for a given current value but depends on the martensite fraction, a function of both load and temperature. Based on these results, a settling time of 70 seconds was adopted as the standard wait time in the subsequent static tests, ensuring equilibrium was consistently reached. In the pick and place validation, actuation times were significantly shorter, as discussed in Section 4.5. Observing the current profile, it can be noted that the step provided by the DC power supply features an initial overshoot rather than an ideal step shape. This is a consequence of the operating principle of the constant current mode. The power supply is normally operating in constant voltage mode. When the current drawn by the circuit exceeds the set limit, which occurs because the supply voltage is intentionally set higher than the minimum required to drive the desired current through the tendon series resistance, the power supply automatically switches to constant current mode and saturates the output current to the set value. The transition between the two modes takes approximately 1 to 1.5 seconds, producing the characteristic overshoot visible at the beginning of the current profile. As a practical example, for a target current of 400 mA flowing through a tendon series resistance of approximately 30 Ω, the supply voltage is set above $400\text{ mA} \cdot 30\ \Omega = 12\text{ V}$, causing the circuit to initially draw excess current before the supply switches to constant current mode and stabilizes at the desired value. It should be noted that this initial current overshoot does not compromise the validity of the observed results, its magnitude is contained and its duration is negligible compared to the overall dynamics of the system.

The results allow some considerations to be made on the performance of the finger as an actuator. At the maximum tested current of 660 mA, the value adopted during the gripper validation, the finger achieves a fingertip deflection of 36 mm, which represents a significant range of motion relative to the 100 mm finger body length. Furthermore, since the antagonist tendon enables actuation in the opposite direction with a symmetric response, the total range of motion of a single finger is approximately 70 mm. Considering that a grasp involves at least two opposing fingers, the effective grasping range doubles further. Regarding the actuation dynamics, the settling times observed in this test, ranging from 49 to 69 seconds, are relatively long. However, two important considerations must be made. First, the step input used here is not representative of an optimized actuation strategy, but rather a controlled reference input chosen to characterize the system dynamics and extract metrics for the subsequent static tests. The actuation time can be considerably reduced with a more sophisticated control strategy. As reported in the Flexinol® datasheet, applying a large initial current to rapidly heat the wire followed by a reduced holding current to maintain the contracted state is a well established approach to improve actuation speed, and the wire contraction rate is in principle limited only by the rate of temperature change rather than by any fundamental mechanical constraint. Second, in practical grasping tasks the finger does not necessarily need to travel its full range of motion before making contact with an object. The effective actuation time depends on the relative dimensions of the gripper and the grasped object, and in most cases only a fraction of the total stroke is required, resulting in significantly shorter contact times in practice. The three repetitions performed for each current value showed consistent dynamic behaviour, confirming the repeatability of the results.

4.2.3 Repeated Actuation and Thermal Drift

With the same experimental setup, the test was reproduced using a square wave input instead of a single current step. This repeated actuation protocol was designed to study the finger relaxation dynamics and to observe potential thermal drift over time. The test was conducted at three different values of T_{on}, 1.2 s, 10 s, and 28 s, all at 50% duty cycle, and was repeated with and without activation of the antagonist tendon during the relaxation phase. The actuation current was fixed at 660 mA throughout.

Figure 4.5 shows the results for the case of $T_{on} = 10$ s, with and without antagonist activation. As in the previous plot, the upper section reports the fingertip deflection and the lower section the current profile, with the agonist and antagonist current channels clearly distinguished. The first four actuation cycles are shown.

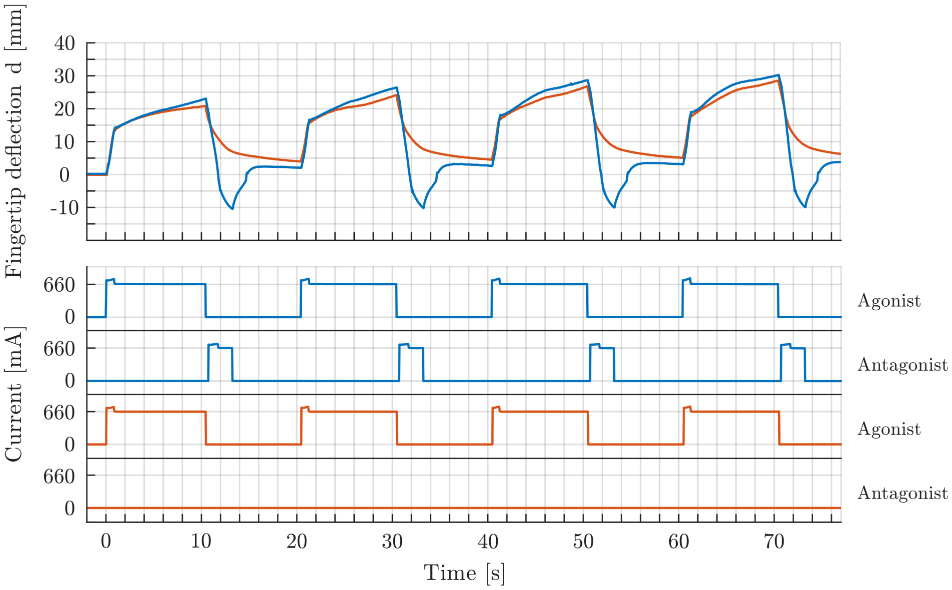

Figure 4.5: Square wave response of the finger actuator at $T_on = 10$ s and I = 660 mA, with and without antagonist tendon activation during the recovery phase. Upper section: fingertip deflection over time. Lower section: current profiles of agonist and antagonist tendon series.

During the T_{on} phase, the fingertip deflection closely follows the behaviour observed in the step response test for the 660 mA step, reaching 20 to 25 mm of deflection within 10 seconds, consistent with the previously characterized dynamics.

The T_{off} phase reveals the most significant differences between the two cases. When the antagonist tendon is not activated, the return to the neutral position is a passive process driven solely by the elastic restoring force of the silicone matrix, which progressively prevails as the agonist tendon cools down. The recovery profile is non-linear, with most of the return occurring in the initial part of the off phase and then slowing down. With a T_{off} of 10 seconds, the finger fails to fully recover the neutral position. This is attributed to incomplete cooling of the agonist tendon within the available time and to friction between the tendon and the tendon sheath, which, although contained, can overcome the elastic restoring force of the silicone body at small deformation levels.

When the antagonist tendon is activated for 2.5 seconds following the switch-off of the agonist, the recovery is instead active and significantly faster. The finger fully returns to the neutral position and exhibits a slight undershoot, a brief actuation in the outward direction, before settling. When the antagonist tendon is subsequently switched off, a residual positive deflection reappears, caused by heat accumulated in the agonist tendon during the preceding T_{on} phase that has not yet fully dissipated.

This plot further demonstrates an important benefit of the agonist-antagonist tendon architecture: beyond enabling bidirectional actuation, it provides active recovery of the neutral position. This capability is particularly valuable in grasping applications, where fast and reliable finger opening is required to release objects. In the pick and place validation, the antagonist tendon was systematically activated to open the gripper and release the grasped object, as discussed in Section 4.5. It is worth noting that the actuation patterns used throughout this analysis consist of simple open-loop square wave current profiles. With a dedicated closed-loop control strategy, significantly more precise and efficient position control could be achieved, further reducing actuation and recovery times.

Upon repeated actuation cycles, heat generated in the SMA tendons by the Joule effect can accumulate within the silicone matrix, which acts as a thermal insulator and slows heat dissipation. This progressive heat buildup produces a gradual drift in the finger behavior over time, observable in both the baseline and peak deflection of the finger. Figure 4.6 reports a comparison between the first two and the last two actuation cycles of a three-minute repeated actuation test, with the intermediate portion of the time axis interrupted for clarity. Both the case with antagonist activation during neutral position recovery (blue line) and without it (orange line) are shown. Two drifting phenomena are simultaneously observable, they will be referred to as upper thermal drift (UTD) and lower thermal drift (LTD) respectively. First, the baseline of the deflection curve, corresponding to the neutral position recovered during the off phase, drifts upward progressively: the finger is unable to fully return to its original neutral position between cycles, as the residual heat in the agonist tendon prevents complete cooling and therefore complete relaxation. Second, the peak deflection also increases over time: since the tendon begins each cycle at a higher temperature, a greater fraction of the wire has already undergone the martensitic transformation before actuation, resulting in a slightly larger contraction and therefore a higher fingertip deflection at steady-state. Both effects are consistent with the thermomechanical behavior of SMA wires described in the Flexinol® datasheet: the contraction and relaxation of the wire are governed solely by its temperature, and any residual heat accumulated between cycles directly influences the subsequent actuation. The antagonist tendon activation during the recovery phase is effective in recovering the neutral position. When the antagonist tendon is powered, the finger actively returns to the neutral position and exhibits a slight undershoot. However, once the antagonist tendon is switched off, the finger regains a slightly positive deflection due to the residual heat still present in the agonist tendon. This residual positive deflection follows the same upward drift observed in the passive recovery case: the antagonist tendon can actively counteract the elastic and frictional forces preventing neutral recovery, but cannot remove the accumulated thermal energy from the agonist tendon. As a result, the thermal drift of the baseline is present in both cases, though the antagonist activation ensures a more consistent recovery at each cycle. This behavior has practical implications for the gripper operation. In continuous use, the thermal drift causes the finger to gradually adopt a more deflected resting position and to actuate slightly further with each cycle. While this effect was limited over the timescale of the pick and place tests performed in this work, it would become relevant in applications requiring prolonged or high-frequency cycling. Mitigation strategies include the use of active cooling, longer rest periods between cycles, or a closed-loop control strategy that compensates for the drift by adjusting the actuation current accordingly.

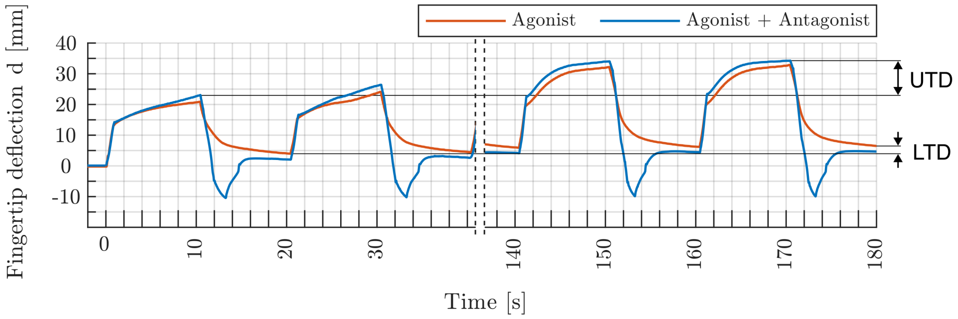

Figure 4.6: Thermal drift observed during repeated actuation cycles. The first two and last two cycles of a three-minute test are shown, with the intermediate portion omitted for clarity (dashed vertical line). Two cases are reported: agonist-only actuation (orange) and agonist actuation with antagonist activation during the recovery phase (blue). UTD: upper thermal drift, indicating the upward shift of the peak deflection over time. LTD: lower thermal drift, indicating the upward shift of the baseline deflection over time. T_{on}=10 s, I = 660 mA.

4.3 Free-Load Deformation Test

The objective of this test was to evaluate the steady-state deformation of the finger and observe its deformed shape under free-load conditions for different actuation levels. A current step was applied to the finger, which was left to deform freely with no external loads until steady-state was reached. Unlike the dynamic test, no video acquisition was required: a single photograph was taken after 70 s, a duration confirmed to be sufficient for reaching steady-state by the previous step response test. The tendons were then switched off and allowed to cool down completely before the next trial. The test was repeated for 10 different current values, and the entire procedure was conducted three times to assess repeatability. A custom firmware was developed for this test. Current values were monitored in real time via the serial monitor: an average over 10 samples was printed together with a timestamp every second, allowing to track the elapsed time and capture the photo at the correct instant. The operational flowchart of the test is reported in Figure 4.7.

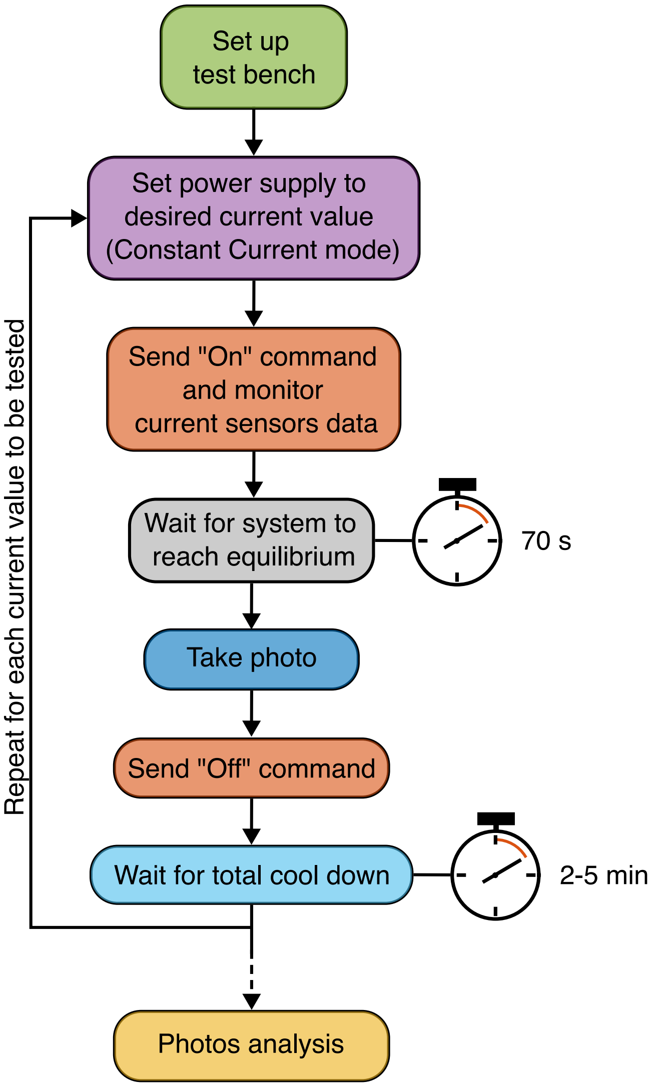

Figure 4.7: Operational flowchart of the free-load deformation test.

4.3.1 Data analysis

In this test, all six markers were taken into consideration to reconstruct the full bending shape of the finger. Manually identifying each marker in every photograph would have been a tedious and error-prone process. For this reason, a dedicated marker detection function was developed in MATLAB, exploiting the Image Processing Toolbox. The function takes an image as input and automatically detects and localizes the markers attached to the finger. The main steps of the algorithm are summarized in Figure 4.8. The image is first read, resized, and rotated. The resizing step is particularly important for high resolution images, as it reduces the computational cost of subsequent operations by sub-sampling the scene while preserving its content. The color space is then converted from RGB to HSV, which uniquely describes colors in terms of Hue, Saturation, and

Value, separating chromatic information from luminance. The Hue channel was selected for further processing, as the colored markers appear clearly distinguishable from the background in this representation. A binarization step is then applied: pixels with a Hue value above a defined threshold are set to 1 and all others to 0, producing a binary mask. An additional spatial mask discards pixels in the peripheral regions of the image, since the finger and markers are known to be located in the central portion of the frame. The resulting binary image still contains outliers, which are removed using connected component analysis. This groups connected pixels of equal value into distinct regions and computes their geometric properties. Markers are identified by applying filters on circularity, eccentricity, and area, properties that are consistent across images since the markers are rounded pins and the camera is maintained at a fixed distance from the scene. The detected regions are sorted by centroid position and their coordinates are returned as the output of the function. A dedicated script then loops over all photographs, applies the detection function, and produces the final plots.

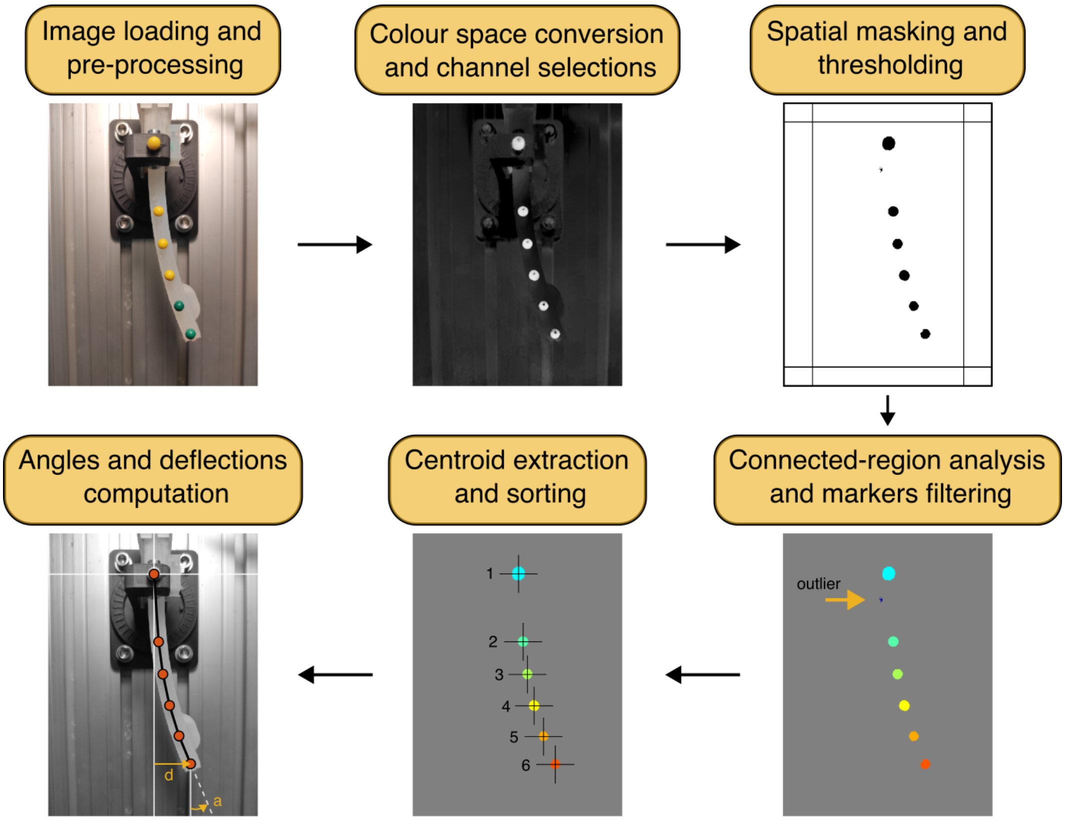

Figure 4.8: Main steps of the marker detection algorithm implemented in MATLAB.

4.3.2 Results

Figure 4.9 (a) reports the steady-state fingertip deflection d as a function of applied current, while Figures 4.9 (b)-(e) show photographs of the actuated finger at selected current values with the reconstructed deformed shape overlaid.

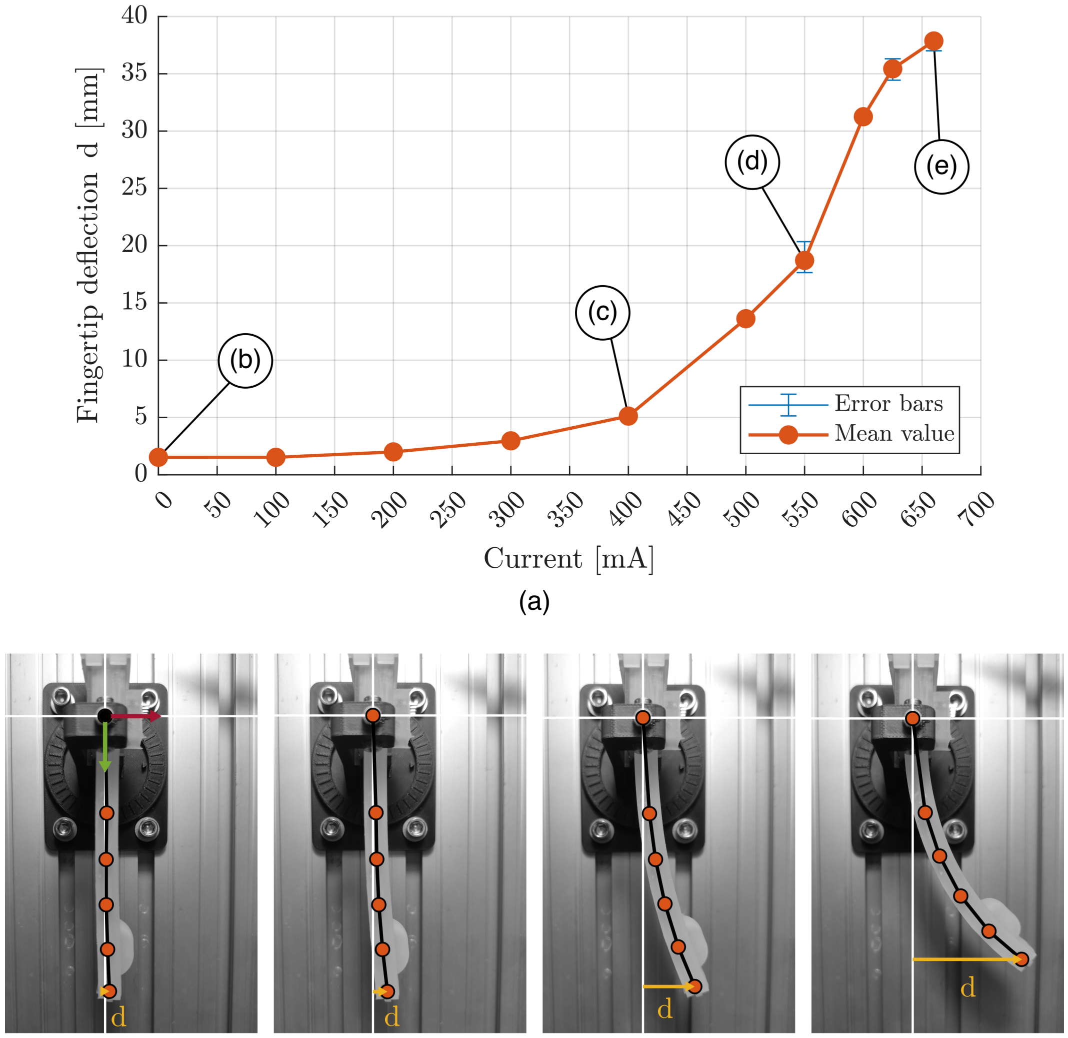

(a)

(b) (c) (d) (e)

Figure 4.9: Free-load deformation test results. **(a)** steady-state fingertip deflection as a function of applied current. Error bars represent variability across three repetitions. **(b)-(e)** Photographs of the finger at selected current values with the reconstructed deformed shape overlaid.

For current values below 300 mA, no significant fingertip deflection is observed. A residual 1-2 mm deflection is present even at 0 mA, which is attributed to friction between the tendon and the tendon sheaths rather than to any actual actuation. Between 300 mA and 400 mA, a first observable deformation occurs, reaching approximately 5 mm at 400 mA. Above 400 mA the slope of the deflection curve increases markedly: a deflection of approximately 15 mm is observed at 500 mA, and the slope increases further between 550 mA and 625 mA, reaching approximately 35 mm at 625 mA. Above this value the curve begins to saturate, reaching approximately 37-37.5 mm at 660 mA. The results are consistent with those observed in the step response test, with slightly higher deflection values recorded here, which is expected given the longer settling time allowed.

The shape of the deflection curve is directly linked to the thermomechanical behavior of the SMA tendons. Current values below 300-400 mA are insufficient to raise the wire temperature to the austenite start temperature of 70°C, and the wire remains in the martensitic phase, producing no meaningful contraction. As the current increases beyond this threshold, the phase transformation begins and the tendon contraction force grows rapidly, producing the steep increase in deflection observed between 400 mA and 600 mA. The saturation observed above 625 mA is consistent with the approach to the maximum recoverable strain of the wire, which the Flexinol® datasheet reports to be in the range of 4-5% for reliable cyclic operation. Beyond this point, further increases in current raise the wire temperature but produce no additional contraction, as the transformation is essentially complete.

Furthermore, as visible in Figures 4.9 (b)-(e), the deformed shape of the finger closely approximates a circular arc, consistent with the constant curvature bending behaviour predicted by the quasi-static model reported in Appendix A and attributable to the uniform cross-section of the silicone matrix and the concentrated bending moment generated by the tendon-driven mechanism.

It is also worth noting that the steady-state deflection represents the mechanical equilibrium between the tendon contraction force and the elastic restoring force of the silicone matrix. As reported in the datasheet, the magnitude of the contraction force depends on the stress level imposed on the wire during cooling, in this case provided by the pretensioned silicone body acting as a bias force. The observed deflection profile is therefore the result of the combined nonlinear behavior of both the SMA wire and the silicone matrix.

The error bars visible in Figure 4.9 (a) indicate the variability across the three repetitions. The repeatability is generally good, with the exception of the 550 mA data point, which shows a slightly larger spread. This is consistent with the steep slope of the curve in this current range, which translates into large variations in deflection for small variations in wire temperature.

Fingertip deflection was selected as the primary deformation metric throughout all characterization tests, rather than fingertip angle, for two reasons. First, it provides a consistent and directly comparable parameter across all three tests. Second, it has a direct functional interpretation in the context of grasping. The transverse displacement, i.e. fingertip deflection, the finger must cover to make contact with a grasped object, assuming a symmetric grasp with the object centered among the fingers, is:

$$d = \frac{d_f - d_o}{2}$$

where d is the required stroke, d_f is the distance between finger bases, and d_o is the diameter of the grasped object. The fingertip deflection thus directly relates to the grasping range of the gripper and to the d_o/d_f ratio reported in Table 4.2.

4.4 Isometric test

The objective of this test was to measure the fingertip force for different values of applied current and at different imposed deformation levels. A current step was applied to the finger, whose deformation was constrained by the presence of a load cell. The load cell was equipped with a 3D printed flat indenter and held in a vertical orientation, parallel to the finger in its neutral position. It was mounted on the base panel of the test bench using 3D printed rails to allow for adjustment along two axes. The axis perpendicular to the finger face sets the imposed deflection level, while the axis along the finger length centers the contact point between the indenter and the fingertip, keeping it consistent across all trials. After waiting 70 s, as in the free-load test, the force was acquired. The finger was then switched off and allowed to cool down completely before the next trial. The test was repeated for seven different load cell positions, corresponding to seven imposed deformation levels, and for each position six current values were tested. The entire procedure was conducted three times to assess repeatability. To measure the actual deformation at each load cell position, the finger was equipped with marker pins and one photograph per position was taken and processed using the same marker detection algorithm described in the free-load test section.

4.4.1 Load Cell and Data Acquisition

The load cell used is a strain gauge type. It consists of a small aluminum beam with a cutout at the center that locally reduces its bending stiffness. Two strain gauges are bonded on opposite faces of the beam. When an external force produces a bending moment, the two gauges deform in opposite directions, generating a differential voltage proportional to the applied force. This signal is read and converted to a force value through a known linear relationship. The load cell was used together with an HX711 24-bit ADC, wired to unused GPIO pins of the ESP32 via a four-wire interface, power, ground, serial clock, and serial data, analogous in structure to I^2C. The full scale of the load cell is 1 kg. Preliminary tests showed that the forces exerted by the finger were well within the 0-100 g range. A dedicated calibration procedure was therefore carried out before the isometric test to improve measurement accuracy within this range: known reference weights in the 0-100 g range were applied to the cell and the corresponding 24-bit ADC readings were recorded. A linear gain was then computed from these data using a least squares regression, and this gain was used in the firmware to convert raw ADC readings to force values. A tare procedure was performed before every trial to zero the scale.

The operational flowchart of the test is reported in Figure 4.10.

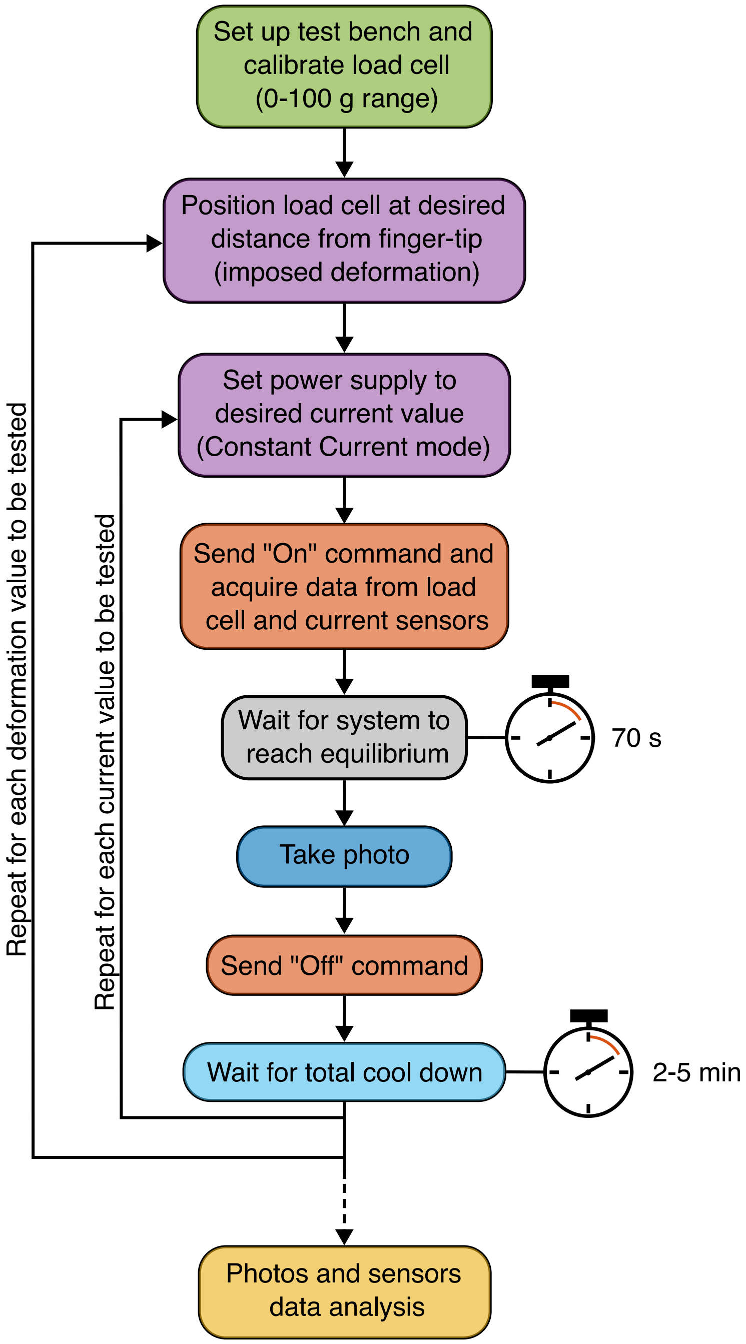

Figure 4.10: Operational flowchart of the isometric test. The outer loop iterates over deformation levels, while the inner loop iterates over current values tested at each deformation.

4.4.2 Results

Figure 4.11 (a) reports the fingertip force as a function of fingertip deflection for six current values. Figure 4.11 (b) shows a photograph of the actuated finger in contact with the load cell indenter during force acquisition.

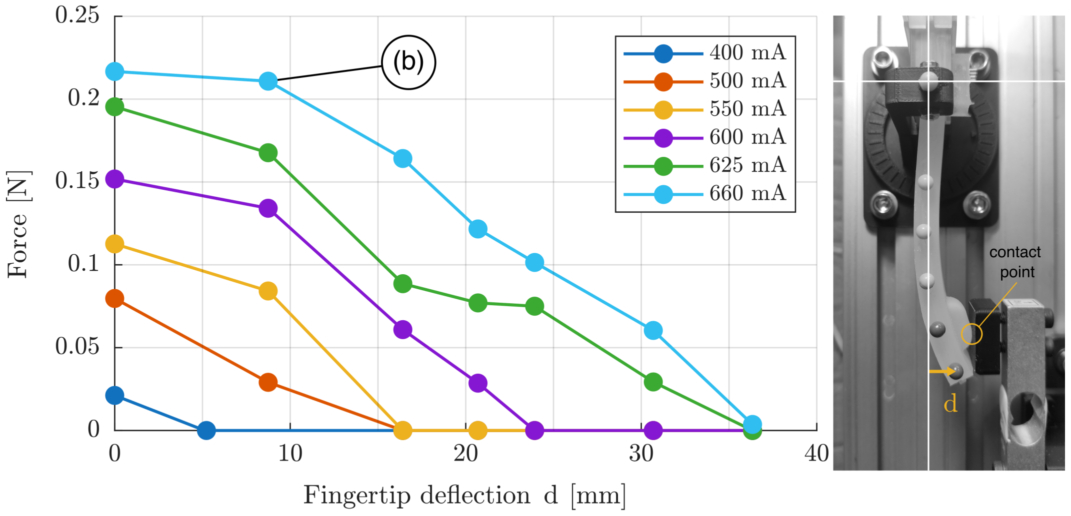

(a) (b)

Figure 4.11: Isometric test results. **(a)** Fingertip force as a function of fingertip deflection for six current values. **(b)** Photograph of the actuated finger in contact with the load cell indenter during force acquisition.

The maximum measured fingertip force was 0.22 N, recorded at 660 mA and at zero imposed deformation, that is, with the load cell positioned directly in front of the fingertip in its undeflected rest position. This is consistent with expectations: at zero deformation the elastic restoring force of the silicone body is negligible, and the entire tendon contraction force is available at the fingertip. Observing the force values at zero deformation across current levels, the same trend identified in the free-load test is recognizable: negligible force below 400 mA, a rapid increase between 400 mA and 625 mA, and a saturation between 625 mA and 660 mA. This is consistent with the SMA phase transformation occurring progressively in this current range and being essentially complete above 625 mA, as discussed in the previous sections.

As the imposed deformation increases, the measured force decreases for all current levels, following an approximately linear trend. This linearity reflects the approximately linear elastic behavior of the silicone matrix in the tested deformation range. The decrease can be explained by considering that the force measured by the load cell represents the net force at the fingertip, the difference between the tendon contraction force and the elastic restoring force of the silicone body. As the finger is forced into a more deformed configuration, the elastic restoring force grows, reducing the net force available at the fingertip. Each curve reaches zero at the deformation level at which the two forces are in equilibrium, which corresponds to the steady-state free-load deflection at the same current. This is largely consistent with the results of the free-load test, providing a cross-validation between the two experiments. A slight discrepancy is observed for the 500 mA and 550 mA curves, whose zero-force crossings occur at slightly smaller deformation levels than the corresponding free-load steady-state values. This is likely attributable to the additional mechanical constraint introduced by the load cell, which modifies the deformation path of the finger compared to the unconstrained case.

The area under each force-deflection curve represents the mechanical work produced by the finger at the corresponding current level, providing a measure of the energy output of the actuator.

The maximum measured force of 0.22 N is modest in absolute terms. However, fingertip force is not the only contributor to grasping capability in soft grippers. Friction between the compliant silicone finger surface and the grasped object, combined with the ability of the finger to conform and wrap around irregular shapes, can provide a secure grasp even at low normal forces. This is a well recognized advantage of soft grippers over rigid ones, and its practical implications are demonstrated in the pick and place validation presented in Section 4.5. Data points where the finger did not reach the load cell were recorded as zero force. Error bars are not shown in the plot, as the three repetitions showed good consistency across all measured data points.

The main results obtained from the three characterization tests are summarized in Table 4.1, providing an overview of the finger actuator performance at the reference actuation current of 660 mA.

Table 4.1: Summary of single finger characterisation at 660 mA actuation current.

Test	**Parameter**	**Value**
Step response	Settling time	70 s
	Fingertip deflection	18 mm @ 5 s 32 mm @ 30 s 36 mm @ 70 s
Free-load	Max deflection	36 mm (after settling time)
	Bending shape	Arc of circumference (constant curvature)
Isometric	Max tip force	0.22 N (null deformation)
Additional observations	Thermal drift upon repeated actuation	
	Active recovery of neutral position by antagonist tendon	

It should be noted that a finger manufactured using a stiffer silicone, Shore A40 compared to the Shore A25 used for the other finger, was also tested. Although a slightly higher maximum fingertip force of approximately 0.3 N was measured, the increased rigidity of the material proved disadvantageous to both the wrapping performance during grasping and the sensitivity of the tactile sensing system, as the stiffer bladder walls required larger contact forces to produce a measurable pressure variation. Furthermore, the higher viscosity of the Shore A40 formulation introduced significant practical difficulties during the manufacturing process, particularly in the degassing and casting steps, making it harder to achieve void-free parts. For these reasons, the Shore A25 formulation was selected as the material of choice for all finger prototypes.

4.5 Gripper Validation

The aim of this last testing phase was to evaluate the grasping capability of the developed gripper prototype, both in the two-finger and three-finger configurations. The prototype was mounted on a Kinova Gen2 7-DOF commercial robotic arm, replacing its original rigid gripper, and tested in pick and place tasks involving objects of different shapes, dimensions, and masses. The gripper was attached to the robot arm by means of the custom 3D printed flange described in the functional design chapter and secured with six screws. Figure 4.12 shows the developed soft gripper mounted on the Kinova Gen2 robotic arm (a) and the original rigid gripper alongside the developed gripper (b).

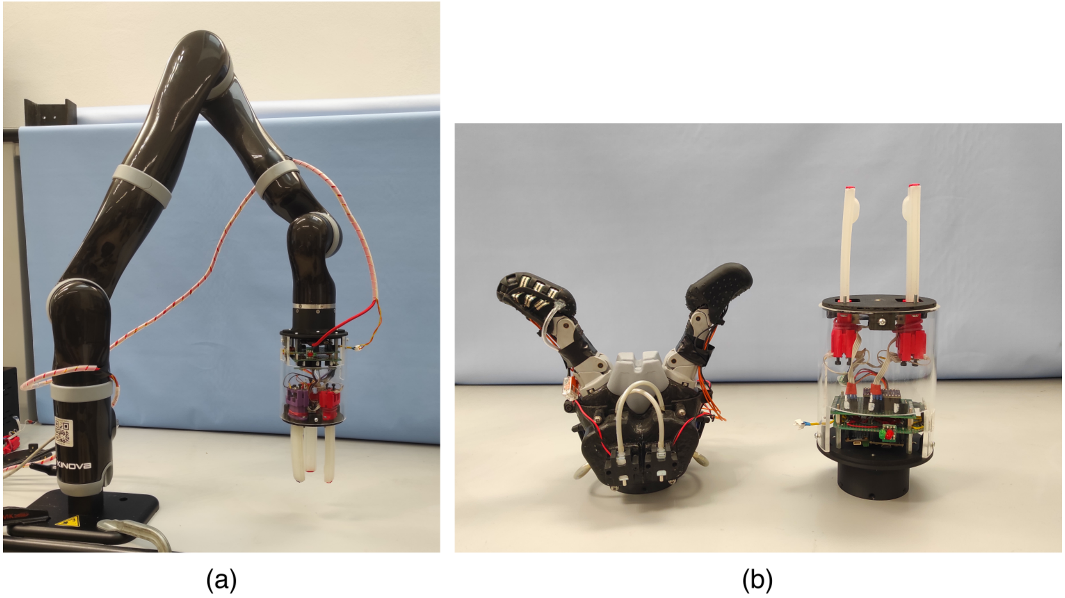
(a) (b)

Figure 4.12: **(a)** The developed soft gripper mounted on the Kinova Gen2 robotic arm. **(b)** The original rigid gripper alongside the developed gripper.

To execute the pick and place task, the robot arm was pre-programmed to follow a fixed trajectory autonomously, while the gripper was actuated manually through keyboard serial commands. The task consisted of picking an object from a fixed point A, lifting it, transporting it to a fixed point B, and releasing it. The sequence of steps is summarized in Figure 4.13:

1. The robot arm moves to position the gripper above the object.
2. The `open` command is sent: the antagonist tendons are activated and the fingers bend outward.
3. After a 5-second delay, the robot arm lowers the gripper onto the object at a pre-programmed height.
4. The `close` command is sent: the agonist tendons are activated and the fingers close around the object.
5. After a 15-second delay, the robot arm lifts the gripper with the grasped object, moves above point B, and lowers down.
6. The `open` command is sent again and the object is released.

7. The robot arm lifts the gripper and the `relax` command is sent, returning the fingers to their neutral position.

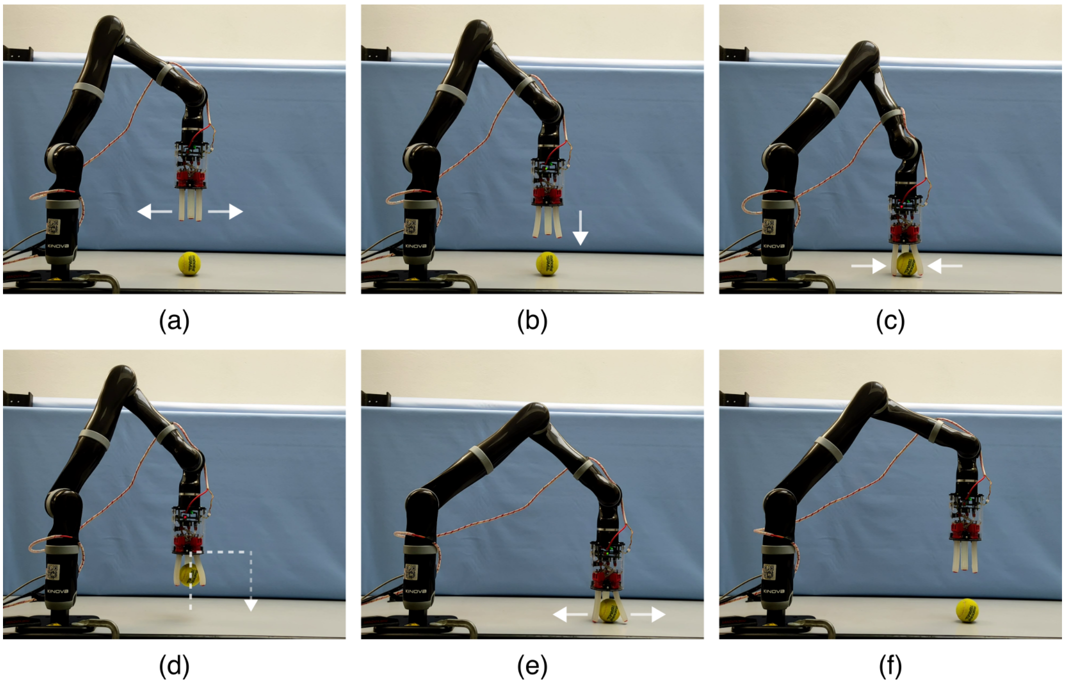
(a) (b) (c) (d) (e) (f)

Figure 4.13: Sequence of operations of the pick and place task.

The 5-second opening delay was sufficient to open the gripper before contact with the object. Additionally, the gripper continues to open further as the robot arm lowers onto the object. The 15-second closing delay was chosen as a compromise between task speed and deformation achieved. Referring to the step response plot in Figure 4.4, at 660 mA, the actuation current used throughout the entire validation, the fingertip deflection reaches approximately 27 mm after 15 seconds, corresponding to 75% of the total available stroke. Point A and point B were kept fixed for all tested objects, while the waypoint height above each object was pre-programmed individually to account for the different object dimensions. No computer vision system was used.

The robot arm trajectory was defined by identifying a set of waypoints referring to the tool center point (TCP), the reference point at the center of the robot's end-effector flange. The gripper dimensions were accounted for during waypoint selection to avoid collisions with the environment. The robot arm was connected to the PC via Ethernet and programmed using the Kinova Development Center software. The reference frame was set to the fixed base frame of the robot, and the control mode was set to Cartesian, allowing waypoints to be specified in terms of position (x, y, z) and orientation $(\theta_x, \theta_y, \theta_z)$, which is more intuitive than direct joint angle control. Waypoints were defined by manually moving the arm to the desired pose using the virtual joystick in the software interface, or alternatively the physical joystick mounted at the base of the robot, and saving the current position. Time delays were inserted at specific waypoints to allow the gripper sufficient time to open or close before the arm continued its trajectory.

4.5.1 Grasping Types

Figure 4.14 illustrates the grasping strategies observed during the validation tests.

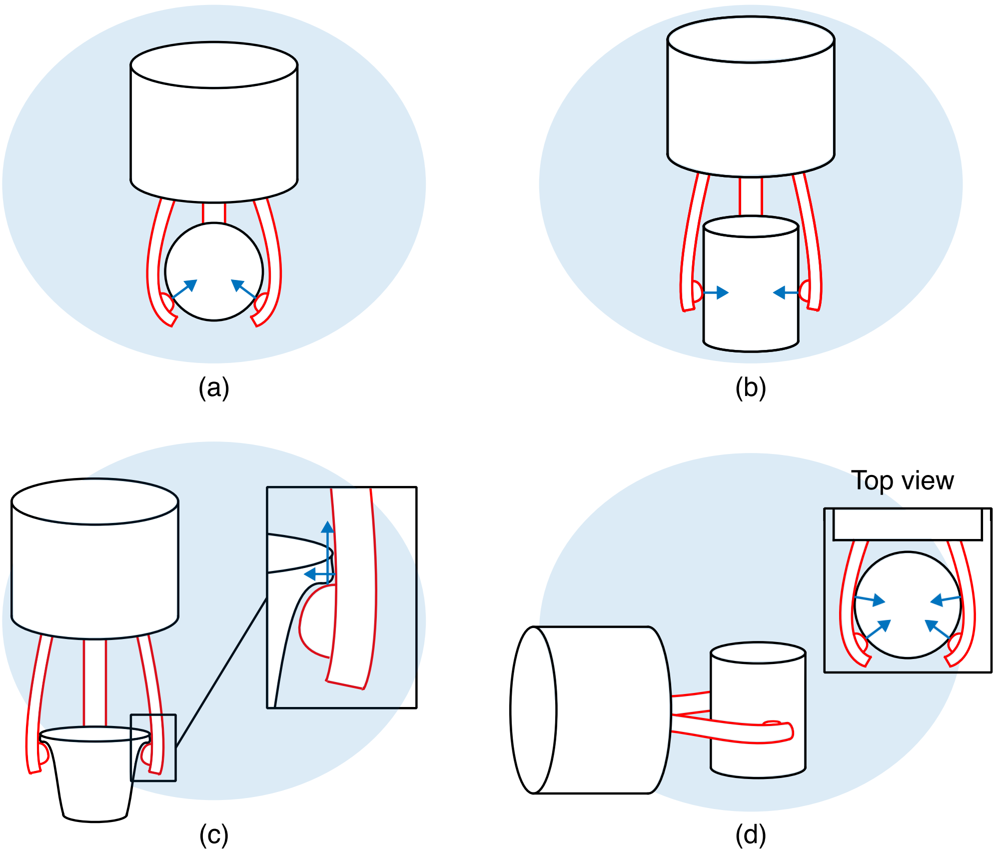

Figure 4.14: Grasping strategies observed during the pick and place validation. **(a)** Power grasp: the three fingers envelope a spherical object from above, with contact forces directed inward and upward. **(b)** Three-finger pinch grasp: the fingers contact the object laterally, with predominantly horizontal contact forces. **(c)** Form-fit grasp: the protruding bladder engages a geometric feature of the object, the lifting force is supported by the finger body in traction. **(d)** Parallel grasp (two-finger configuration): the gripper approaches laterally and contacts the object along its length.

In the three-finger configuration, three distinct grasping types were identified. The first is a **power grasp** [24], in which the three fingers envelope a roughly spherical object from above, wrapping around it and gently pushing it toward the palm. The contact force has a significant vertical component, and the grasp relies primarily on friction between the silicone finger surface and the object. The second type is a **three-finger pinch grasp**, in which the geometry of the object prevents the fingers from fully wrapping underneath it. The fingers instead pinch the object laterally, with the contact force oriented predominantly in the horizontal direction. Two variants of this grasp were observed: one in which only the fingertips are in contact, and one in which contact extends over approximately half the finger length, producing partial wrapping. A soda can grasped from above is a representative example of this case. Both the power grasp and the three-finger pinch grasp rely on friction to support the object weight during lifting. The third grasping type exploits the protruding bladders of the tactile sensing system to establish a **form-fit coupling** with a geometric feature of the grasped object, such as the rim of a glass or a structural rib. In this case, the finger bending force is responsible for engaging the coupling, while the lifting force is generated within the form-fit contact and supported by the finger body in tension. This strategy allows heavier objects to be lifted but is limited to objects with suitable geometric features. In the two-finger configuration, a **parallel grasp** was tested, in which the gripper approached the object laterally and grasped it along its longer dimension. The contact force is predominantly horizontal and perpendicular to the object axis, with lifting relying on friction. In the presence of suitable geometric features, a form-fit coupling can also be exploited in this configuration, this time using the lateral faces of the fingers as mechanical constraints rather than the protruding bladders. A more versatile variant, mounting two fingers on one side and one on the other to function as a thumb, was identified as a promising configuration but was not tested in this work, as it would have required a dedicated base plate and exceeded the scope of the current prototype. A total of 18 objects featuring different shapes, overall dimensions, and masses were tested. In Table 4.2 the successfully grasped objects, their main properties and the corresponding grasping strategies adopted are summarized.

Table 4.2: Objects successfully grasped during the pick and place validation test. d_o: object diameter, d_f: finger base spacing (60 mm), d_o/d_f: ratio between object size and finger spacing. Grasping type letters refer to the strategies illustrated in Figure 4.14.

Object	**Shape**	d_o **[mm]**	d_o/d_f	**Mass [g]**	**Grasping type***
Filled plastic glass	Cylinder	80	1.4	160	c
Pencil case		60	1.1	150	d
Coffee tin box		85	1.5	85	b, d
Filled paper glass		50	0.9	85	b, d
Oil bottle		40	0.7	40	b
Plastic bottle		80	1.4	30	d
Adhesive tape		60	1.1	30	b
Foam gear		70	1.3	30	b
Tin wire		55	1.0	25	b
Empty plastic glass		80	1.4	10	b, c
Tennis ball	Sphere	60	1.1	60	a
Egg		40	0.7	60	a
Lemon		45	0.8	75	a
Skein		70	1.3	70	a/b

*Letters refer to the grasping strategies illustrated in Figure 4.14.

As reported in Table 4.2, the heaviest successfully grasped object was a plastic glass filled with laboratory components, weighing 160 g. This was achieved by exploiting the form-fit coupling between the protruding bladders and the rim of the glass. The heaviest objects grasped with a power grasp and a three-finger pinch grasp were respectively a lemon weighing 75 g and a coffee tin box and a filled paper glass, both weighing 85 g. In the two-finger configuration, the coffee tin box (85 g) was successfully grasped with a standard parallel grasp, while a pencil case of 150 g was lifted by exploiting a form-fit coupling between the finger sides and the object geometry.

The three-finger configuration was tested more extensively than the two-finger one, as it represents the primary intended use of the gripper.

A power grasp was only achievable with objects whose shape could be approximated as a sphere. For the egg and the lemon, whose dimensions are relatively small, thin spacers were used to lift them slightly off the table surface, allowing the fingers to wrap around them. Without the spacers, the gripper could only achieve a weak pinch grasp, insufficient to retain the object during lifting. The boundary between power grasp and pinch grasp is not always sharp: upon partial slipping, a power grasp can transition into a pinch grasp, depending on the object geometry. This was the case for the skein, which was assigned both classifications.

Observing the d_o/d_f column, it can be noted that the gripper successfully manipulated objects ranging from approximately 0.5 to 1.4 times its characteristic finger spacing dimension. Below this lower bound, the fingers exerted insufficient force to generate enough friction to lift the object. A glue stick of 25 mm diameter and 38 g mass was tested without success. Above the upper bound, the gripper could not open wide enough or wrap sufficiently around the object to achieve a stable grasp. More relevant than the specific threshold values is the observation that the gripper was capable of grasping objects both smaller and larger than its own characteristic dimension, a direct consequence of the antagonist tendon enabling active bidirectional actuation.

The material and surface finish of the grasped objects also played a significant role. Since the contact normal forces are relatively modest, the friction coefficient between the silicone finger surface and the object surface is critical. The silicone used for the finger body generally produces good grip on a variety of materials. However, a paper tea box of approximately 56 g could not be grasped due to its smooth surface finish, compounded by the compliance of the box itself, which absorbed part of the contact force through deformation rather than transmitting it as friction.

Further unsuccessful grasping attempts included an apple of 155 g, which could be lifted but subsequently slipped from the fingers due to the combination of its smooth peel and weight exceeding the available friction force despite good finger wrapping, and a head of salad of 145 g, which could not be lifted at all due to its weight and the weak wrapping achievable around its irregular shape.

The fingers demonstrated better wrapping performance for objects with a diameter close to or slightly larger than the finger spacing, as in these cases the bending force is more effectively converted into contact force along the finger length. It was also observed that during pinch grasps, after initial fingertip contact, the base of the finger tended to deform before the rest of the body, behaving as a virtual hinge. This is not ideal: an optimal soft finger design should feature compliance that increases progressively toward the fingertip, promoting distal wrapping. In the current design, the silicone matrix maintains a uniform cross-section throughout the finger length, without thinned regions acting as preferential bending points or stiffer embedded elements promoting a desired deformation profile. This represents a potential area for improvement in future design iterations.

Finally, it is worth noting that the protruding bladders served a dual function during grasping. Beyond enabling form-fit coupling with geometric features of objects, their compliance contributed to extending the contact surface area between the finger and the object, thereby increasing the total friction force available. This suggests that incorporating compliant protruding elements in soft finger designs is beneficial not only as a potential mechanical constraint but also as a passive means of improving grasping robustness through increased contact area.

4.5.2 Tactile Sensing System Evaluation

Throughout the pick and place testing, pressure data were acquired from the embedded sensors and analyzed offline. Videos were simultaneously recorded and compared with the pressure data to evaluate the tactile sensing system.

Two configurations were tested. The first was the standard three-finger configuration, in which pressure data were acquired from the three distal bladders of the three fingers, one sensor per finger. The second consisted of a modified version of the three-finger configuration in which one standard finger was replaced with the multi-bladder variant. In this case, pressure data were acquired from the three bladders of the single multi-bladder finger, while the remaining two standard fingers provided actuation only. This configuration allowed the multi-bladder variant to be evaluated without modifying the electronics stack, which was designed to read a maximum of three pressure sensors simultaneously. Extending the system to three multi-bladder fingers, requiring nine sensors, would have necessitated an additional multiplexer and further modifications to the electronics, without adding scientific value within the scope of this work. This extension can be readily implemented in future developments.

The pressure values reported in both figures are expressed as gauge pressure p_g, defined as the instantaneous pressure minus the initial pressure recorded at the start of data acquisition. Since the internal bladder cavity is sealed, the air trapped at the moment of sensor installation, the last step of the manufacturing process of the finger body, remains isolated from the external environment. As a result, the three assembled fingers may exhibit slightly different initial internal pressures depending on the ambient conditions at the time of fabrication, all close to atmospheric pressure. The gauge pressure formulation removes this offset, retaining only the pressure variation due to bladder deformation.

Figure 4.15 (a) reports the gauge pressure profiles over time acquired during the picking of a plastic glass filled with laboratory components, grasped via form-fit coupling. Figures 4.15 (b)-(d) show three video snapshots corresponding to the instants marked in the pressure plot.

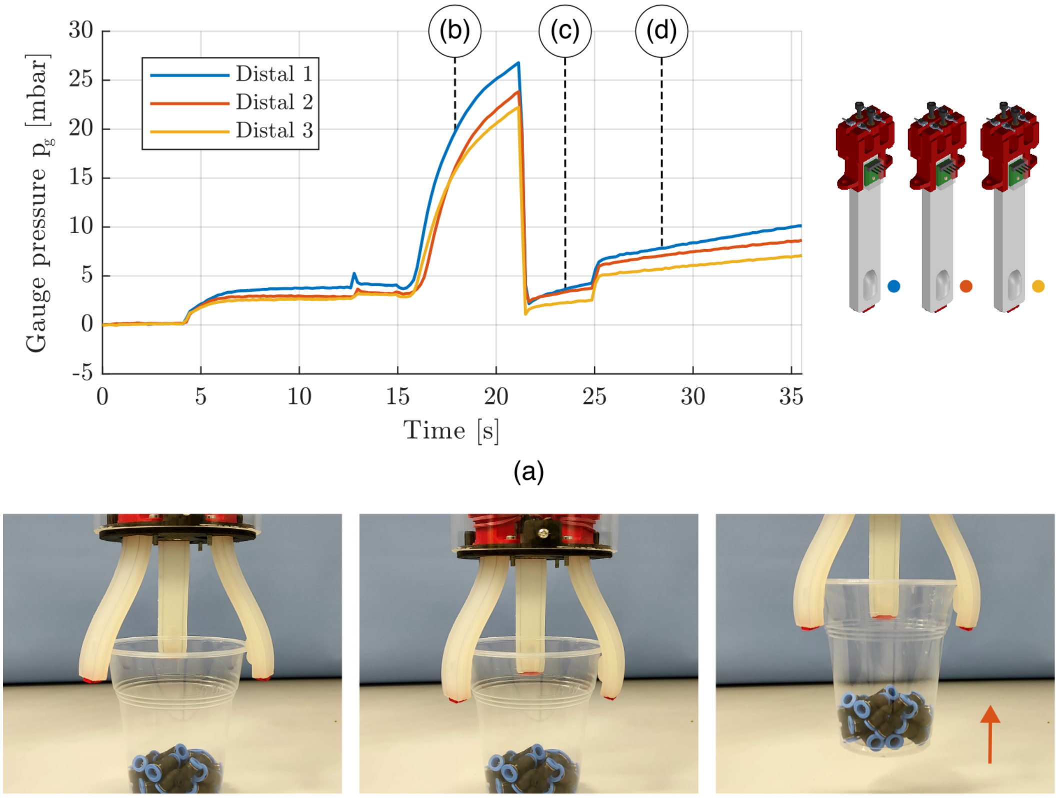

(a)

(b)

(c)

(d)

Figure 4.15: Tactile sensing evaluation, single bladder configuration. **(a)** Gauge pressure profiles over time acquired during the form-fit grasping of a filled plastic glass. The three curves correspond to the distal bladders of the three fingers. **(b)-(d)** Video snapshots at the instants indicated in the pressure plot.

Three distinct phases can be identified. In the first phase, the gripper, already positioned above the glass with fingers open, closes around it. The agonist tendons are activated and the three distal bladders make contact with the rim of the glass, deforming substantially due to the sharp geometry of the rim. A significant pressure increase is recorded by all three sensors. A non-zero gauge pressure is already present before contact, attributable to the slight deformation of the bladder induced by the bending of the finger body itself. In the second phase, the robot arm lowers the gripper further, causing the bladders to slide under the rim. The bladders are less compressed in this configuration and the pressure signals decrease rapidly, remaining slightly above zero as the bladders are still in partial contact with the glass wall. Snapshot (b) captures this phase, showing good finger wrapping around the glass. In the third phase, the robot arm lifts the gripper and the glass. The weight of the object pushes downward against the upper face of the bladders, partially compressing them and producing a second pressure increase, clearly visible in the plot. Snapshot (d) shows the glass successfully lifted, with the red arrow indicating the upward motion.

The tactile sensing system successfully and unambiguously detected contact through bladder deformation. The pressure signal provides not only binary contact information but also an indication of contact intensity, which could be exploited by a dedicated algorithm for contact detection, slip detection, or grasp quality estimation.

Figure 4.16 follows the same layout, reporting pressure data from the multi-bladder finger configuration during the pinch grasp of a coffee tin box. The sequential activation of the bladders along the finger length is clearly visible in the plot.

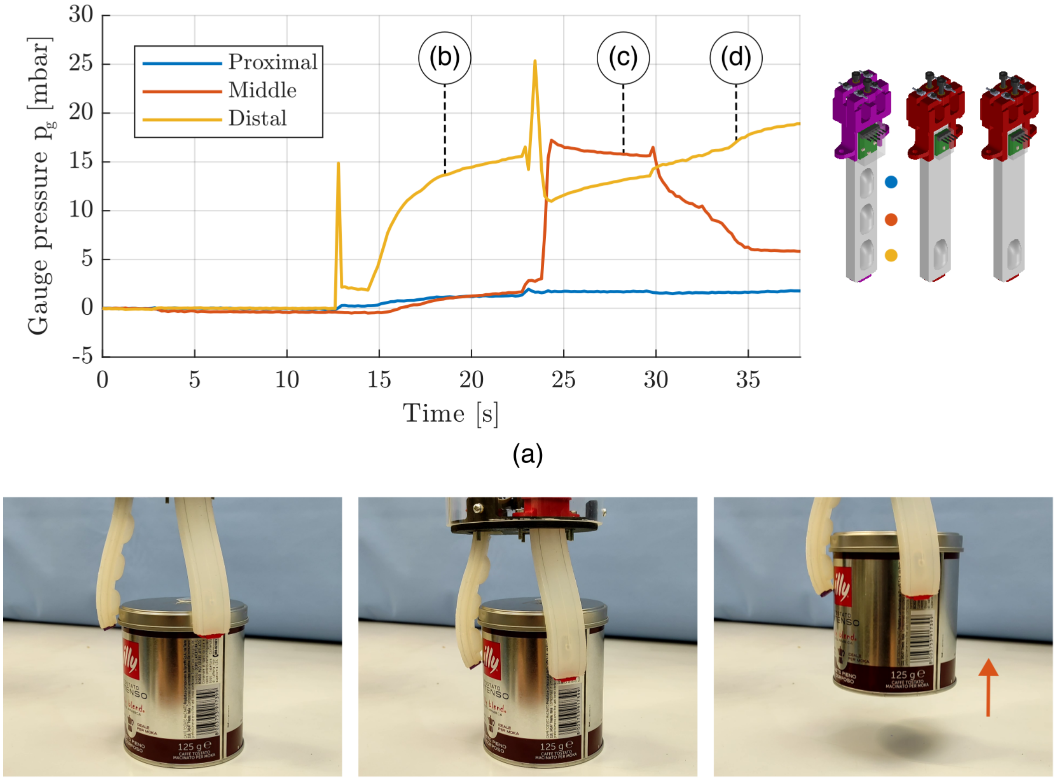

(a)

(b)

(c)

(d)

Figure 4.16: Tactile sensing evaluation, multi-bladder configuration. **(a)** Gauge pressure profiles over time acquired during the three-finger pinch grasp of a coffee tin box. The three curves correspond to the proximal, middle, and distal bladders of the multi-bladder finger. **(b)-(d)** Video snapshots at the instants indicated in the pressure plot.

In the first phase, as the gripper closes, only the distal bladder makes contact with the side wall of the box and its pressure signal rises, shown in yellow. The middle and proximal bladders remain unloaded and their signals stay near zero. In the second phase, the robot arm lowers the gripper. The distal bladder slides along the side wall of the box while the middle bladder reaches the upper edge of the lid, which is slightly wider than the box body, and makes contact with it. The middle bladder pressure increases accordingly, while the distal bladder pressure decreases slightly due to the geometry of the transition between the lid and the body. In the third phase, during lifting, a gradual decrease in the middle bladder pressure and a corresponding increase in the distal bladder pressure suggest a partial slip of the finger along the box surface, with the contact region shifting distally as the box weight loads the lower portion of the finger. The proximal bladder pressure remains near zero throughout, with only a slight increase toward the end, consistent with no direct contact being established at the proximal region.

Two pressure spikes are visible in the distal bladder signal. These appear to be measurement outliers and would be removed by a low-pass filter in a real-time implementation. The sampling frequency used during these tests was approximately 5-10 Hz, which is sufficient for offline analysis but could be increased in future developments to support real-time contact and slip detection algorithms.

It should be acknowledged that the two examples presented represent relatively favorable conditions for the tactile sensing system: both the plastic glass and the coffee tin box have dimensions comparable to the finger spacing, and both feature rigid bodies. These characteristics ensure that most of the actuation force is transferred into bladder deformation rather than being absorbed by object compliance or lost due to poor contact geometry. Pressure data acquired during the grasping of smaller and more compliant objects were analyzed qualitatively as well, and the tactile sensing system demonstrated consistent behavior, though with more subtle pressure variations, confirming its general applicability beyond the two cases reported here.

A final consideration concerns the thermal influence of the SMA tendons on the pressure readings. The tendons heat up to approximately 70°C or above during actuation and are in close proximity to the bladder cavities, potentially warming the trapped air and producing a slow pressure increase unrelated to mechanical contact. This thermal contribution can be distinguished from contact-induced pressure variations by exploiting the difference in their dynamics. Thermal drift, in fact, evolves slowly over the actuation timescale, while contact events produce fast, localized pressure changes. Furthermore, the MS5837 sensors used in this implementation also measure temperature, which could be exploited to compensate for the thermal contribution in future signal processing implementations.

Chapter 5

Conclusions

5.1 Summary and Findings

This thesis presented the design, prototyping, and characterization of an SMA-actuated soft gripper with integrated pressure-based tactile sensing. The work covered the full development cycle of the system, from functional design and mold development to hardware assembly and experimental validation.

The primary novelty of this work lies in the integration of two established subsystems into a single smart actuator: an agonist-antagonist SMA tendon-driven actuation architecture and an embedded pneumatic tactile sensing system based on compliant bladders and miniaturized pressure sensors. While both subsystems have been explored independently in the literature, their combination in a single finger prototype, with the sensing system fully embedded and the antagonist tendon enabling active neutral position recovery, represents a contribution not previously reported.

A modular design approach was followed throughout. The gripper was conceived as a reconfigurable system supporting both two-finger and three-finger configurations through base plate replacement. Two finger variants were developed: a single-bladder version and a three-bladder version enabling contact localization along the finger length. A custom prototyping process was established, based on open mold casting of silicone and integration of soft and rigid components, and documented in detail to support reproducibility.

The finger actuator was characterized through three tests. The step response test revealed settling times in the range of 49 to 69 seconds under step current inputs, with a fingertip deflection of 36 mm at 660 mA, corresponding to 35% of the finger body length. The free-load deformation test confirmed the nonlinear relationship between applied current and steady state deflection, with the phase transformation of the SMA tendons occurring predominantly in the 400–600 mA range. The isometric test measured a maximum fingertip force of 0.22 N at 660 mA and zero imposed deformation, decreasing approximately linearly with increasing deformation. The repeated actuation tests demonstrated the benefit of the antagonist tendon for active neutral position recovery and quantified the thermal drift affecting both the baseline and peak deflection under prolonged cycling.

Grasping capability was evaluated by mounting the gripper on a Kinova Gen2 robotic arm and performing pick and place tasks with 18 objects of different shapes, dimensions, and masses. Fourteen objects were successfully grasped, with a maximum lifted mass of 160 g achieved via form-fit coupling between the protruding bladders and the rim of a plastic glass. Four distinct grasping strategies were identified: power grasp, three-finger pinch grasp, form-fit grasp, and parallel grasp. The gripper demonstrated the ability to manipulate objects ranging from 0.5 to 1.4 times its characteristic finger spacing, a range enabled by the bidirectional actuation provided by the antagonist tendon. The tactile sensing system was evaluated in both single-bladder and three-bladder configurations. Contact events were clearly detectable from the pressure signals in both cases, and the multi-bladder variant provided richer spatial information, with sequential bladder activation enabling the localization of contact along the finger length and the detection of partial slip events.

5.2 Limitations

Several limitations of the current prototype should be acknowledged. The fingertip force of 0.22 N is modest and restricts the range of objects that can be lifted by friction alone, making the gripper most effective for lightweight or geometrically favorable objects. The uniform compliance of the silicone matrix along the finger length leads to a tendency for deformation to initiate at the base rather than distributing progressively toward the fingertip, resulting in a virtual hinge effect that limits wrapping quality during pinch grasps. The current electronics architecture relies on an external power supply for current regulation, with the microcontroller powered separately via USB, limiting the system autonomy and portability.

Finally, the actuation dynamics, with settling times on the order of tens of seconds under step inputs, are relatively slow for practical applications, though this is characteristic of SMA-based systems without dedicated thermal management or control strategies.

5.3 Future Work

Several directions for future development emerge naturally from the limitations identified above.

The fingertip force and range of motion could be improved by extending the tendon length beyond the finger body, routing the tendons externally as demonstrated in the literature [8]. Longer tendons produce larger absolute contractions and higher pulling forces. Alternatively, using multiple tendons in parallel or larger diameter wire would increase the available force.

The wrapping behavior could be improved by introducing compliance variation along the finger length. Embedding rigid elements or thinning the silicone matrix at specific locations to create preferential bending points, virtual hinges by design rather than by accident, would promote more distal and progressive wrapping, improving grasping robustness for a wider range of object geometries.

The grasping performance could also be enhanced by exploring surface texture features on the finger contact faces. Micro-structured elements such as pips or bio-inspired gecko-like adhesive surfaces could significantly increase the effective friction coefficient between the finger and the grasped object, extending the range of liftable masses without requiring higher actuation forces.

The actuation performance could be significantly improved through a dedicated closed-loop control strategy. A two-step current profile, a high initial current for rapid heating followed by a reduced holding current, would reduce actuation time while preventing overheating. Integrating the tactile sensing system into a feedback loop, for example for grasp force regulation or slip detection, would move the system toward reactive grasping. The resistivity variation of SMA wires during the phase transformation could also be exploited for self-sensing, providing position feedback without additional sensors. Integration of the gripper within a ROS-based control framework would facilitate its use in more complex manipulation tasks.

The electronics architecture could be made self-contained by integrating local current regulation on a custom PCB, eliminating the need for an external power supply and significantly reducing the system footprint.

Finally, the tactile sensing system offers several directions for improvement. Alternative bladder geometries and distributions could be explored to optimize sensitivity and spatial resolution. Dedicated signal processing algorithms, for contact detection, slip detection, and grasp quality estimation, could be implemented to exploit the full information content of the pressure signals in real time. The temperature measurement capability of the embedded MS5837 sensors could be exploited to compensate for the thermal drift induced by SMA heating on the pressure readings.

Appendix A

Quasi-Static Tendon-Driven Actuator Model

This appendix presents the quasi-static mechanical model of the SMA tendon-driven soft actuator proposed by Lee et al. [8], reproduced here for completeness using the notation adopted throughout this thesis. It is noted that this model was not used to drive the design of the finger presented in this work, which followed an iterative experimental process. However, the model provides a physically grounded framework for interpreting the results of the characterization tests reported in Chapter 4, and represents a natural direction for future work in which experimental measurements could be compared against model predictions.

Model Assumptions

The model rests on the following assumptions:

- The silicone matrix that forms the body of the finger is treated as an isotropic, homogeneous, and linearly elastic solid with constant Young's modulus E_{Act}.
- The matrix is modelled as a slender Euler–Bernoulli cantilever beam with rectangular cross-section, clamped at its proximal end and free at its distal end.
- Small deformations and small rotations. This assumption is strictly valid only below a few degrees of bending, and is therefore significantly violated throughout the useful operating range of the actuator. It is nonetheless used as it yields a tractable closed-form result that captures the correct qualitative trends, as confirmed by the experimental validation reported in Lee et al.
- The SMA wire tendon exerts a purely axial force along its own direction, applied at an eccentricity d_{SMA} from the neutral axis. By static equivalence, this is resolved into an axial load and a concentrated bending moment $M = F_{SMA} \cdot d_{SMA}$ at the neutral axis. The concentrated end moment produces a uniform bending moment

distribution along the cantilever, implying uniform curvature and a circular arc deformation, see Figure A.1 (a).

- No friction between the wire and the tendon sheath, the wire slides freely and transmits no shear to the matrix.
- Static equilibrium configurations only, no thermal transients or inertial effects.

Model Description

The actuator consists of a rectangular silicone matrix of length l_d, width w, and thickness t, through which an SMA wire is routed via a tendon sheath, see Figure A.1 (b). The wire extends beyond the matrix at each end by a free tendon length L_{Ten}. The model finds the quasi-static equilibrium between the stress produced by the SMA wire and the stress required to bend the matrix.

The force exerted by the SMA wire is:

$$F_{SMA} = A_{SMA}\,\sigma_{SMA} \tag{A.1}$$

where $A_{SMA} = 2\cdot\pi d_{wire}^2/4$ is the effective cross-sectional area of the tendon, accounting for the two parallel branches of the U-shaped wire routing, and σ_{SMA} the stress in the wire. By superposition of the axial and bending effects, the strain at the neutral plane ε_{CP} and at the plane of the SMA wire ε_{AP} are:

$$\varepsilon_{CP} = \frac{F_{SMA}}{E_{Act}\,A_{Act}} \tag{A.2}$$

$$\varepsilon_{AP} = \frac{F_{SMA}\,d_{SMA}^2}{E_{Act}\,I_{Act}} + \frac{F_{SMA}}{E_{Act}\,A_{Act}} \tag{A.3}$$

where $A_{Act} = w \cdot t$ is the matrix cross-sectional area and $I_{Act} = wt^3/12$ its second moment of area. Subtracting ε_{CP} from ε_{AP} isolates the pure bending contribution. The bending angle is then:

$$\theta = \frac{(\varepsilon_{AP} - \varepsilon_{CP})\,l_d}{d_{SMA}} \tag{A.4}$$

The strain actually demanded from the SMA wire, accounting for the total wire length, is:

$$\varepsilon_{SMA} = \frac{\varepsilon_{AP}\,l_d}{l_d + L_{Ten}} \tag{A.5}$$

When $L_{Ten} = 0$ this reduces to the classical embedded-wire case. For $L_{Ten} > 0$, the same fractional strain ε_{SMA} distributed over a longer wire produces a larger absolute contraction, and therefore a larger bending angle, without altering the matrix geometry.

The stress–strain–temperature behaviour of the SMA wire is described by the Brinson one-dimensional thermoconstitutive model:

$$\sigma - \sigma_0 = E(\xi)\,(\varepsilon - \varepsilon_0) + \Omega(\xi)\,(\xi - \xi_0) + \Theta\,(T - T_0) \tag{A.6}$$

where $E(\xi)$ is the martensite-fraction-dependent Young's modulus, $\Omega(\xi) = -E(\xi)\,\varepsilon_L$ is the phase transformation contribution, ε_L is the maximum recoverable strain, and Θ is the thermoelastic coefficient (assumed negligible). Under standard initial conditions this simplifies to:

$$\varepsilon = \frac{\sigma}{\xi E_m + (1-\xi)E_a} + \varepsilon_L\,\xi \tag{A.7}$$

where E_a and E_m are the austenite and martensite Young's moduli. The martensite fraction ξ during strain recovery is:

$$\xi = \frac{\xi_M}{2}\left[\cos\left(\frac{\pi(T-A_s)}{A_f-A_s} - \frac{\pi\sigma}{C_A(A_f-A_s)}\right)+1\right] \tag{A.8}$$

where $\xi_M = 1$ at the start of actuation (fully detwinned martensite), A_s and A_f are the austenite start and finish temperatures, and C_A is a dimensionless fitting parameter. Equations A.1–A.8 are solved simultaneously to find the equilibrium bending angle as a function of temperature and tendon length.

Fingertip Deflection and Force

From the equilibrium bending angle θ, the transverse fingertip deflection follows from the circular arc geometry, see Figure A.1 (c):

$$\delta_\perp = \frac{l_d}{\theta}\,(1-\cos\theta) \tag{A.9}$$

The fingertip force F_{tip} is estimated by a moment balance at the clamped end, equating the tendon moment $M = F_{SMA}\cdot d_{SMA}$ to the moment produced by a transverse tip force with moment arm $R\sin\theta = (l_d/\theta)\sin\theta$:

$$F_{\text{tip}} = \frac{F_{SMA}\cdot d_{SMA}\cdot\theta}{l_d\cdot\sin\theta} \tag{A.10}$$

At small angles $\theta/\sin\theta \approx 1$, recovering the elementary result $F_{tip} = F_{SMA}\cdot d_{SMA}/l_d$. The decrease in tip force with increasing bending angle observed experimentally by Lee et al., and in the course of this thesis, is primarily due to the reduction in F_{SMA}, as the equilibrium operating point shifts. If F_{tip} is required as a function of deflection $\delta_\perp$ rather than θ, Equation A.9 must be inverted numerically and the resulting θ substituted into Equation A.10.

Upper Bound Estimate

A first-order upper bound on actuator performance is obtained by treating the SMA wire as inextensible and prescribing its contraction equal to the maximum recoverable transformation strain $\varepsilon_L \approx$ 4–5% [8]. Setting $\varepsilon_{SMA} = \varepsilon_L$ and assuming this strain is entirely converted into matrix bending yields the theoretical maximum bending angle:

$$\theta_{max} = \frac{\varepsilon_L \left(l_d + L_{Ten}\right)}{d_{SMA}} \tag{A.11}$$

Under the constant curvature assumption, the corresponding maximum transverse fingertip deflection is:

$$\delta_{\max} = \frac{l_d}{\theta_{\max}} \left(1 - \cos\theta_{\max}\right) \tag{A.12}$$

This upper bound cannot be exceeded by the real system. The experimentally measured bending angle will be lower for several reasons. The matrix resistance loads the wire and shifts the SMA equilibrium, reducing the recovered transformation strain. The phase transformation may be incomplete if the wire temperature does not fully reach A_f. Thermal hysteresis and latent heat dissipate part of the available energy. Finally, the elastic compliance of the wire absorbs a fraction of the total contraction. The gap between θ_{max} and the measured angle gives a qualitative measure of how efficiently the system converts the wire's material capability into useful bending.

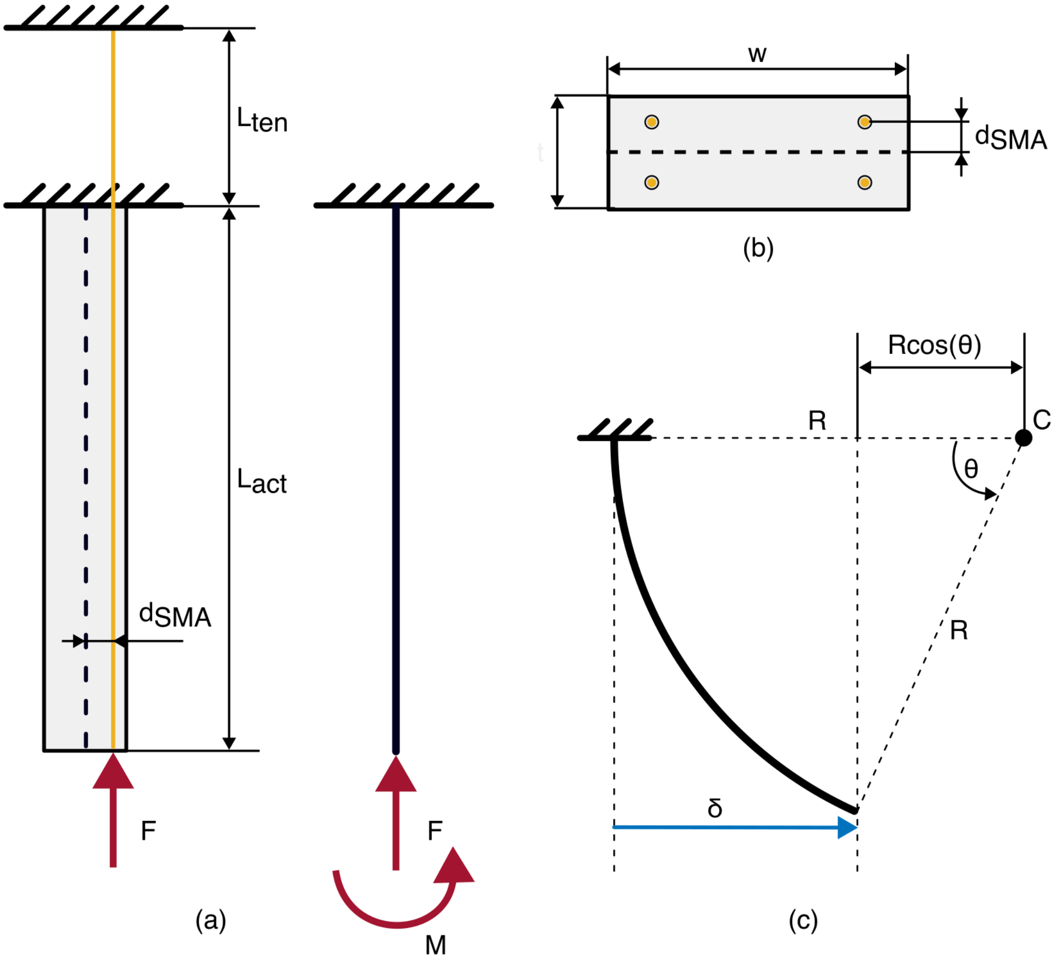

Figure A.1: **(a)** Loading model: the eccentric axial tendon force F at offset d_{SMA} from the neutral axis (left) is resolved by static equivalence into an axial force and a concentrated bending moment $M = F \cdot d_{SMA}$ at the neutral axis (right). **(b)** Rectangular cross-section of the actuator showing the wire positions and eccentricity d_{SMA}. **(c)** Circular arc deformation geometry under the constant curvature assumption, defining the bending radius R, bending angle θ, and transverse fingertip deflection $\delta = R(1 - \cos\theta)$.

Appendix B

Circuit schematic

In Figure B.1 the detailed circuit schematic of the gripper electronics is reported. The general electronics architecture was discussed in the functional design chapter, this appendix provides the complete circuit details including component values and pin connections.

Two IRL540 N-channel MOSFETs were used to realize the digital switches for the agonist and antagonist SMA tendon series. Being N-channel devices, they were placed on the low side of the circuit, with their drains connected in series to the respective SMA series and their sources connected to the common ground. A 10 kΩ pull-down resistor was connected to each gate to ensure the MOSFET remains off when the GPIO is not driven high. A 220 Ω resistor was placed between each gate and the respective ESP32 GPIO pin, GPIO 12 for the agonist series and GPIO 14 for the antagonist series, to limit the gate current and discharge the gate capacitance during switching. When the GPIO is set high (3.3 V), the gate potential reaches approximately 3.2 V due to the voltage divider formed by the 220 Ω and 10 kΩ resistors, which is sufficient to fully enhance the IRL540 and allow current to flow through the SMA series with negligible on-state resistance.

Two status LEDs, connected to GPIO 16 and GPIO 17 respectively, mirror the state of the agonist and antagonist switches. Each LED was wired in series with a 330 Ω current limiting resistor.

The ESP32 was connected to the PC via USB, used both for power supply and for serial data exchange. The I^2C bus was formed by the 3.3 V, GND, GPIO 21 (SDA), and GPIO 22 (SCL) lines of the ESP32.

Two INA219 current sensors were placed on the high side of each SMA series, between the positive terminal of the external power supply and the high side of the respective tendon series. The ground of the external power supply was connected to the ESP32 ground to establish a common reference for the entire circuit. The INA219 sensors were connected to the I^2C bus, both for data exchange and power. To assign distinct I^2C addresses to the two sensors, the address configuration pads on one of the Adafruit breakout boards were bridged by soldering, assigning addresses 0x40 and 0x41 respectively. No additional pull-up resistors were added to the main I^2C bus, as the

Adafruit INA219 breakout boards already feature internal 10 kΩ pull-up resistors. The two resistors in parallel result in an equivalent 5 kΩ pull-up, which is also exploited by the multiplexer.

The TCA9548A I^2C multiplexer was connected to the main I^2C bus. The three MS5837 pressure sensors were connected to channels 3, 5, and 7 of the multiplexer respectively, with their VDD pins connected to the 3.3 V rail and their GND pins to the common ground. A 100 nF decoupling capacitor was added between the VDD and GND pins of each sensor to stabilize the supply voltage during ADC conversions. Two 5 kΩ pull-up resistors were added per sensor channel, one on SDA and one on SCL, connected to the 3.3 V rail.

The circuit was designed following the electrical specifications and recommendations reported in the datasheets of the individual components [25, 26, 27, 28, 29]. In particular, the gate resistor values, decoupling capacitors, and pull-up resistor sizing were selected in accordance with the respective manufacturer guidelines.

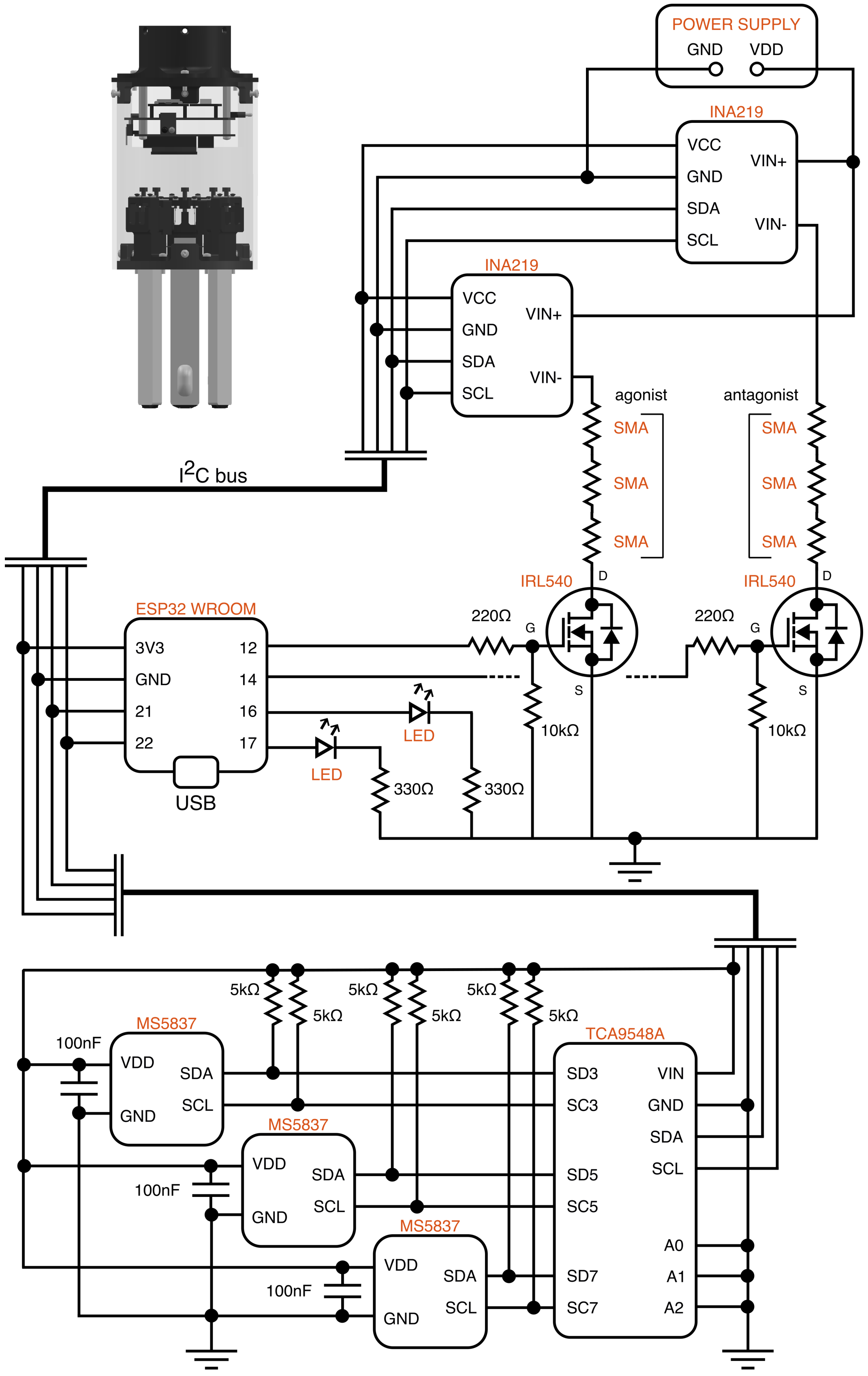

Figure B.1: Circuit schematic of the gripper electronics.

Bibliography

[1] Jun Shintake, Vito Cacucciolo, Dario Floreano, and Herbert Shea. "Soft Robotic Grippers." In: *Advanced Materials* 30.29 (2018), p. 1707035. issn: 1521-4095. doi: 10.1002/adma.201707035.

[2] Eduardo Navas, Roemi Fernández, Delia Sepúlveda, Manuel Armada, and Pablo Gonzalez-de-Santos. "Soft Grippers for Automatic Crop Harvesting: A Review." In: *Sensors* 21.8 (Apr. 2021), p. 2689. issn: 1424-8220. doi: 10.3390/s21082689.

[3] Mohammad Mahdi Kheirikhah, Samaneh Rabiee, and Mohammad Ehsan Edalat. "A Review of Shape Memory Alloy Actuators in Robotics." In: *RoboCup 2010: Robot Soccer World Cup XIV*. Lecture Notes in Computer Science, vol. 6556. Berlin: Springer, 2011, pp. 206–217. doi: 10.1007/978-3-642-20217-9_18.

[4] William Coral, Claudio Rossi, Julian Colorado, Daniel Lemus, and Antonio Barrientos. "SMA-Based Muscle-Like Actuation in Biologically Inspired Robots: A State of the Art Review." In: *Smart Actuation and Sensing Systems — Recent Advances and Future Challenges*. Ed. by Giovanni Berselli, Rocco Vertechy, and Gabriele Vassura. Rijeka: InTech, 2012, chap. 3, pp. 53–82. doi: 10.5772/50209.

[5] Min-Soo Kim, Jae-Kyung Heo, Hugo Rodrigue, Hyun-Taek Lee, Salvador Pané, Min-Woo Han, and Sung-Hoon Ahn. "Shape Memory Alloy (SMA) Actuators: The Role of Material, Form, and Scaling Effects." In: *Advanced Materials* 35.3 (2023), p. 2208517. issn: 1521-4095. doi: 10.1002/adma.202208517.

[6] Haoyuan Du, Guorui Li, Jiyu Sun, Yanyan Zhang, Yunhe Bai, Chen Qian, and Yiming Liang. "A Review of Shape Memory Alloy Artificial Muscles in Bionic Applications." In: *Smart Materials and Structures* 32.10 (2023), p. 103001. issn: 0964-1726. doi: 10.1088/1361-665X/acf1e8.

[7] Hunter Song, Eric Kubica, and Rob Gorbet. "Resistance Modelling of Shape Memory Alloy Wires." In: *e-Journal of Nondestructive Testing* 17.2 (2012). Proceedings of Smart Materials & Structures / NDT in Aerospace / NDT in Canada 2011, Montreal, Canada, Nov. 2–4, 2011. url: `https://www.ndt.net/?id=11480`.

[8] Ji-Hyeong Lee, Yoon Seop Chung, and Hugo Rodrigue. "Long Shape Memory Alloy Tendon-based Soft Robotic Actuators and Implementation as a Soft Gripper." In:

Scientific Reports 9.1 (Aug. 2019), p. 11785. issn: 2045-2322. doi: 10.1038/s41598-019-47794-1.

[9] Hugo Rodrigue, Wei Wang, Dong-Ryul Kim, and Sung-Hoon Ahn. "Curved Shape Memory Alloy-based Soft Actuators and Application to Soft Gripper." In: *Composite Structures* 176 (Sept. 2017), pp. 398–406. issn: 0263-8223. doi: 10.1016/j.compstruct.2017.05.056.

[10] Hyung-Il Kim, Min-Woo Han, Sung-Hyuk Song, and Sung-Hoon Ahn. "Soft Morphing Hand Driven by SMA Tendon Wire." In: *Composites Part B: Engineering* 105 (Nov. 2016), pp. 138–148. issn: 1359-8368. doi: 10.1016/j.compositesb.2016.09.004.

[11] Oybek Valijonovich Tuyboyov, Geo-Sung Lee, and Gil-Yong Lee. "Multi-mode Soft Composite Bending Actuators Based on Glass Fiber Textiles Interwoven with Shape Memory Alloy Wires: Development and Use in the Preparation of Soft Grippers." In: *International Journal of Precision Engineering and Manufacturing-Green Technology* 10.5 (2023), pp. 1263–1280. issn: 2198-0810. doi: 10.1007/s40684-022-00491-3.

[12] Wei Wang and Sung-Hoon Ahn. "Shape Memory Alloy-Based Soft Gripper with Variable Stiffness for Compliant and Effective Grasping." In: *Soft Robotics* 4.4 (Dec. 2017), pp. 379–389. issn: 2169-5172. doi: 10.1089/soro.2016.0081.

[13] M. Dzareeful F. Abdullah, Azni Nabela Wahid, and Asan G.A. Muthalif. "Development of Shape Memory Alloy (SMA) Based Artificial Muscle for Application in Soft Gripper." In: *Journal of Engineering Science and Technology* 18.3 (June 2023), pp. 1413–1426. issn: 1823-4690.

[14] Yu She, Chang Li, Jonathon Cleary, and Hai-Jun Su. "Design and Fabrication of a Soft Robotic Hand with Embedded Actuators and Sensors." In: *Journal of Mechanisms and Robotics* 7.2 (May 2015), p. 021007. issn: 1942-4302. doi: 10.1115/1.4029497.

[15] Tess Hellebrekers, Kadri Bugra Ozutemiz, Jessica Yin, and Carmel Majidi. "Liquid Metal-Microelectronics Integration for a Sensorized Soft Robot Skin." In: *Proceedings of the IEEE/RSJ International Conference on Intelligent Robots and Systems (IROS)*. Madrid, Spain, Oct. 2018, pp. 4924–4929. doi: 10.1109/IROS.2018.8593944.

[16] Claudio Rossi, Julian Colorado, William Coral, and Antonio Barrientos. "Bending Continuous Structures with SMAs: A Novel Robotic Fish Design." In: *Bioinspiration & Biomimetics* 6.4 (Dec. 2011), p. 045005. issn: 1748-3190. doi: 10.1088/1748-3182/6/4/045005.

[17] William Coral and Claudio Rossi. "Soft Dorsal/Anal Fins Pairs for Roll and Yaw Motion in Robotic Fish." In: *Bioinspiration & Biomimetics* 18.1 (2022), p. 016008. issn: 1748-3190. doi: 10.1088/1748-3190/aca132.

[18] Daoxiong Gong, Rui He, Jianjun Yu, and Guoyu Zuo. "A Pneumatic Tactile Sensor for Co-Operative Robots." In: *Sensors* 17.11 (Nov. 2017), p. 2592. issn: 1424-8220. doi: 10.3390/s17112592.

[19] Sinuo Zhao, Chi Cong Nguyen, Trung Thien Hoang, Thanh Nho Do, and Hoang-Phuong Phan. "Transparent Pneumatic Tactile Sensors for Soft Biomedical Robotics." In: *Sensors* 23.12 (June 2023), p. 5671. issn: 1424-8220. doi: 10.3390/s23125671.

[20] Maria Pozzi, Leonardo Franco, Zubair Iqbal, Monica Malvezzi, Domenico Prattichizzo, and Gionata Salvietti. "Soft Pneumatic Pads Enable New Sensing and Actuation Capabilities in Soft-Rigid Grippers." In: *Proceedings of the IEEE International Conference on Soft Robotics (RoboSoft)*. San Diego, CA, USA, Apr. 2024. doi: 10.1109/ROBOSOFT60065.2024.10522022.

[21] Giovanni Colucci. "Pneumatic Soft Robotic System for Actuation and Sensing: Novel Sustainable Solutions for Service Robotics." Politecnico di Torino, 2025. url: `https://iris.polito.it/retrieve/handle/11583/3000605/fddfa6dd-3674-46fd-87e2-1d57ecee049c/conv_01_summary_c.pdf`.

[22] Siqi Shang, Mingyo Seo, Yuke Zhu, and Lillian Chin. "FORTE: Tactile Force and Slip Sensing on Compliant Fingers for Delicate Manipulation." In: *IEEE Robotics and Automation Letters* (2026). doi: 10.1109/LRA.2026.3662618.

[23] Naveen Kuppuswamy, Alex Alspach, Avinash Uttamchandani, Sam Creasey, Takuya Ikeda, and Russ Tedrake. "Soft-Bubble Grippers for Robust and Perceptive Manipulation." In: *Proceedings of the IEEE/RSJ International Conference on Intelligent Robots and Systems (IROS)*. Las Vegas, NV, USA, Oct. 2020, pp. 9475–9482. doi: 10.1109/IROS45743.2020.9341534.

[24] Martin R. Cutkosky. "On Grasp Choice, Grasp Models, and the Design of Hands for Manufacturing Tasks." In: *IEEE Transactions on Robotics and Automation* 5.3 (June 1989), pp. 269–279. issn: 1042-296X. doi: 10.1109/70.34763.

[25] Espressif Systems. *ESP32-WROOM-32D & ESP32-WROOM-32U — Datasheet*. Espressif Systems (Shanghai) Co., Ltd., Shanghai, China, 2023. url: `https://documentation.espressif.com/esp32-wroom-32d_esp32-wroom-32u_datasheet_en.pdf`. (Accessed: 2025).

[26] Adafruit Industries. *Adafruit INA219 Current Sensor Breakout — Product Guide*. Adafruit Industries LLC, New York, NY, USA. url: `https://learn.adafruit.com/adafruit-ina219-current-sensor-breakout`. (Accessed: 2025).

[27] TE Connectivity. *MS5837-30BA: Miniature 300 Bar Module with Waterproof Capability — Datasheet.* TE Connectivity Ltd., 2017. url: `https://www.te.com/en/product-MS583730BA01-50.html`. (Accessed: 2025).

[28] Texas Instruments. *TCA9548A: 1-to-8 I^2C Bus Switch with Reset — Datasheet.* Texas Instruments Inc., Dallas, TX, USA, 2015. url: `https://www.ti.com/lit/ds/symlink/tca9548a.pdf`. (Accessed: 2025).

[29] Vishay Siliconix. *IRL540: N-Channel 100V (D-S) MOSFET — Datasheet.* Vishay Intertechnology Inc., Malvern, PA, USA. url: `https://www.vishay.com/docs/91300/irl540.pdf`. (Accessed: 2025).

[30] Polytek Development Corp. *PlatSil® Gel-25: Platinum-Catalyzed Silicone Rubber — Technical Bulletin.* Polytek Development Corp., Easton, PA, USA. url: `https://polytek.com/content/pdf/TDS/PlatSilGels_TechnicalBulletin_Polytek%20Std%20Prods%20SkinSafe.pdf`. (Accessed: 2025).

[31] Dynalloy, Inc. *Flexinol® Actuator Wire: Technical and Design Data.* Dynalloy, Inc., Tustin, CA, USA. url: `https://dynalloy.com/wp-content/uploads/2025/03/TCF1140.pdf`. (Accessed: 2025).

[32] Bambu Lab. *Bambu Lab X1 Carbon: 3D Printer.* Bambu Lab Co., Ltd., Shenzhen, China, 2023. url: `https://bambulab.com/en/x1`. (Accessed: 2025).

[33] NICE-POWER. *SPS305D: 30V 5A Regulated DC Power Supply — User Manual.* Shenzhen Yizhan Electronic Co., Ltd., Shenzhen, China. url: `https://nice-power.com.cn/productinfo/637000.html`. (Accessed: 2025).

[34] Kinova Inc. *JACO^2 Gen2: 7 DOF Assistive Robotic Arm — User Guide and SDK Documentation.* Kinova Inc., Boisbriand, QC, Canada. url: `https://www.kinovarobotics.com`. (Accessed: 2025).